Sager, W.W., Sano, T., Geldmacher, J., and the Expedition 324 Scientists
Proceedings of the Integrated Ocean Drilling Program, Volume 324

Methods[1]

Expedition 324 Scientists[2]

Chapter contents

Procedures

Numbering of sites, holes, cores, and samples

Drilling sites are numbered consecutively from the first site drilled by the *Glomar Challenger* in 1968. Integrated Ocean Drilling Program (IODP) Expedition 301 began using the prefix "U" to designate sites occupied by a U.S. Implementing Organization (USIO) vessel. For all IODP drill sites, a letter suffix distinguishes each hole drilled at the same site. The first hole drilled is assigned the site number modified by the suffix "A," the second hole takes the site number and the suffix "B," and so forth. For Expedition 324, each site has only one hole (A).

The cored interval is measured in meters below seafloor (mbsf) according to the core depth below seafloor, method A (CSF-A), depth scale (see IODP Depth Scale Terminology at **www.iodp.org/program-policies/**). In general, the depth below seafloor is determined by subtracting the water depth estimated from the initial drill pipe measurement to the seafloor from the total drill pipe measurement. The depth interval assigned to an individual core begins with the depth below seafloor at which coring began and extends to the depth that coring advanced. Each coring interval is generally ~9.5 m, which is the length of a core barrel; however, coring intervals may be shorter. During Expedition 324, some of the overlying sediment succession was drilled without coring. Coring at all sites started ~50–70 m above the expected basement contact.

During Expedition 324, unless otherwise noted, all core depths below seafloor were calculated as CSF-A. For ease of communication of shipboard results, all depths are reported in this volume as "meters below seafloor" unless otherwise noted.

Cores taken from a hole are numbered sequentially from the top of the hole downward. Core numbers and their associated cored intervals are unique in a given hole. Generally, maximum recovery for a single core is 9.5 m of rock or sediment contained in a plastic liner (6.6 cm internal diameter) plus ~0.2 m (without a plastic liner) in the core catcher, which is a device at the bottom of the core barrel that prevents the core from sliding out when the barrel is being retrieved from the hole. In certain situations, recovery may exceed the 9.5 m maximum. In soft sediments, this is normally caused by core expansion resulting from depressurization. In hard rock cores, this probably happens when a pedestal of

---

[1] Expedition 324 Scientists, 2010. Methods. *In* Sager, W.W., Sano, T., Geldmacher, J., and the Expedition 324 Scientists, *Proc. IODP,* 324: Tokyo (Integrated Ocean Drilling Program Management International, Inc.). doi:10.2204/iodp.proc.324.102.2010

[2] **Expedition 324 Scientists' addresses.**

rock fails to break off and is grabbed by the next core barrel.

A recovered core is divided into 1.5 m sections that are numbered serially from the top. When full recovery is obtained, the sections are numbered 1 through 7, with the last section usually being shorter than 1.5 m. Rarely, an unusually long core may require >7 sections. When the recovered core is shorter than the cored interval, the top of the core is equated with the top of the cored interval by convention to achieve consistency in handling analytical data derived from cores. All pieces recovered are placed immediately adjacent to each other in the core tray. Samples and descriptions of cores are designated by distance, measured in centimeters from the top of the section to the top and bottom of each sample or interval. By convention, material recovered from the core catcher is placed below the last section when the core is described and is labeled with the suffix "CC." In sedimentary cores, the core catcher section is treated as a separate section. The core catcher is placed at the top of the cored interval in cases in which material is recovered only in the core catcher. However, information supplied by the drillers or by logging may allow more precise interpretation as to the correct position of core catcher material within an incomplete recovered cored interval.

A complete identification number for a sample consists of the following information: expedition, site, hole, core number, core type, section number with the interval in centimeters measured from the top of the section, and piece number (assigned only for hard rock). For example, a sample identification of "324-U1350A-26R-8 (Piece 1, 4–7 cm)" indicates a 3 cm sample of Piece 1 removed from the interval between 4 and 7 cm below the top of Section 8 of Core 26 ("R" designates that this core was taken with the rotary core barrel [RCB]) in Hole A at Site U1350 during Expedition 324.

Core handling

Cores recovered during Expedition 324 were extracted from the core barrel in plastic liners. These liners were carried from the rig floor to the core processing area on the catwalk outside the core laboratory, where they were split into ~1.5 m sections. Liner caps (blue = top, colorless = bottom) were glued with acetone onto liner sections on the catwalk by the curator. Hard rock pieces were pushed to the top of the liner sections and total rock length was measured. The length was entered into the database using the Sample Master application as "created length." This number is used to calculate recovery. The 1.5 m sections were transferred to the core splitting room, where the plastic liners were split lengthwise to expose the core.

Oriented pieces of core were marked on the bottom with a red wax pencil to preserve orientation, either before they were extracted from the core barrel or when they were removed from the split core liner. In some cases, pieces were too small to be oriented with certainty. Adjacent but broken core pieces that could be fit together along fractures were curated as single pieces. The structural geologist on shift confirmed piece matches and corrected any errors. The structural geologist also marked the split line on the pieces, which defined how the pieces were cut in two equal halves. The aim was to maximize the expression of dipping structures on the cut face of the core while maintaining representative features in both archive and working halves. A plastic spacer was secured to the split core liner with acetone between individual pieces or reconstructed contiguous groups of subpieces. These spacers may represent a substantial interval of no recovery. The length of each section of core, including spacers, was entered into the curation database as the curated length. Curated length commonly differs by a few to several centimeters from the created length measured on the catwalk. The database then recalculates the assumed depth of each piece based on the curated length.

Each section was allowed to equilibrate to ambient room temperature (3 h for hard rock, 4 h for sediment) and first scanned using the shipboard Whole-Round Multisensor Logger (WRMSL) (see **"Physical properties"**). The whole-round core sections were next measured with the Natural Gamma Ray Logger (NGRL) (see **"Physical properties"**). Each piece of core was then split with a diamond-impregnated saw into an archive half and a working half, with the positions of plastic spacers between pieces maintained in both halves. Pieces were numbered sequentially from the top of each section, beginning with number 1. Separate subpieces within a single piece are assigned the same number but were lettered consecutively (e.g., 1A, 1B, 1C). Pieces were labeled only on the outer cylindrical surfaces of the core. If it was evident that an individual piece had not rotated around a horizontal axis during drilling, an arrow was added to the label, pointing to the top of the section. The oriented character of the piece was then recorded in the database using the Sample Master application

Digital images of the dry, cut faces of the archive halves were captured with the Section Half Imaging Logger (SHIL). Measurements of point magnetic susceptibility and color reflectance were performed with the Section Half Multisensor Logger (SHMSL) on the archive half of the cores. This instrument also includes a laser calibration system. The data from the laser (e.g., the location of gaps in the core and rubble intervals) was used to aid data filtering of multisensor measurements (see **"Physical properties"**).

The archive half of each core was described for magmatic lithology and structural features, and observations were recorded using the descriptive data capture application, DESClogik. Specialized templates and spreadsheets were developed for this application by the individual descriptive laboratory groups (for details, see individual disciplinary sections in this chapter).

Finally, digital color close-up images were taken of particular features, as requested by individual scientists. During the crossover of both day and night shifts, a sample meeting was held to discuss the sections described and to select key intervals for shipboard analyses sampling.

Samples were taken on working halves for shipboard physical property, paleomagnetic, thin section, X-ray diffraction (XRD), and geochemical analyses, as described in the sections below. Each extracted sample was logged into the Sample Master database program by location, sample type, and intended shipboard study (e.g., thin section, XRD, etc.). Records of all removed samples are kept by the IODP Curatorial Specialist. Sampling for personal postcruise research was delayed until the transit at the end of the expedition. This allowed for a more careful sample selection because it was based on the integrated shipboard data set (e.g., geochemical analyses, thin section descriptions, and other observational or analytical data stored in the database). At the end of Expedition 324, all cores were transferred from the ship for permanent storage at the IODP Gulf Coast Repository in College Station, Texas (USA).

Authorship of site chapters

The separate sections of the site chapters and methods chapter were written by the following shipboard scientists (authors are listed in alphabetical order; no seniority is implied):

Sedimentology: Littler, Matsubara, Woodard
Paleontology: Ando, Herrmann
Igneous petrology: Almeev, Greene, Koppers, Miyoshi, Natland, Shimizu, Widdowson
Alteration and metamorphic petrology: Delacour, Murphy
Structural geology: Hirano, Li
Geochemistry: Heydolph, Ishikawa, Mahoney
Physical properties: Harris, Kang, Prytulak
Paleomagnetism: Carvallo, Ooga, Tominaga
Downhole logging: Evans, Iturrino

Sedimentology

The lithostratigraphy of sediments recovered during Expedition 324 was determined using a variety of descriptive and analytical techniques. These included digital core imaging, color reflectance, magnetic susceptibility, and sedimentological observations based on visual (macroscopic) core description, thin sections, and smear slides. The methods employed during this expedition were similar to those used during Ocean Drilling Program (ODP) Leg 198 (Shipboard Scientific Party, 2002a), during which sediments were also drilled on Shatsky Rise. Expedition 324 used the DESClogik application (see link to user guides at **iodp.tamu.edu/tasapps/**) to record descriptive data for the Laboratory Information Management System (LIMS) database, which was first implemented during IODP Expedition 320T (Expedition 320T Scientists, 2009). Three spreadsheet templates were customized for Expedition 324 in DESClogik prior to the arrival of the first core. The spreadsheet templates were used to record macroscopic core descriptions, as well as smear slide and thin section data, which helped quantify the texture and relative abundance of biogenic and nonbiogenic components. The locations of all smear slide and thin section samples taken from each core were recorded in the IODP-USIO Sample Master program. The descriptive data were used to produce the visual core description (VCD) graphic reports.

Core imaging

After whole cores were split into archive and working halves, the flat face of the archive half was imaged using the SHIL. Images were taken with a line scan camera at 20 pixel/mm intervals. This process generated high-resolution digital images that aided core description, as the high quality of the images enhances the appearance of some sedimentary features.

Visual core descriptions

Cores were examined and the descriptions were entered into the DESClogik sedimentary template, from where they were uploaded into the central LIMS database. The data were used to produce VCD graphic reports (Fig. **F1**), which include simplified graphical representations of the cores with accompanying descriptions of the features observed. Depending on the type of material drilled, two VCDs were sometimes produced for each core, one to describe the sediments/sedimentary rocks recovered and the other for description of igneous features. In contrast to the igneous VCD, which displays data in terms of core sections, the sedimentary VCD shows the entire core. For further information about the igneous VCDs, see **"Igneous petrology."**

Hole, core, and interval (core depth below seafloor) are given at the top of the VCD, and core depths and section lengths are indicated along the far left margin. Physical descriptions of the core correspond to entries in the DESClogik application and include lithology, grain size, sedimentary structures, bioturbation, accessory features, and the types of samples taken from the core for shipboard studies. Additionally, selected physical property data (gamma ray attenuation [GRA] bulk density, magnetic susceptibility, and color reflectance) and paleontological observations are displayed on the sediment VCDs. A core summary section at the top of the VCD provides a generalized overview of the lithology and features of the whole core. The individual columns shown in the VCD are listed below, followed by an outline of the lithostratigraphic classification used during Expedition 324.

Core summary

A brief overview of major and minor lithologies present in the core, as well as notable features (e.g., sedimentary structures), are presented in the core summary text field at the top of the VCD. The summary includes sediment color determined qualitatively using the Munsell soil color charts (Munsell Color Company, Inc., 1994). Because color of the sediment may evolve during drying and subsequent redox reactions, color was described shortly after the cores were split.

Section

Once on deck each core was cut into sections. The section number is listed in the far left column of the VCD along the core image scan and the core depth in meters.

Core image

The high-resolution scans of each core section made by the SHIL are compiled to provide a continuous image of the entire core to the right of the column listing the core sections. Sedimentary VCDs are created only for cores which contain at least a 1 m interval of sediments.

Graphic lithology

The lithology of the core recovered is represented on the VCD sheet by graphic patterns (Fig. F2). For intervals containing homogeneous mixtures of multiple lithologies, patterns are arranged within the column from left to right in order of their relative abundance. Only components determined to be the primary lithology of the sediment (most abundant) are represented in the Graphic Lithology column. The width of each pattern in the column gives the relative abundance of that component. Therefore, the Graphic Lithology column represents an approximate estimate of the sedimentary constituents, rather than a quantitative characterization. It is important to note that occasionally other sedimentary constituents, which comprise >25% (major component), are not displayed. We suggest interested parties access the LIMS database (**iodp.tamu.edu/tasapps/**) to obtain detailed descriptive information and a complete characterization of the sedimentary material recovered.

Gamma ray attenuation bulk density

Where recovery and core length permitted, the bulk density of the sediments was measured using GRA (see **"Physical properties"**). The raw and filtered data appear in the first column to the right of the Graphic lithology column.

Magnetic susceptibility

Where recovery and core length permitted, the magnetic susceptibility, which roughly indicates sedimentary iron content, was measured (see **"Physical properties"**). The raw and filtered data appear beside the GRA bulk density column.

Color reflectance spectrophotometry

Reflectance of visible light from the archive halves of sediment cores was routinely measured using a SHMSL. The SHMSL was equipped with OceanOptics software for analysis of color reflectance data. Cores consisting of soft sediment were covered with clear plastic wrap and placed on the SHMSL. Hard rock sections were run without the protective plastic cover. Measurements were taken at 1–2 cm spacing. The SHMSL is set to skip empty intervals in the core liner but cannot recognize relatively small cracks, disturbed areas of core, or plastic section dividers. Thus, raw SHMSL data may contain spurious measurements that should ideally be edited out of the data set before use. Therefore, a filter was applied to the reflective data set (see **"Physical properties"**). Both filtered and unfiltered data are shown on the VCD.

Age

The nannofossil or foraminifer zone which defines the age of the sediments is listed in the Age column.

Grain size

The Grain size column displays the dominant grain size of the sediment. Where mixtures of multiple sedimentary constituents with varying grain sizes occur, the most prevalent grain size is displayed. Rather than being plotted by absolute size, sedimentary grain sizes are represented numerically using a range from 0 (cryptocrystalline) to 6 (gravel/pebble/lapilli) (Fig. **F2**).

Shipboard sample

Samples taken for shipboard analyses are recorded here. These samples include toothpick samples and thin sections, all micropaleontology samples, and those taken for physical properties measurements. At least one or two smear slides (or thin sections) were generated from each core to constrain sedimentary composition. In addition, coulometric analyses of carbonate content and carbon-hydrogen-nitrogen-sulfur (CHNS) analyses of total sedimentary carbon were performed on discrete samples to aid lithologic description.

Bioturbation

Degree of bioturbation was determined by observing how intensely the sediment was altered by the action of organisms (Droser and Bottjer, 1986). Degree of bioturbation was determined based on the following parameters: intense (75%–100%), moderate (25% to <75%), and minor (>0% to <25%). Graphic symbols in the Bioturbation intensity column illustrate these parameters (Fig. **F2**).

Fossils

Identifiable trace fossils (ichnofossils) and any major body fossils or fossil fragments recovered are displayed to the right of the Bioturbation intensity column in the Ichnofossil/Fossil column.

Structures

Structures resulting from physical sedimentary processes and those associated with drilling disturbance are shown in the following columns.

Sedimentary structure

Structures formed by both physical and biogenic processes are included. These processes include detailed descriptions of features such as laminations and cross-bedding, contacts between sediments of differing lithologies, and any soft-sediment deformation structures (e.g., flame structures).

Lithologic accessories

Nonprimary sedimentary constituents such as authigenic or diagenetic minerals are recorded in the Lithologic accessories column. Alteration structures and postdepositional features (e.g., sedimentary coatings) also appear here.

Drilling disturbance

The degree to which the core is affected by drilling disturbance is recorded in this column (e.g., biscuiting) (Fig. **F2**).

Sediment classification

Lithologic names including sediment composition, degree of lithification, and/or texture are based on conventions outlined by Mazzullo et al. (1988) in the ODP sediment classification scheme. The principal name is based on the composition of the major lithology as identified by observation, smear slides, and so on, and is preceded by major modifiers (in order of increasing abundance) that refer to components making up at least 25% of the sediment. Minor components represent between 10% and 25% of the sediment and follow the principal name in order of increasing abundance. Thus a well-indurated sample containing 70% nannofossils, 25% clay minerals, and 5% foraminifers would be described as a "clayey nannofossil limestone." Only the major lithology is recorded in the Graphic lithology column, whereas other major and minor components are available from the LIMS database.

Size divisions for grains are those of Wentworth (1922) (Fig. **F3**). These size and textural qualifiers were not used in the sediment names (e.g., nannofossil clay implies that the dominant component is clay minerals rather than clay-sized nannofossils).

Terms that describe lithification are dependent upon the dominant composition. For sediments derived predominantly from calcareous organisms (e.g., calcareous nannofossils and foraminifers) the terms "ooze," "chalk," and "limestone" are applicable. If the sediment can be deformed with a finger it is classed as ooze, if it can be scratched easily by a fingernail it is chalk, and if it cannot be scratched easily it is limestone.

For sediments derived predominantly from siliceous microfossils (diatoms, radiolarians, and siliceous sponge spicules) the terms "ooze," "radiolarite/spiculite/diatomite," and "chert" are applicable. If the sediment can be deformed with a finger it is classified as ooze, if it cannot be easily deformed manually it is radiolarite/spiculite/diatomite, and if it displays a glassy luster it is chert. The term "porcellanite" is used as defined by Keene (1975) and describes a siliceous limestone/claystone that has a dull luster and is less hard and compact than chert. Porcellanite may contain a mix of opal, quartz, clay minerals, and carbonate. Note that the terms porcellanite and chert do not imply crystallinity of the silica.

For sediments derived predominantly from siliciclastic material, naming is based on the dominant grain size rather than the degree of lithification. For indurated material, the lithification suffix "-stone" is appended to the dominant size classification (e.g., "silt" versus "siltstone").

For sediments composed predominantly of fine-grained volcaniclastic grains the terms "volcanic ash" and "tuff" are applicable. If the sediment can be deformed easily with a finger, the interval is described as ash and a modifier of "coarse" or "fine" is given to indicate the grain size range of sand and silt/clay, respectively. For more consolidated material, the rock is called tuff. The term "volcaniclastic breccia" is used for coarse-grained material (i.e., granule and pebble size categories). Discrete pumice lapilli are noted simply as "pumice." If a rock is composed of volcanic grains which have obviously experienced transport and redeposition it may be referred to as a "volcaniclastic sandstone" or "volcaniclastic mudstone." The terms "breccia" and "conglomerate" are used for rocks which contain many grains >2 mm in size. If the composition of the majority of the clasts is igneous, then "volcaniclastic" may be added to the beginning as a descriptive qualifier. At Site U1348, the term "hyaloclastite" is used for vitroclastic (i.e., glassy) materials produced by the interaction of water and hot magma or lava (Fisher and Schmincke, 1984). Fine-grained hyaloclastite is classified into "fine hyaloclastite" (clay and silt size categories) and "hyaloclastite sandstone" (sand size categories). The terms "granular hyaloclastite" and "hyaloclastite breccia" are used for rocks that contain many grains 2–4 mm and >4 mm in size, respectively. The use of genetic nomenclature for the volcaniclastic succession recovered at Site U1348 is based on the assumption that the material recovered is predominantly (altered) hyaloclastite (Table T1). This assumption however, must be verified by further detailed studies.

Paleontology

Calcareous microfossils (nannofossils, planktonic foraminifers, and benthic foraminifers) were examined for core catcher samples as well as for additional section-half samples. Preliminary age assignments were based on biostratigraphic analyses of calcareous nannofossils and planktonic foraminifers. Paleobathymetric interpretations were based on benthic foraminifer assemblages. Where possible, the preservation, abundance, and zonal assignment of each microfossil group were entered into the LIMS database through the DESClogik software. The timescale used for this study is that constructed for Leg 198 (Shipboard Scientific Party, 2002a) (Fig. F4). This timescale is based chiefly on Gradstein et al. (1995) and Channell et al. (1995) for the Cretaceous part. For planktonic foraminifer biochronology, modifications to the Leg 198 timescale were made on the base of the *Leupoldina cabri* Zone (120.5 Ma) and the base of the *Rotalipora globotruncanoides* Zone (98.9 Ma), according to Leckie et al. (2002).

Calcareous microfossil datums

Age assignments for Cretaceous calcareous nannofossil and foraminifer datums (FO = first occurrence or datum base; LO = last occurrence or datum top) are from Erba et al. (1995), Bralower et al. (1997), Premoli Silva and Sliter (1999), and Leckie et al. (2002). Cretaceous datums are graphically presented in Figure F4 and listed in Tables T2 and T3. The ages of a few Cenozoic calcareous nannofossil datums are estimated following Leg 198 (Shipboard Scientific Party, 2002a).

Calcareous nannofossils

Calcareous nannofossil zonal scheme and taxonomy

The zonal schemes of Sissingh (1977; CC zones [modified by Perch-Nielsen, 1985]) and Burnett (1998; UC zones) are used for the Late Cretaceous, and those of Roth (1978, 1983; NC zones) for the Early Cretaceous. For the Jurassic/Cretaceous boundary interval, subdivisions proposed by Bralower et al. (1989; NK and NJK zones) are applied. The zonation used is presented in Figure F4. For consistency with the results from Leg 198, nannofossil taxonomy follows Bown (1999). Full taxonomic lists can be found therein. The zonal scheme of Bukry (1973, 1975 [modified by Okada and Bukry, 1980]) is used for the few stratigraphic alignments of Cenozoic calcareous nannofossils.

Methods of study for calcareous nannofossils

Calcareous nannofossils were examined in smear slides prepared from raw sediment samples. Slides were observed using standard light microscope techniques, under crossed polarizers, transmitted light, and phase contrast at 1000× magnification.

Estimates of the abundance of calcareous nannofossils are

D = dominant (>100 specimens per field of view).

A = abundant (>10–100 specimens per field of view).
C = common (>1–10 specimens per field of view).
F = frequent (1 specimen per 1–10 fields of view).
R = rare (<1 specimen per 10 fields of view).
B = barren.

Preservation of calcareous nannofossils are

VG = very good (no evidence of dissolution and/or recrystallization, no alteration of primary morphological characteristics, and specimens identifiable to the species level).
G = good (little or no evidence of dissolution and/or recrystallization, primary morphological characteristics only slightly altered, and specimens identifiable to the species level).
M = moderate (some etching and/or recrystallization, primary morphological characteristics somewhat altered, and most specimens identifiable to the species level).
P = poor (severe etching or overgrowth, primary morphological characteristics largely destroyed, fragmentation occurred, and specimens often unidentifiable at the species and/or generic level).

Foraminifers

Planktonic foraminifer zonal scheme and taxonomy

The zonation used for Cretaceous planktonic foraminifers (Fig. F4) is based on Caron (1985), Sliter (1989), Robaszynski and Caron (1995), Premoli Silva and Sliter (1999), and Leckie et al. (2002). Cretaceous taxonomic concepts of planktonic foraminifers selectively follow those of Michael (1972), Robaszynski et al. (1984), Caron (1985), Nederbragt (1991), Boudagher-Fadel et al. (1997), Bellier and Moullade (2002), Moullade et al. (2002), Verga and Premoli Silva (2003a, 2003b, 2005), and Petrizzo and Huber (2006).

Benthic foraminifer taxonomy and paleodepth estimation

In this study, identification of benthic foraminifers is made at the genus level. The benthic taxonomic concepts selectively follow Luterbacher (1973), Sliter (1977, 1980), Gradstein (1978), Loeblich and Tappan (1988), Bolli et al. (1994), Widmark (1997), and Holbourn and Kaminski (1997).

Cretaceous paleodepth interpretation is based on Sliter and Baker (1972), Sliter (1977, 1980), Nyong and Olsson (1984), Koutsoukos and Hart (1990), Sikora and Olsson (1991), Jones and Wonders (1992), and Holbourn et al. (2001). The bathymetric terminology follows Sikora and Olsson (1991):

Neritic = ≤200 mbsl.
Upper bathyal = >200–500 mbsl.
Middle bathyal = >500–1500 mbsl.
Lower bathyal = >1500–2500 mbsl.
Abyssal = >2500 mbsl.

Methods of study for foraminifers

Among pelagic carbonate samples (~1–2 cm^3), soft ooze sediments were spray-washed on a 63 µm sieve without any chemical reaction steps, placed in an ultrasonic bath for <1 s, and oven-dried at <50°C. Chalks and limestones were cut into small pieces, soaked in a 3% hydrogen peroxide solution, wet-sieved at 63 µm, sonicated for a few seconds, and oven-dried at <50°C. Indurated or incompletely disaggregated samples were further processed through the glacial (=100%) acetic acid technique (Ando et al., 2009, and references therein) as follows: each sample was oven-dried at ~80°C, soaked in glacial acetic acid for a few hours, quickly transferred to a 63 µm sieve, and washed thoroughly with tap water. The sample was then kept in a beaker full of water until cessation of the chemical reaction, followed by screen-washing and oven-drying.

For mudstones (~3–5 cm^3), each sample was oven-dried at ~80°C and soaked in kerosene for a few hours. After removing excess kerosene, the sample was immersed in boiling water and wet-sieved at 63 µm.

Foraminifer picking and identification were made on the >150 µm size fraction under a stereomicroscope. For pre-Albian samples with smaller planktonic foraminifer test sizes and/or low-abundance benthic foraminifers, the >125 µm fraction was used. For samples with high foraminifer abundance, the sieved fraction was evenly spread on a gridded picking tray, and both planktonic and benthic foraminifers were picked together from the grid transect (~200 specimens). Further collection of benthic foraminifers was made on the entire picking tray.

The following categories were used for description of both planktonic and benthic foraminifer abundance:

A = abundant (≥11 specimens).
C = common (6–10 specimens).
F = few (4–5 specimens).
R = rare (2–3 specimens).
T = trace (≤1 specimens).

The preservation status of foraminifers was estimated as

VG = very good (no evidence of overgrowth, dissolution, or abrasion).
G = good (little evidence of overgrowth, dissolution, or abrasion).

M = moderate (common calcite overgrowth, dissolution, or abrasion).
P = poor (substantial overgrowth or infilling, dissolution, or fragmentation).

Igneous petrology

Physical volcanology

Previous information regarding the nature of volcanism on Shatsky Rise is scant. The best evidence comes from core recovered during Leg 198 (Hole 1213B), which reveals a series of fine-grained, massive volcanic units of several meters thickness. These units were tentatively interpreted as "sills" as a result of their intercalation with sediment and the presence of a few associated chill zones. Also present were rare, smaller volcanic features of <1 m thickness that resemble small (0.1–0.2 m diameter) glass-rimmed pillow lava units. However, there remained considerable speculation regarding the nature of volcanism on Shatsky Rise and, at that stage, it was unclear whether the volcanism conforms more readily to eruptive styles typical of either subaerial or submarine volcanism, or possibly a combination of the two. The combined occurrence of both subaerial and submarine volcanism in the development of submarine large igneous provinces (LIPs) has been previously documented in, for example, the Kerguelen Plateau (Southern Indian Ocean; Frey et al., 2000; Keszthelyi, 2002) and the accreted Wrangellia Terrane (western North America; Greene et al., 2010). Accordingly, Expedition 324 to Shatsky Rise aimed to capture key volcanological elements that would aid in determining the nature and evolution of subaerial and submarine volcanic components in this largely unstudied LIP.

The procedures for core description outlined here are similar to those developed by the ODP Leg 197 Shipboard Scientific Party (2002b), who drilled and cored the Emperor Seamounts. In our initial description of each core we used the nongenetic scheme outlined in Figure F5, but as our knowledge and understanding of Shatsky Rise basement lithostratigraphy improved through description of the core, we evolved a more relevant genetic volcanic classification based on the scheme outlined in Figure F6. The emphasis of our shipboard studies was to produce an integrated picture of the style of volcanism and environmental setting of each site. This was achieved by systematic rock descriptions and identification of key effusive, volcaniclastic, and igneous textures that are known to be diagnostic of specific modern physical volcanic processes. Accordingly, the physical description of volcanic rocks and deposits recovered during Expedition 324 required a multistage process. The first step involved defining boundaries of lithologic units by either visual identification of actual lithologic contacts, or by inference of the position of such contacts using observed changes in volcanic characteristics and/or volcaniclastic features (e.g., chill zones, flow tops, etc.). This was followed by general description of the lithology, lithologic variation, and characteristic igneous textures and vesicle distributions. All of these macroscopic observations were then combined with those from detailed petrographic microscopy of the key igneous units.

Background

Effusive basaltic volcanism in both the subaerial and submarine environment produces a range of common features associated with the development and inflation of flow lobes of varying sizes. Depending on the environment, these include pillow lavas, pahoehoe or rubbly flow surfaces and, where lava interacts directly with seawater, hyaloclastites and breccias. Unsurprisingly, the vast majority of research and literature regarding the evolution of basaltic lava morphologies relates to those observed on land. Continental flood basalt provinces (CFBPs) and other terrestrial eruptions often comprise individual eruptive units consisting of large, internally massive inflation sheets of typically 5–30 m thick, or else an accumulation of numerous stacked flow lobes that build up into single eruptive units of 5–30 m thick (commonly termed simple and compound lavas, respectively) (Walker, 1971). Hawaiian and Icelandic eruptions are also described in terms of surface and cross-sectional morphologies as either pahoehoe or a'a; the development of these morphologies is dependent upon endogenic factors (e.g., eruption rates, viscosity, strain rate, and degree of crystallinity) and exogenic factors (e.g., degree of inclination and topography of the surface upon which the lava propagates). By contrast, submarine eruptions are dominated by stacks of budding and anastomosing pahoehoe-like extrusions resulting in piles of rounded or tubular masses (Batiza and White, 2000), the most readily recognized component of these is the "pillow basalt" often referred to as "pillow lava." However, large inflation units of several meters thickness, as well as more laterally extensive extrusions, have also been observed; both these types have much more "sheetlike" morphologies (e.g., Lonsdale and Spiess, 1980; Mitchell et al., 2008).

Subaerial lava eruptions

Subaerial mafic lavas are commonly divided broadly into a'a- or pahoehoe-type flows (Macdonald, 1953, 1967), each displaying fundamentally different internal and external appearances. The morphological division is important because the mode of lava emplacement for a'a and pahoehoe flows is fundamentally different, this often being a response to differing eruptive environments. A'a flows advance like the treads on a bulldozer, contain a molten core, and are typified by thermally inefficient emplacement in open channels in which solidified lava crusts tend to become disrupted and mixed with the internal molten core. By contrast, pahoehoe inflation units (and their marine equivalent, "pillow lavas") develop an outer viscoelastic crust, and their cores are thus insulated during transport so that, prior to stagnation and cooling, they remain largely molten. The lava is internally transported by pathways within the propagating flows (or within lava tubes) to the active flow fronts, where it advances by inflating lobes with a continuous crust, "buckling," and then by sequential lobe-by-lobe emplacement (Walker, 1991; Hon et al., 1994). A wide range of intermediate flow types exists between the a'a and pahoehoe end-members. However, in drill core, these different types of lava can only be identified if centimeter-scale morphologic features such as glassy rinds, chill zones, and vesiculation patterns at the flow tops and bottoms are well preserved, recovered, and can be placed in context. In both cases, the flow cores are virtually indistinguishable from one another. Importantly, a'a-type flows are uncommon in ocean floor drill core, and the largest submarine flow types appear to be sheet flows or laterally extensive pahoehoe-like inflation units analogous to those found in terrestrial LIPs.

One feature unique to some subaerial lava stacks, as opposed to submarine examples, is the development of flow-top weathering profiles. These are usually apparent through development of oxidative alteration (reddening) that produces iron and aluminium oxyhydroxides. Weathering profiles typically develop during prolonged volcanic hiatuses or on abandoned posteruptive surfaces under suitable climatic and geomorphic conditions.

A'a flows are characterized by angular, spinose clinker at both the flow tops and bottoms (by contrast, pahoehoe flows are often characterized by smooth surfaces and sharp contacts between successive and/or adjacent units). Internal disruption during emplacement permits efficient degassing, and the crust, core, and base of a'a flows are therefore typically sparsely vesicular or nonvesicular. Transitional flow types (e.g., rubbly, slab, or toothpaste pahoehoe; Guillbaud et al., 2005) show some of the characteristics of both a'a- and pahoehoe-type flows.

Pahoehoe lavas are usually vesicular, often highly so, and frequently exhibit bulk porosities in excess of 20 vol% (typical range is from 20 to 60 vol%). Thin pahoehoe lobes (e.g., < 0.5–1 m) are often vesicular throughout and exhibit a gradual coarsening in vesicle size from the lobe margins toward the interior (Wilmoth and Walker, 1993). During development of pahoehoe lava fields, gas bubbles can frequently become trapped and entrained in the magma body as it cools from both above and below. Thus, thicker, inflated pahoehoe lobes of 5–30 m thickness, such as those documented in CFBPs, are often characterized by the threefold structure of a vesicular upper crust, a dense core, and a thinner vesicular lower crust (Aubele et al., 1988; Thordarson and Self, 1998; Jerram and Widdowson, 2005).

Subaerial eruptions entering water bodies and shallow subaqueous eruptions

Subaqueous lava flows and hyaloclastite associations have been documented where flows from land-based eruptions entered water (e.g., into the sea or freshwater lakes) or else are erupted directly into shallow submarine settings (e.g., ongoing eruption flowing from Pu'u 'O'o, Hawaii; units of the Miocene Columbia River Basalt CFBP, which entered the sea; submarine magmatism associated with the emergence of the Surtsey eruptions, 1963–1967; and around the coasts of the Azores). On entering water or soft unconsolidated (e.g., wet) sediments, the eruptive style changes fundamentally and, depending on local conditions, advancement of the lava front typically generates either pillow basalt, hyaloclastites, peperites, or a combination of all three. Hyaloclastites and peperites are volcaniclastic sediments that form by quench fragmentation (Carlisle, 1963). Pillow basalts are a common product of these environments but can usually be distinguished from terrestrial pahoehoe inflation units by their much thicker glassy rinds (a consequence of a more efficient aqueous quenching process), and by the presence of lacustrine or marine sediments preserved in and between the pillows. Although less frequently documented, larger subaqueous flows may also be massive and sheetlike. Overall, the progression from pillow basalt to massive flow seems largely controlled by local flow rate, which is itself a function of effusion rate and topographic slope (Walker, 1992; Gregg and Fink, 1995).

Submarine lava eruptions

Submarine lavas are important because they represent the most abundant igneous rock on the surface of Earth, forming most of the ocean floor. As indicated, a close morphological similarity exists between pillow lava formed under water and pahoehoe lava formed on land, though the latter typically lacks, or has only a relatively thin glassy rind (i.e., glassy surface selvage). Submarine pillows occur at a variety of depths, are the product of a variety of volcanic settings (e.g., ocean spreading centers, off-ridge and isolated seamount edifices, and submarine portions of ocean islands and oceanic plateaus), and accordingly display a range of extrusive combinations and forms (Batiza and White, 2000). They are, for the most part, inaccessible to conventional observational methods (Lonsdale and Spiess, 1980; Mitchell et al., 2008) and so, by contrast with their subaerial counterparts, are relatively poorly documented.

As with subaerial examples, the eruptive styles of submarine lava flows are largely controlled by effusion rate and the local topography and slope onto which lava eruption takes place (e.g., Greg and Fink, 1995; Mitchell et al., 2008, and references therein). Basaltic magma typically erupts at relatively high temperatures and characteristically is fluid (low viscosity), allowing its relatively high gas content to be released effectively during lava emplacement. These gases may be preserved as vesicle layers and pipes that are often characteristic of submarine basaltic materials. However, because of increasing hydrostatic pressure with increasing depth of the seafloor, the degree of vesiculation decreases in deeper water eruptions (Dixon, 1995; Wallace, 1998). High hydrostatic pressure may also limit the possibility of explosivity from either gas release or steam generation caused by contact flash-heating of water upon the nascent lava. At depths deeper than 3 km, the hydrostatic pressure exceeds the critical pressure of water, effectively preventing steam explosions. Accordingly, pillow basalt formed in the upper 1000 m of the water column more commonly consists of moderately to highly vesicular lava and may show evidence of gas fracturing or fragmentation, whereas pillow basalts formed in much deeper water can usually be distinguished by a significantly lower vesicularity (<5 vol%), less fracturing and, occasionally, by the presence of pelagic rather than neritic marine sediment preserved in between the pillows.

Pillow lavas and massive inflation units

Pillow lavas are subaqueous extrusions resulting from individual budding, inflation, and separation of lava “pods” from point sources along an advancing lava front. They can accumulate in a variety of styles, depending upon effusion rate, number of point sources, and internal plumbing architectures within the growing volcanic edifice. However, pillows typically consist of discrete subrounded units of relatively small size (from ~0.2 to <1.0 m diameter), and, characteristically, their exteriors are entirely bounded by glassy rinds as a result of rapid cooling; their interiors often display internally radiating vesicle and joint patterns generated during solidification by cooling and contraction.

Larger single inflation units (~1–2 m diameter) can also develop (sometimes termed “lobate flows”) by the same endogenous inflation process. Although these extrusions broadly resemble pillow lavas, they differ in that they have massive, coarser grained, and sparsely vesicular cores, often with pipe vesicle domains. The larger size permits a slower rate of cooling, more effective degassing, and maturation of the internal vesicle patterns. Accordingly, vesicle zoning is more concentrated in the upper regions of these types of inflation units and often occurs as a series of vesicle bands that develop through the inward migration of the cooling front; by contrast, the lower part of the inflation unit typically contains either sparse, poorly defined vesicle banding and/or “teardrop” shaped vesicles at or just above the basal chill zone. Rather than having spherical or subspherical shapes, these “massive inflation units” tend to have flattened, oblate, or tubular shapes and are most probably generated as a series of interconnected semi-adjacent inflation “pods” fed simultaneously by internal plumbing. Their size and morphology are considered to be indicative of a higher effusion rate than that which generates pillow lavas. Individual units can cover an area of several square meters or significantly more where adjacent units merge either through internal plumbing conduits or as a result of rupture and coalescence. In those instances where they merge into a single entity, submarine images reveal they can develop a continuous lava flow surface displaying a dominantly botryoidal morphology.

“Massive flows” are thick (several meters or more) and are often laterally extensive, forming “sheetlike” and internally massive basalt units (van Andel and Ballard, 1979). They have a variety of surface features generated by deformation and disturbance of the solidifying lava crust while in a plastic/semiplastic state. Dimensions and internal features of massive flows can resemble those of larger subaerially erupted flows (e.g., those found in continental flood basalt provinces). These types of flows may be fed internally and achieve their size and extent by internal inflation and/or marginal budding. They often have texturally uniform massive cores, as thick as several meters, and are characterized by sparse vesicle layering and/or vertical vesicle pipes containing late-stage melt segregation material. Massive or sheetlike flows are most probably a response to particularly high effusion rates and/or local slope and other controlling topographic conditions. In the literature, these unit types are often termed “sheet flows,” though this term implies a significant degree of lateral extension that cannot be determined readily from core alone. Nevertheless, in cases where recovered units are significantly thicker than that expected for the normal dimensions of pillow lava or lobate flows (~0.2–2 m) we prefer the nongenetic term “massive lava unit,” an appellation that also avoids any confusion with the term “sheet flow” as employed in the CFBP literature.

Volcaniclastic deposits

Volcaniclastic deposits include a range of materials from rubbly, in situ volcanic debris to resedimented materials such as volcanic sands or tuffs (Figs. F5, F6). Volcanic materials of all sizes may be the direct products of eruptive processes (pyroclastic) or accumulations through processes involving transport, sorting, and (re)deposition (epiclastic). Pyroclastic material includes hydrovolcanic deposits formed by explosive interaction between magma and water as well as nonexplosive quench fragmentation processes (e.g., hyaloclastite and peperite). Epiclastic volcanic sediment forms by redeposition of volcanic detritus typically produced by erosion and/or transport of volcanic rocks.

Hyaloclastite literally means “glass-fragment rock” and includes all glassy fragmental debris formed by eruptions in which water has been involved. Hyaloclastite-producing environments of relevance to Shatsky Rise may include shallow-water phreatomagmatic eruptions that are generated at newly emergent volcanic islands and, most probably, volcaniclastic materials associated with the development and advancement of submarine lavas at greater water depths (Clague et al., 2009). Phreatomagmatic conditions can result in fragmentation of gas bubbles inflated by steam, producing on deposition thick layers of glass shards (i.e., syneruptive sedimentation). These shards may be sent into subaerial trajectories, or else form suspended “plumes” within the water column. In either case, the shards later settle on the surrounding land or seafloor, or are transported and deposited elsewhere (i.e., epiclastic sedimentation).

Depending on the nature of the eruption, welded and unwelded volcanic rubble and breccia also occur in these environments (Fisher and Schmincke, 1984). Submarine lavas are almost invariably associated with hyaloclastites and a variety of other fragmental volcanic debris, including breccias (Staudigel and Schmincke, 1984; Batiza and White, 2000). Hyaloclastite is rare at mid-ocean ridges but more common at seamounts where it may be the product of granulation by cooling contraction and surficial spalling of lava pillows and pods. Those environments characterized by volcanic breccias are also commonly associated with mass debris flows at various scales, and especially where the eruption occurs on significant seafloor topography.

Peperite is a distinct volcanic sediment facies occurring where submarine basaltic lava flows interact with unconsolidated sediment as they erupt into water or, more commonly, onto the seafloor (Skilling et al., 2002). The mingling of basaltic lavas and wet sediments produces distinct volcanic textures resulting from the physical interaction of lava and sediment (entrainment, baking, folding, chilling, etc.), as well as physical and chemical fragmentation and alteration through steam-rock interaction during flash heating of the water. Common features include quenched margins of basaltic lava clasts surrounded by sediment, as well as basaltic clasts with a variety of fragment morphologies, including “fluidal” (i.e., where fragments remained plastic enough to deform after deposition) or “jigsaw-fit” (i.e., where cooling and contracting fragments crack apart in situ). Lava-sediment interactions include features involving the mixing or mingling of molten or plastic lava with soft sediment, creating deformation features where lava injects or intrudes the seafloor substrate. In some instances, a lack of bedding or lamination is observed in sediments adjacent to pillow lavas or in the materials surrounding lava injections. A likely explanation is that fluidization of the fine-grained sediment, attributable to flash heating and vaporization of sediment pore water, took place during emplacement of the lava (Kokelaar, 1982). Such momentary fluidization causes sediment reconstitution, localized transport, redistribution, and, hence, the destruction of any original bedding structures.

Palagonite is a typical alteration product resulting from the interaction between water and basalt melt and is commonly associated with peperite volcanic facies where the small fragments of lava have reacted with the steam. Accordingly, the presence of peperites and their textures can provide important information regarding the nature of the eruptive environment because their occurrence is taken as evidence that the volcanism and the affected sedimentary environment existed contemporaneously.

Definition of lithologic units and volcanic successions

Our primary aim was to design an observational framework that permitted logging and recording of key data while avoiding nomenclature or terminologies that might incorrectly imply particular styles of effusive basaltic volcanism. Most lava type classifications are derived from land-based observations that consider both the lateral and vertical variations of eruptive units as well as their stacking relationships. Such refined classifications are neither realistic nor justifiable from core observation alone and may only become achievable through integration of multiple data sources alongside the core log description (e.g., petrography, downhole logging data, geochemical and paleomagnetic results, etc.). However, lithofacies associations provide one such avenue of nongenetic description that have been successfully applied to the description of a range of LIP types (e.g., Jerram and Widdowson, 2005; White et al., 2009) and therefore can assist in the interpretation of cored volcanics; the Wrangellia LIP is a particularly useful analog for Shatsky Rise (Fig. F7) because this example contains products of both submarine and subaerial eruptions, as well as instances where one passes into the other (Greene et al., 2010). Accordingly, we employ the term "stratigraphic unit" to describe successions of similar volcanic facies types such as pillow-lava stacks, packages of sheet flows, or hyaloclastic successions. Such lithologic units may often be petrogenetically or volcanically related, having developed as part of a single eruptive event. For instance, during advancement of a submarine flow, a hyaloclastite succession might evolve into a pillow basalt stack and then sheet flow successions; also, such facies associations can arise through natural lateral variation of eruption style across a single lava field. However, in the case of cored basaltic successions, these types of volcanic and petrogenetic relationships often become apparent only after consideration of additional petrographic, geochemical, or downhole logging data. In most instances, core material only permits identification of the smaller volcanic "lithologic" unit divisions (e.g., pillow unit, massive flow unit, etc.), so these are necessarily the basic unit of our descriptions.

Descriptive nomenclature

To aid efficient core description and enable later collation of the observed volcanic units into volcanologically meaningful successions (stratigraphic units), we adopted a simple two-fold numerical hierarchy. The term "lithologic unit" is adopted to define smaller features on the basis of criteria including the presence of lava contacts, chilled margins or identifiable flow tops, vesicle distributions, and intercalated volcaniclastic or sedimentary horizons. When considered together, these features typically define the key volcanic cooling or inflation units of various sizes and scales within the larger eruptive stratigraphy. Lithologic units identified during core logging are given consecutive downhole Arabic numbers (i.e., lithologic Units 1, 2, 3, etc.), irrespective of whether they are pillow, sheet, or massive flow types (i.e., a nongenetic cataloging system).

The term "stratigraphic unit" is applied where successions of consecutive cooling or inflation units of similar or shared evolutionary characteristics can be identified. In effect, these stratigraphic units combine similar types of eruptive products and provide a first step toward considering the volcanic stratigraphy in terms of packages of genetically related lithologic units and, ultimately, understanding the evolution of the volcanism. These packages are given consecutive downhole Roman numbers (i.e., stratigraphic Units I, II, III, etc.). Although we made every effort to ensure that the identified stratigraphic unit boundaries reflect individual lava packages or eruptive units, the term should not be considered as synonymous with a single eruptive event, but rather as a method of dividing the retrieved core into elements or sections displaying broadly similar volcanic characteristics (i.e., lithofacies type).

The most unequivocal evidence for dividing core into lithologic units is the presence of flow-to-flow contacts. Unfortunately, such contacts are not always common in low recovery sections. Alternatively, the presence of glassy material or fine-grained chill zones can provide a useful proxy for determining the presence or estimating the position of unit boundaries. Of particular use in sections of poor core recovery, or where the interior-most massive sections of units are preferentially recovered, are the changes in vesiculation that occur through inflation or cooling units of all sizes. To identify or estimate the position of lithologic unit boundaries using this method, we paid special attention to vesiculation characteristics by measuring or estimating (1) percentage volume of vesicles, (2) average vesicle size, (3) vesicle shape and sphericity, and (4) variations in vesicle sizes (i.e., fining or coarsening upward), these being examined at intervals appropriate for the variability shown by the core (typically across 10–100 cm intervals). The volume fraction of vesicles within the unit or section under consideration, together with modal shape and sphericity of vesicle populations, were estimated using appropriate comparison charts similar to those used by sedimentologists for determining grain size populations (i.e., Wentworth, 1922, classification scheme). Maximum and modal vesicle sizes were determined using a hand lens with a submillimeter graticule; in fact, it proved impractical to measure the minimum size since it always proved to be below the realistic limit of visual resolution.

In order to develop and refine this approach, we initially employed it for the description of archive core recovered from the previous Shatsky Rise expedition (Leg 198, Cores 198-1213B-28R through 33R). These cores were examined by the Expedition 324 shipboard party immediately prior to commencement of drilling, and the volcanologic and petrographic observations were recorded in templates that we designed and collated within the new descriptive data capture application (see **"DESClogik: the new core description software for descriptive data capture"**). From this application, data were uploaded into the LIMS database and used to generate hard rock VCD graphic reports (Figs. F8, F9). As far as possible, we sought to design the DESClogik templates (Fig. F10) in a manner that would ensure that the type of data recorded would be consistent with the volcanologic logging procedures described for ODP Legs 183 and 197 (Shipboard Scientific Party, 2000a, 2002b).

Lithology

Porphyritic basaltic rocks were named according to major phenocryst type, but only in those instances where the total abundance of phenocrysts was >1% (e.g., plagioclase basalt or olivine-pyroxene basalt). Aphyric rocks were not assigned any mineralogical modifier and retained instead a textural description (e.g., aphyric basalt). The term "phenocryst" was used for any crystal that was >1 mm in width and significantly (typically five times) larger than the average size of the groundmass crystals and that was euhedral or subhedral in shape. The term "microcryst" was used for crystals that were larger than the modal groundmass grain size but <1 mm. Where macroscopic observation was possible, microcrysts were also described in the DESClogik database under a suitable heading in the phenocryst table (Fig. F10A). The phenocryst abundance descriptors were further modified by including the names of phenocryst phases in order of increasing abundance. If the abundance of a particular type of phenocryst was >5% the mineral name was included without a modifier, whereas all other phenocryst names included a modifier; "olivine-bearing," for example. Thus an olivine-bearing plagioclase basalt (ol-bearing plag basalt) may contain 10% plagioclase and 1% olivine phenocrysts.

Volcanic units were identified using the criteria outlined above, and appropriate data were entered into the DESClogik database under the Volcanic Attributes tab (Fig. F10B).

Volcaniclastic deposits

We used "volcaniclastic" as a nongenetic term for any fragmental aggregate of volcanic parentage containing >60% volcaniclastic grains and <40% other types of clastic and/or biogenic material. This definition is necessarily broader than that typically used for pyroclastic deposits because the term "pyroclastic" normally applies only to products of explosive volcanic activity, including hydroclastic deposits formed by explosive interaction between magma and water/sediment and nonexplosive quench fragmentation (i.e., hyaloclastite and peperite). Our adopted definition also includes the volcanic detritus produced by erosion and/or transport of volcanic materials (i.e., epiclastic sediment). Accordingly, the term "volcaniclastic" does not necessarily imply active volcanism at the time of deposition (Fig. F6).

In fragmental lava facies we documented volcaniclastic textures using standard sedimentologic techniques (such as clast versus matrix modal proportions, clast size, shape, sorting, and lithology) (Fig. F5). Of particular interest was the presence (or absence) of features diagnostic of viscous or quench fragmentation while the lava was hot. These include clasts engulfing fragments of other (earlier) clasts, welding, glassy margins surrounding clasts, extensions of the interior of the flow into breccia, entrained clasts within the interior of the flow, and the presence of a basal breccia. We used changes in clast morphology and crystallinity as well as changes in vesicle abundance and shape to identify clast types within breccia.

The subclassification of volcaniclastic sediment followed during Expedition 324 differs from the standard ODP classification (Mazzullo et al., 1988) in that we adopt a descriptive (nongenetic) terminology similar to that employed during Leg 197 (Shipboard Scientific Party, 2002b). Unless an unequivocally pyroclastic origin for volcanogenic materials could be determined, we simply described deposits composed of these materials as being of volcanic provenance (i.e., volcaniclastic) according to the classification scheme for clastic sediment, noting the dominance of volcanic grains. We followed the clastic textural classification of Wentworth (1922) to separate the various volcanic sediment types and sedimentary rocks (according to grain size) into volcanic gravel (>2 mm), volcanic sand (2–0.0625 mm), volcanic silt (0.0625–0.0039 mm), and volcanic clay (<0.0039 mm).

For coarse-grained and poorly sorted volcaniclastic sediments, including those produced by gravity currents, we applied the terms "volcanic breccia" (angular clasts) or "volcanic conglomerate" (rounded clasts) and used lithologic or structural modifiers for further description.

Where appropriate and possible, we further classified volcaniclastic sediment by adding major and minor modifiers to the designated principal name. The principal name defines the grain size class (e.g., gravel, sand, silt, or clay). Relative proportions of vitric (glass), crystal (mineral), and lithic (rock fragment) components of the sediment are used to determine additional modifiers in the name and are placed before the principal name. For example, volcanic sand composed of 75% glass, 5% feldspar crystals, and 20% lithic fragments is named vitric-lithic volcanic sand. Where the evidence for a pyroclastic origin was compelling, we adopted the classification scheme of Fisher and Schmincke (1984). In these instances we used the grain size terms volcanic breccia (>64 mm), lapilli/lapillistone (2–64 mm), and ash/tuff (<2 mm). Sedimentary structures recorded in Shatsky Rise volcanic sediments included graded bedding, cross-bedding, planar laminations, foreset bedding, dune forms, and ripples (and bioturbation). However, although these descriptions were entered into the igneous database, the VCD for sedimentary rocks was typically employed to record the detail for core sections consisting predominantly of volcaniclastic material. This approach ensured efficiency during the logging and description of newly retrieved core material.

Core and thin section descriptions

The first step in describing the recovered core was the identification of unit boundaries on the basis of changes in lithology, including color, grain size, the presence of volcaniclastic or sedimentary intercalations, volcanological features (e.g., presence of contacts or chilled margins), vesicle distribution patterns, changes in primary mineralogy (occurrence and abundance of plagioclase, pyroxene, olivine, and oxide minerals), structure, and alteration. Unit boundaries of volcanic rocks were chosen to reflect different volcanic cooling or volcaniclastic units (see **"Definition of lithologic units and volcanic successions"**). In some cases, limited recovery required interpolation for the placement of unit boundaries. Of fundamental importance to the core interpretation was the additional use of digital image printouts of the archive core halves. During core processing, these printouts are generated as a matter of course on the split core using the SHIL. Annotation of the printouts provides a working record onto which observation notes, sketches of key features, or an indication of shipboard sampling or analytical requirements may easily be made. In effect, this approach mimics the type of observation and note-taking that is familiar to field-based geologists. This visual record also proved invaluable during the preparation of site reports because it provided the type of sequential context and visual cues that help in assembling and describing broader stratigrahic relationships. Scanned files of these handwritten records are available from the Expedition Project Manager/Staff Scientist.

For thin section descriptions, all minor variations in texture, grain size, vesicularity, color, and/or mineralogy, as well as important volcanic features (e.g., chilled margins, concentration of glomeroporphyritic clots, or crystal aggregates) were recorded in the LIMS database using the DESClogik software interface (see Fig. **F11** for an example). The VCDs thus provide summary information regarding the position of igneous unit boundaries and also include a brief description of each section and associated lithologic boundary, if captured.

Macroscopic visual core description

We used the DESClogik data entry software to document each section of the igneous rock cores and to store the descriptions in the LIMS database. To provide consistency in approach, the procedure and database templates we designed closely follow the methods for core descriptions from previous IODP volcanic basement expeditions, including the Kerguelen Plateau, Hawaii-Emperor Seamounts, and Superfast Spreading Crust legs (Legs 183 and 197 and Expedition 309/312; Shipboard Scientific Party, 2000a, 2002b; Expedition 309/312 Scientists, 2006).

VCD graphic reports were automatically generated to summarize each section of the igneous rock cores (Fig. **F8**). The VCD report displays, from left to right,

1. The core depth in meters;
2. A scale for core section length of 0–150 cm, or as appropriate;
3. The sample piece number;
4. A scanned digital image of the core archive half;
5. An arrow indicating the upward direction for oriented pieces;
6. The sample type and position of intervals selected for different types of shipboard analytical study, including locations of thin sections made;
7. The number of the identified lithologic units;
8. Symbols summarizing structural information;
9. Measurements of strike and dip;
10. A line chart displaying measured and recorded percent vesicularity;
11. A stacked line chart displaying phenocryst percentage for plagioclase (pl, red line), olivine (ol, green line), and pyroxene (px, blue line);
12. A line chart displaying variation in the modal crystal size of groundmass (in millimeters), with presence of fresh glass (f) or altered glass (ag) indicated;
13. A pattern depicting alteration intensity;
14. A column-measured intensity for point-source (MS point) and whole-round (MS) magnetic susceptibility (raw and filtered); and

15. Line chart displaying recorded point-source color reflectance with the red line (L*) and blue line (b*) stacked one on top of the other.

Additionally, the VCD contains written descriptions to accompany the schematic representation of the core sections. These include the following information:

1. The expedition, site, hole, core, type, and section number (e.g., 324-U1346A-15R-3) and the top of the core section measured in meters.
2. The lithologic unit number (numbered consecutively downhole), the piece numbers, and on which piece or pieces the description was based.
3. The lithology (rock description and name). Rock description nomenclature was achieved from hand specimen observation using the eye, hand lens, and binocular microscope.
4. Volcanic description based upon the type of unit or part of unit (e.g., pillow lava, massive flow, etc.). Units were identified using the presence of glassy margins, groundmass grain size variations, and vesicle-rich bands. An interval was described as massive if there was no evidence of variation in internal structure.
5. Rock texture (whether the rock was phyric or aphyric and, if present, phenocryst types).
6. Modal color determined on wetted rock surfaces.
7. Phenocryst content and type based upon minerals identifiable by naked eye, hand lens, or binocular microscope.
8. Groundmass grain size and texture. Categories are as follows: glassy/cryptocrystalline (<0.1 mm), microcrystalline (0.1–0.2 mm), very fine grained (0.2–0.5 mm), fine grained (0.5–1 mm), medium grained (1–2 mm), coarse grained (2–5 mm), and very coarse grained (>5 mm) (Fig. **F8**).
9. Presence of vesicles. Data entered are (a) the percentage volume of vesicles, (b) their shape and sphericity, and (c) changes in vesicle sizes (i.e., fining or coarsening upward) or vesicle patterns within the unit. Volume fraction, modal shape, and sphericity of vesicle populations were estimated using amended comparison charts (based upon Wentworth, 1922).
10. Contact relations and boundaries in the upper and lower parts of units, as based on the physical changes observed in the core material (i.e., presence of chilled margins, changes in vesicularity, alteration, etc.) and information regarding their position within the section. "Not recovered" was entered where no direct contact was recovered (e.g., if igneous contact was otherwise inferred using proxy observations such as a chilled margin or changes in vesicularity).
11. Presence of alteration. Alteration was based on estimated percent of alteration products by volume, and categorized as follows: unaltered (<2%), slight (2%–10%), moderate (10%–40%), high (40%–80%), very high (80%–95%), and complete (95%–100%). This section includes comments regarding degree and type of vesicle infilling. See **"Alteration and metamorphic petrology"** for details.
12. Occurrence and type of mineral filling of veins. Additional detailed information of vein materials and orientation descriptions are reported in **"Alteration and metamorphic petrology"** and **"Structural geology."**
13. A general structural summary statement regarding the volcanic structure and/or comments regarding the nature of the igneous contact or other internal structures not described under previous headings.

Microscopic visual core description

Thin section analyses of sampled intervals were used to complement and refine macroscopic core observations. Typically, at least one thin section was examined and logged per defined lithologic unit. To capture the descriptive information, a specialized DESClogik template was created. For an example of a thin section description sheet, see Figure **F11.** As far as was practically possible, the same terminology and nomenclature hierarchy employed for the visual core compositional descriptions was also used for the thin section descriptions. The textural terms used were those defined by MacKenzie et al. (1982). Phenocryst assemblages and their modal percentages and sizes, groundmass, and alteration phases were determined and textural descriptions constructed.

Alteration and metamorphic petrology

Alteration characteristics of cores were described on the archive halves of the core, using petrographic description of thin sections and XRD analyses (bulk rock, veins, and vesicle infillings). Alteration was then presented as a component of the VCDs.

DESClogik: the new core description software for descriptive data capture

A new software program, DESClogik, first implemented and assessed during Expedition 320T for core logging, thin section description, and database compilation, was used during Expedition 324. Prior to drilling operations, two spreadsheet templates were constructed and customized in order to record alteration characteristics. These spreadsheet templates were based on the methods and guided by the recorded observations of ODP Leg 192 and IODP Expedition 304/305 (Mahoney, Fitton, Wallace, et al., 2001; Blackman et al., 2006). The first of these spreadsheet templates was used to record alteration by visual core description (Fig. **F12**), and the second template was used to record descriptions of veins (Fig. **F13**).

Core logging

Description of alteration of the archive half of the core provides information on alteration of primary igneous features including phenocrysts and groundmass secondary mineralogy, veins, and infilling material in vesicles. Information on the extent of replacement of igneous minerals and groundmass by secondary minerals and, where possible, the nature and approximate modes of secondary mineral assemblages are recorded using DESClogik. The presence of veins or vesicle infill and their description and mineralogy are also recorded using DESClogik.

Visual estimates of alteration degree, type, color, textures (e.g., halos and patches), abundance (%) of mineral filling vesicles, and the proportion of altered groundmass and phenocrysts were recorded in the alteration and vein logs of DESClogik. Most of the secondary mineral assemblages were composed of clays that were difficult to identify macroscopically; therefore, a general descriptive term such as “brown clay” was used.

Alteration degree is defined and reported graphically on the VCDs according to various ranges of intensity (Fig. **F8**):

Fresh = (<2 vol%).
Slight = (2–10 vol%).
Moderate = (10–50 vol%).
High = (50–95 vol%).
Complete = (95–100 vol%).

Alteration color was defined based on Munsell Soil Color Charts (Munsell Color Company, 1994) and converted to a more intuitive color name. Precise color identification using Munsell Soil Color Charts was recorded in the DESClogik template of the Igneous Petrology group (see **“Igneous petrology”**). Quantification of individual mineral modes was estimated by investigating the archive-half core under a binocular microscope. A distinction was made between overprinting alteration assemblages and assemblages localized by preexisting lithology changes. For example, a core of altered basalt containing a subinterval with vein halos would be described using two rows, one long interval of altered basalt within the alteration tab of DESClogik (Fig. **F12**) and a shorter subinterval containing the overprinting vein halo assemblage within the vein tab of DESClogik (Fig. **F13**).

Veins are recorded according to their location, apparent orientation, width, length, and mineralogy (Fig. **F13**). Textures were recorded in DESClogik using a series of codes (Fig. **F14**) in terms of vein shape (straight, sigmoidal, irregular, pull-apart, and fault vein), connectivity (isolated, single, branched, and network), texture (massive, cross-fiber, slip-fiber, vuggy, and polycrystalline), structure (simple, composite, banded, haloed, and intravenous), and geometry (en echelon, ribbon, and cross fractures).

Thin section description

Thin section descriptions were recorded using DESClogik and subsequently uploaded to the database. Secondary mineral assemblages and replacement relations to primary phases were described, as well as secondary modes (Fig. **F11**). Mineralogy of veins and vesicles, as well as cement when present in basaltic breccia, was also reported in the database. The modal estimates of the secondary minerals allowed characterization of alteration intensity.

X-ray diffraction

Phase identification in selected samples of whole-rock shipboard powders and vein and vesicle material was aided by XRD analyses using a Bruker D-4 Endeavor diffractometer with a Vantec-1 detector using nickel-filtered CuKα radiation. Instrument conditions were

Voltage = 35 kV.
Current = 40 mA.
Goniometer scan (bulk samples) 2θ = 3°–70°.
Step size = 0.015°.
Scan speed = 0.2 s/step.
Divergence slit = 0.3 mm.

Structural geology

Structural geology was an important facet of visual core description during Expedition 324. The priorities set by the structural geologists were

1. To document all structures in the core and record evidence for the relative timing of the various structures and other processes such as magmatic cooling, tectonic processes, and hydrothermal alteration;
2. To record the orientation of all structures on the core face frame and, where possible, to orient these in three dimensions in the core reference frame;

3. To obtain evidence from the style, geometry, and microstructure of individual structures that might bear upon the processes and conditions of deformation and the finite strain that can be inferred; and
4. To construct plausible models of the tectonic environment from all of these data.

This section outlines the techniques used for macroscopic and microscopic description of structural features observed in hard rock basement cores. Conventions for structural studies established during Expedition 309/312 (Teagle et al., 2006) and ODP hard rock drilling (Leg 118, Shipboard Scientific Party, 1989; Leg 131, Shipboard Scientific Party, 1991; Leg 135, Shipboard Scientific Party, 1992c; Leg 140, Shipboard Scientific Party, 1992b; Leg 141, Shipboard Scientific Party, 1992a; Leg 147, Shipboard Scientific Party, 1993b; Leg 148, Shipboard Scientific Party, 1993a; Leg 153, Shipboard Scientific Party, 1995; Leg 176, Shipboard Scientific Party, 1999; Leg 206, Shipboard Scientific Party, 2003b) were generally followed during Expedition 324. However, several minor changes in nomenclature and procedure were adopted.

Graphic symbols and terminology

All material from both working and archive halves was examined, although the records of the structures and orientation measurements were made on the archive half. The most representative structural features in the cores recovered during Expedition 324 are summarized on the VCD form (see "Core descriptions"). For some important sections, more detailed structural information is described and sketched on a separate Structural Geology Description form (Fig. F15). All structural data were entered in structural spreadsheet logs using DESClogik, with reference to the structural geology and symbols checklist (Fig. F8; Table T4).

We used a set of structural feature "identifiers" in order to maintain consistency of core descriptions. Brittle deformation identifiers include joint, vein, shear vein, fault, and breccia. Identification of these features is based on the presence of fractures, filling phases, and evidence of shear displacement. The terminology adopted generally follows that of Ramsay and Huber (1987), Twiss and Moores (1992), and Passchier and Trouw (1996) and is consistent with the terminology used during Leg 153 for brittle deformation (Shipboard Scientific Party, 1995). Some of the terms (Teagle et al., 2006) and symbols commonly used in the structural description are sketched in Figures F8 and F16:

1. Igneous contacts (demonstrably extrusive or dike contact),
2. Lineation (preferred orientational minerals in the shear zone, oriented minerals in magmatic foliation, or slickenlines in the fault surface),
3. Magmatic fabric (lineations and foliations, referred to as magmatic foliation when recognized, defined by shape-preferred orientation of primary minerals with no evidence of crystal-plastic deformation),
4. Magmatic foliation (shape-preferred orientation of primary minerals with no evidence of crystal-plastic deformation),
5. Shear veins (obliquely opening veins with minor shear displacement filled with slickenfibers or overlapping fibers),
6. Veins (extensional open fractures filled with secondary minerals),
7. Fractures (brittle failure with or without displacement),
8. Joints (fractures where the two sides show no differential displacement [relative to the naked eye or 10× pocket lens] and have no filling material), and
9. Faults (fractures with kinematic evidence for shear displacement across the discontinuity or with an associated cataclasite; we adopted the term "microfault" when the scale of the offset is millimetric).

This division of structures does not imply that all features fall into distinct and exclusive categories. We prefer to use the term "veins" for all healed fractures, avoiding the usual division based on fracture width (e.g., Ramsay and Huber [1987] defined veins as having >1 mm filling material), mainly to be consistent with the DESClogik alteration vein log template. Rigid boundaries between the adopted structural categories do not exist. Where necessary, details specific of structural features are illustrated with comments and sketches.

Brecciated core intervals are described in detail in a separate structural template in DESClogik, in which the compositional and textural features of the breccias are recorded. Where common types of breccia can be unambiguously recognized, such as fault-related, hyaloclastite, or hydraulic breccia, a note was added in the Comments column. Data on the composition and alteration of both veins and breccias were integrated with the Alteration and Vein Logs (see "Alteration and metamorphic petrology").

Geometric reference frame

Structures are measured on the archive half relative to the core face frame and core reference frame based on previous ODP/IODP procedures (Leg 141, Shipboard Scientific Party, 1992a; Leg 206, Shipboard Scientific Party, 2003b; Expedition 309/312 Scientists, 2006). The plane normal to the axis of the borehole is referred to as the horizontal plane. On this plane, a 360° net is used with a pseudosouth (180°) pointing out of the archive half and a pseudonorth (0°) pointing into the archive half and perpendicular to the cut surface of the core (Fig. **F17**). The cut surface of the core, also called core face or cut face, therefore is a vertical plane striking 90°–270°.

Apparent dip angles of planar features were measured on the cut face of the archive half of the core. To obtain a true dip value, a second apparent dip reading was obtained where possible in a section perpendicular to the core face (second apparent orientation). The dip and the dip direction with respect to the archive half of the core are recorded on the spreadsheet together with second plane measurements. If the feature intersected the upper or lower surface of the core piece, measurements of the strike were made directly in the core reference frame and combined with the apparent dip measurements to calculate the true dip values.

However, for the long term we should recover real orientation of the structures. Therefore, following the recording of orientation data on the descriptive sheets as outlined above, it would be desirable to convert these local orientations to geographical coordinates. The multishot and Formation MicroScanner (FMS) logging techniques allow cores to be oriented with respect to magnetic north and allow the arbitrary local reference frame to be positioned. A paleomagnetic approach can be also employed. It is especially useful for cores obtained by RCB drilling because these techniques often cause the core to break into several pieces that rotate independently of each other within the core liner. To remove these drilling-induced rotations, FMS data could be gathered from sections of core that were considered to be structurally continuous.

Thin section description

Thin sections of basement rocks recovered during Expedition 324 were examined in order to (1) confirm macroscopic descriptions of brittle structures; (2) characterize the microstructure of the rocks; (3) provide information on the kinematics of brittle and brittle-ductile deformation; (4) identify time relationships between deformation, magmatic, and alteration processes and the relatively temporal sequence between different veins and joints; and (5) document downhole variations of structured zones.

The microstructural notes were entered into the DESClogik Thin Section Description template (see **"Igneous petrology"** for details of the template). For the description of microstructures we primarily applied the terminology of Passchier and Trouw (1996). Shipboard thin sections were generally oriented; the orientation is given relative to the core reference frame and was marked on each thin section by an arrow pointing upward. Digital photomicrographs were taken during the cruise to document features described in the thin sections.

Geochemistry

Sampling and analysis of igneous rocks

Sample preparation

Representative samples of igneous rocks were analyzed for major and trace element concentrations during Expedition 324 using inductively coupled plasma–atomic emission spectroscopy (ICP-AES). Samples ranging in size from ~3 cm^3 for cryptocrystalline to very fine grained rocks to as much as 10 cm^3 for medium-grained rocks were cut from the core with a diamond saw blade. If possible, a thin section billet was taken from the same or adjacent interval. All outer surfaces were ground on a diamond-impregnated disk to remove altered rinds and surface contamination from the drill and saw. Each sample was then placed in a beaker containing trace metal–grade methanol and washed ultrasonically for 15 min. The methanol was decanted and the samples were washed in deionized water for 10 min in an ultrasonic bath. They were then washed for 10 min in Barnstead deionized water (~18 MΩ·cm), again in an ultrasonic bath. The cleaned pieces were dried for 10–12 h at 110°C.

The cleaned, dried samples were crushed to <1 cm chips between two disks of Delrin plastic in a hydraulic press. The chips were then ground to a fine powder in tungsten carbide in a SPEX 8000M mixer/mill or, for larger samples, a SPEX 8515 Shatterbox; the smallest samples were hand-ground in an agate mortar. It should be noted that among the elements analyzed, contamination from the tungsten carbide mills is negligible (Shipboard Scientific Party, 2003b). Some samples were amygdular and, before grinding, we hand-picked chips under a binocular microscope in order to obtain material that was as free of amygdules as possible. Hand-picking was also done for several clasts separated from the volcaniclastic rocks of Site U1348. After grinding, a 1000.0 ± 0.5 mg aliquant of the sample powder was weighed on a Mettler Toledo dual balance system and ignited to determine weight loss on ignition (LOI). Samples from Sites U1346–U1349 were ignited at 975°C for 4 h. Normally, a temperature >1000°C is achieved for LOI measurements, but the maximum temperature that the muffle furnace on the ship could reach during most of Expedition 324 was 975°C. For the Site U1350 samples, a temperature of 1025°C was attained, following addition of a step-up transformer to the furnace (see below). Estimated uncertainty on LOI values is ~0.2 mg (0.02 wt%).

ODP *Technical Note* 29 (Murray et al., 2000) describes in detail the shipboard procedure for digestion of rocks and ICP-AES analysis of samples. The following protocol is an abbreviated form of this procedure with minor modifications. After determination of LOI, 100.0 ± 0.2 mg aliquots of the ignited whole-rock powders were weighed and mixed with 400.0 ± 0.5 mg of $LiBO_2$ flux that had been preweighed on shore. Standard rock powders and full procedural blanks were included with unknowns in each ICP-AES run. All samples and standards were weighed on the Cahn C-31 microbalance (designed to measure on board) with weighing errors estimated to be ±0.05 mg under relatively smooth sea-surface conditions.

Ten milliliters of 0.172 mM aqueous LiBr solution was added to the mixture of flux and rock powder as a nonwetting agent to prevent the cooled bead from sticking to the crucible. Samples from Sites U1346–U1349 were then fused individually in Pt-Au (95:5) crucibles for ~12 min at a maximum temperature of 1050°C in an internal-rotating induction furnace (Bead Sampler NT-2100). Because of a breakdown of this instrument late in the cruise, the Site U1350 samples were fused in the muffle furnace. Addition of a step-up transformer allowed the muffle furnace to reach a temperature of 1025°C. The furnace was heated to 900°C, 6–12 samples were inserted together, and the furnace temperature was increased as rapidly as possible to 1025°C. After 5 min at 1025°C, the samples were removed; the total time in the furnace at temperatures above 900°C was ~30 min.

After cooling, beads were transferred to high-density polyethylene (HDPE) bottles and dissolved in 50 mL of 10% (by volume) HNO_3; dissolution was aided by shaking with a Burrell wrist-action bottle shaker for 1 h. Following digestion of the bead, the solution was passed through a 0.45 µm filter into a clean 60 mL wide-mouth HDPE bottle. Next, 2.5 mL of this solution was transferred to a plastic vial and diluted with 17.5 mL of 10% HNO_3 to bring the total volume to 20 mL. The final solution-to-sample dilution factor was ~4000. For standards, stock standard solutions were placed in an ultrasonic bath for 1 h prior to final dilution to ensure a homogeneous solution.

Analyses

Major (Si, Ti, Al, Fe, Mn, Mg, Ca, Na, K, and P) and trace (Ba, Sr, Zr, Y, V, Sc, Cu, Zn, Co, Cr, and Ni) element concentrations of standards and samples were determined with a Teledyne Leeman Labs Prodigy ICP-AES instrument. Wavelengths used for sample analysis during Expedition 324 are provided in Table T5. For several elements, measurements were made at two wavelengths (e.g., Si at 251.611 and 288.158 nm).

The plasma was ignited at least 30 min before each run of samples to allow the instrument to warm up and stabilize. A zero-order search was then performed to check the mechanical zero of the diffraction grating. After the zero-order search, the mechanical step positions of emission lines were tuned by automatically searching with a 0.002 nm window across each emission peak using basalt laboratory standards BAS-140 (Bach et al., 1996) or BAS-206 (Shipboard Scientific Party, 2003b) in 10% HNO_3. During the initial setup, BAS-140 was used to select an emission profile for each peak to determine peak-to-background intensities and set the locations of background levels for each element. The Prodigy software uses these background locations to calculate the net intensity for each emission line. Photomultiplier voltage was optimized by automatically adjusting the gain for each element using BAS-140.

The ICP-AES data presented in the "Geochemistry" sections of the site chapters were acquired using the Gaussian mode of the Prodigy software. This mode fits a curve to points across a peak and integrates the area under the curve for each element measured. Each sample was analyzed three times from the same dilute solution (i.e., in triplicate) within a given sample run. For elements measured at two wavelengths, we either used the wavelength giving the better calibration line in a given run or, if the calibration lines for both wavelengths were of similar quality, used the data for both and reported the average concentration.

A typical ICP-AES run (Table T6) included

- A set of 9 certified rock standards (BCR-2, BHVO-2, BIR-1, JA-3, JGb-1, JR-2, NBS-1c, SCO-1, and STM-1), analyzed at the beginning of each run;
- As many as 23 samples (unknowns) analyzed in triplicate;
- A drift-correcting standard (BHVO-2) analyzed in every fifth sample position and at the beginning and end of each run;
- Blank solutions, analyzed near the beginning and end of each run and, in the longer runs, at another point in the middle of the sequence; and
- Two "check" standards (BAS-140 and BAS-206) run as unknowns, each analyzed in triplicate at least twice during a run.

A 10% HNO_3 wash solution was run for 90 s between each analysis.

Data reduction

Following each run of the instrument, the measured raw-intensity values were transferred to a data file, corrected for instrument drift, and then corrected for the procedural blank. Drift correction was applied to each element by linear interpolation between the drift-monitoring solutions run every fifth analysis. After drift correction and blank subtraction, a calibration line for each element was calculated using the results for the certified rock standards. Element concentrations in the samples were then calculated from the relevant calibration lines.

Replicate analyses of the basalt "check" standards BAS-140 and BAS-206 were used to estimate precision and provide an idea of accuracy for both major and trace elements. Table T7 summarizes the results and compares them with published data. For most elements, the Expedition 324 averages agree well with previously published values. However, our values for Cr in BAS-206 are considerably and consistently higher (135 ± 10 versus 83.7 ppm). At present, we have no explanation for this discrepancy, but we note that our Cr values for BAS-140 agree within error with published values (191 ± 9.7 and 186 ppm, respectively).

Individual analyses of both check standards and samples produced total major element weight percentages that vary from 100 wt% by as much as several percent. Probable causes include errors in weighing the sample (particularly in rougher seas) and/or flux powders and the relatively low temperature of ignition for most of the samples. To facilitate comparison of the Expedition 324 results with each other and with data from the literature, we normalized the measured major element values to 100 wt% totals.

Sedimentary carbon and carbonate analysis

Sediment and sedimentary rock samples were scraped to remove surface contamination, then freeze-dried to remove water and powdered to ensure complete homogenization. Carbonate content was determined by acidifying ~10 mg of bulk powder with 2 M HCl and measuring the CO_2 evolved. A UIC coulometer was employed for the measurement.

We determined total carbon content for the same samples by combustion of the sample at an initial temperature of 900°C in a Thermo Electron Corporation CHNS analyzer (Flash EA 1112 Series). The total carbon value was then used to calculate weight percent of total organic carbon by subtraction (i.e., the weight percent of carbon in the carbonate measured by coulometric analysis was subtracted from the total carbon content obtained with the CHNS analyzer).

Physical properties

Shipboard measurements of physical properties were performed to provide preliminary information characterizing the recovered material. The primary objective of Expedition 324 was to recover hard rock, which necessitated a modified approach compared with expeditions focusing on sedimentary coring. Sedimentary material was recovered, but it was disturbed by the exclusive use of RCB drilling except for most volcaniclastic sediments, which are relatively consolidated. The descriptions herein relate specifically to hard rock material. Sedimentary material was treated in the same manner despite more limited discrete sampling.

Once recovered, whole-round cores were first allowed to thermally equilibrate to ambient room temperature (3 h for hard rock, 4 h for sedimentary material). Core sections with continuous intervals longer than 8 cm were run through the WRMSL for measurement of GRA density and magnetic susceptibility. Magnetic susceptibility and GRA data from gaps and cracks between pieces were filtered out of the data sets using a MATLAB routine (written by A. Harris during Expedition 324) as described below in **"Data filtering."** The filtered data were then visually double-checked against images of the core section halves. Sections longer than 50 cm were measured with the NGRL. The WRMSL also incorporates a compressional wave velocity sensor (PWL) and a noncontact resistivity detector (NCR). The PWL was used only in a few rare cases where sedimentary sections filled most of the core liner; even then sufficient contact with the rock could not always be made. The NCR was not employed during this cruise because of the same unfilled core liner problem, which is common in hard rock recovery.

After measurements with the WRMSL and NGRL, the cores were split into archive and working halves. The archive half of the core was passed through the SHMSL for measurement of point magnetic susceptibility and color reflectance. The SHMSL also uses a laser to record piece heights, which yields information about the location of gaps and cracks between pieces of the core. This information was used to aid data filtering of whole-round and split-half measurements (see **"Data filtering"**).

Thermal conductivity was measured on either the archive or working half of the split cores, depending on availability of suitable material. The thermal conductivity sensors experienced technical difficulties at the end of Hole U1349A; therefore, there are no measurements for Hole U1350A.

Lastly, discrete samples were taken from the working half at intervals of ~1–2 per core. Discrete samples were used for compressional wave velocity measurements in three directions and moisture and density (MAD) measurements including bulk density, dry density, grain density, water content, void ratio, and porosity. A comprehensive discussion of methodologies and calculations used in the R/V *JOIDES Resolution* physical properties laboratory is presented in Blum (1997).

Whole-Round Multisensor Logger measurements

GRA bulk density and magnetic susceptibility were measured nondestructively with the WRMSL. To optimize WRMSL performance, sampling intervals and measurement integration times were the same for all sensors. Sampling intervals were set at 2 cm with an integration time of 5 s for each measurement. These sampling intervals are common denominators of the distances between the sensors installed on the WRMSL (30–50 cm) and allow sequential and simultaneous measurements. Quality assurance/Quality control (QA/QC) was monitored by passing a single core liner filled with fresh water through the WRSML after every core.

The primary objective of Expedition 324 was the recovery of hard rock. In general, measurements are most effective with a completely filled core liner with minimal drilling disturbance. Consequently, the diameter of the core liner (66 mm) is assumed for the core diameter, even though the liner is often <100% filled. In addition, hard rocks are often recovered in pieces, rather than continuous core, which compounds the diameter discrepancy that is already introduced by the drilling process. Therefore, GRA bulk density and magnetic susceptibility measurements tend to underestimate true values. Data were filtered to remove anomalously low values associated with gaps and cracks in the core (see **"Data filtering"**).

Gamma ray attenuation bulk density

The GRA densiometer on the WRMSL operates by passing gamma rays from a ^{137}Cs source through a whole-round core into a 75 mm × 75 mm sodium iodide detector situated directly below the core. The gamma ray peak has a principal energy of 0.662 MeV and is attenuated as it passes through the core. The attenuation of gamma rays, mainly by Compton scattering, is related to the material bulk density. Therefore, for a known thickness of sample the gamma ray count is proportional to density. Calibration of the GRA densiometer was performed using core liners filled with seawater and aluminum density standards. Recalibration was performed as needed if the freshwater QA/QC standard after every core deviated significantly (more than a few percent) from 1 g/cm^3. The spatial resolution of the GRA densitometer is <1 cm.

Magnetic susceptibility

Magnetic susceptibility, k, is a dimensionless measure of the degree to which a material can be magnetized by an external magnetic field:

$$k = M/H,$$

where M is the magnetization induced in the material by an external field strength H. Magnetic susceptibility responds to variations in the type and concentration of magnetic grains, making it useful for the identification of compositional variations. Materials such as clay (e.g., from the alteration of igneous materials) have a magnetic susceptibility several orders of magnitude lower than magnetite and other iron oxides that are common constituents of igneous material. Water and plastics (core liner) have a slightly negative magnetic susceptibility.

The WRMSL incorporates a Bartington Instruments MS2 meter coupled to a MS2C sensor coil with a diameter of 8.8 cm and operates at a frequency of 565 Hz. The sensor output can be set to centimeter-gram-second (cgs) units or SI units, with the IODP standard being the SI setting. The core diameter is smaller than the aperture through which it passes to be measured. Therefore, a volume correction factor must be applied to the data offline. Assuming a core diameter of 66 mm and using the coil aperture of 88 mm, the correction factor simply entailed multiplying the $\times 10^{-5}$ SI units by a factor of 0.68 (Blum, 1997).

The MS2C coil is calibrated with a homogeneous mixture of magnetite and epoxy in a 40 cm long piece of core liner to an accuracy of ±5% (factory preset). The resolution of the method is ±4 cm; therefore, core material that is not continuous over an 8 cm interval will underestimate magnetic susceptibility. Data collected near gaps or pieces smaller than 8 cm were removed by a filter (see **"Data filtering"**) and shown as grayed out points in report figures.

Natural Gamma Radiation Logger

The Natural Gamma Radiation Logger (NGRL) installed on the *JOIDES Resolution* was designed and built at IODP-Texas A&M University (TAMU) from 2006 to 2008. NGR occurs primarily as a result of the decay of ^{238}U, ^{232}Th, and ^{40}K isotopes. Data generated from this instrument are used to augment geologic interpretations.

The main NGR detector unit consists of 8 NaI scintillator detectors, 7 plastic scintillator detectors, 22 photomultipliers, and passive lead shielding. The NaI detectors are covered by 8 cm of lead shielding. In addition, lead separators (~7 cm of low-background lead) are positioned between the NaI detectors. Half of the lead shielding closest to the NaI detectors is composed of low-background lead, whereas the outer half is composed of regular (virgin) lead. In addition to passive lead shielding, the NGR detector unit employs a plastic scintillator to suppress the high-energy gamma and muon components of cosmic radiation by producing a veto signal when these charged particles pass through the plastic scintillators. The NGR detector unit was calibrated using ^{137}Cs and ^{60}Co sources and identifying the peaks at 662 and 1330 keV, respectively. Calibration materials were from Eckert & Ziegler Isotope Products, Valencia, California (USA).

For presentation purposes, the counts were summed over the range of 100–3000 keV to be comparable with data collection from previous cruises and for direct comparison with downhole logging data. Background measurements of an empty core liner counted for 20,000 s (5 h) were made upon arrival at each site. Over the 100–3000 keV integration range, background counts averaged 4–5 cps and contributed <0.5% to the overall signal of the measured core.

A single measurement run consisted of two eight-measurement sets (20 cm between each of the eight sensors). The first set was measured at one position and the second set was measured at a another position shifted 10 cm from the first (for a total of 16 measurements, each 10 cm apart, over a 150 cm long section of core). The quality of the energy spectrum measured in a core depends on the concentration of radionuclides in the sample but also on the counting time, with higher times yielding a more clearly defined spectra. The available count time in each position depended on how fast and how much core was recovered. In general, we had the opportunity to count for longer times, yielding statistically significant energy spectra because the rate of hard rock core recovery from drilling averaged 1 core every 2–3 h. Count times ranged between 1800 and 5400 s for each position, resulting in total count times of 1–3 h per section. Improved spectral resolution allows qualitative identification of the main contributors to the energy spectra (i.e., products of the ^{40}K, ^{232}Th, or ^{238}U decay chains). Building a database of well-resolved spectra works toward the aim of separation of ^{40}K, ^{232}Th, and ^{238}U contributions and eventual quantification of concentrations of the radionuclide daughters.

Section Half Multisensor Logger measurements

The SHMSL measures spectral reflectance and magnetic susceptibility on core section halves. The archive half of the split core is placed on the core track. An electronic platform moves along a track above the core section, recording the sample height using a laser sensor. The laser establishes the location of the bottom of the section, then the platform reverses the direction of movement, moving from bottom to top making measurements of point magnetic susceptibility and spectral reflectance data at 2 cm intervals.

Color reflectance spectrometry

Reflectance is measured from 171 to 1100 nm wavelength at 2 nm intervals using a halogen light source, covering a wavelength from ultraviolet through visible to near infared. The scan of the entire wavelength range takes ~5 s per data acquisition offset. The data are generated using the L*a*b color system, in which L* is luminescence, a* is the blue + green values, and b* is the red + green values. The color reflectance spectrometer calibrates on two spectra, pure white (reference) and pure black (dark). Color calibration was conducted approximately every 12 h.

Point magnetic susceptibility

The point magnetic susceptibility is measured using a contact probe with a flat 15 mm diameter sensor operating at a frequency of 0.580 kHz. The sensor takes and averages three measurements at 0.1 attenuation for each offset to an accuracy of 5%. The spatial resolution of the magnetic susceptibility point instrument is 20 mm, making it advantageous over whole-round magnetic susceptibility for cores consisting of broken pieces <8 cm (the spatial resolution of whole-round magnetic susceptibility). Units are reported in dimensionless SI units on a volume basis. The point magnetic susceptibility meter was calibrated by the manufacturer before installation on the ship. The probe is zeroed in air before each measurement point, and a background magnetic field is measured (influence from metal track, etc.) and removed from the data before being output. The instrument is calibrated so that the value output is measured assuming the probe is buried in the sample; however, because the probe is only in contact with the upper, flat surface, a correction factor of 2× was applied after the data were collected (note that the data stored in LIMS have not had this correction applied).

Thermal conductivity

Thermal conductivity is the rate at which heat flows through a material and is dependent on composition, porosity, and structure. Thermal conductivity was measured by transient heating on the archive half of split core with a known heating power and a known geometry. The changes in temperature with time after an initial heating were recorded using a TK04 system. The temperature of the superconductive probe has a linear relationship with the natural logarithm of the time after the initiation of heat (Blum, 1997).

Thermal conductivity was measured on the archive half of the split core with the probe in half-space mode (Vacquier, 1985). These half-space determinations were made with a needle probe embedded in the surface of an epoxy block with a low thermal conductivity (Vacquier, 1985). Samples need to be smooth to ensure adequate contact with the heating needle. Visible saw marks were removed when necessary by grinding and polishing the split face using 120–320 gauge silicon carbide powder (most samples did not require polishing). Because measurements were sometimes performed on the archive half of the core, we avoided the use of silicon gel, which can be employed to improve sample/needle contact.

Samples equilibrated to room temperature in a seawater vacuum saturator for 4 h, and sample and sensor needle were equilibrated together in a cooler insulated with styrofoam for at least 15 min prior to measurement. Isolation of the sample and sensor needle eliminated the effect of rapid but small temperature changes introduced by air currents in the laboratory. The instrument internally measures drift and does not begin a heating run until sufficient thermal equilibrium is attained. Cores were measured at irregular intervals (one sample per section) depending on the availability of homogeneous and relatively vein/crack-free pieces long enough to be measured without edge effects (pieces at least 7 cm long; i.e., longer than the instrument needle). Measurements were made at room temperature and pressure, and were not corrected for in situ conditions.

A MACOR ceramic standard with a certified thermal conductivity of 1.637 ± 0.033 W/(m·K) was run at each site, and the results are summarized in Table T8. Unfortunately, the puck and embedded sensor needle experienced irrevocable technical difficulties at the end of Hole U1349A, and as a result thermal conductivity measurements were not conducted on samples from Hole U1350A.

Discrete samples

Cubic samples were cut from the working halves of split cores at an interval of ~1–2 samples per core. Collection of these ~7 cm^3 samples aimed to best represent the general variation and lithologies of the core. The purpose of these samples is two-fold. First, they are used for physical property measurements of compressional wave velocity and MAD measurements (explained below). Second, discrete samples were shared with paleomagnetists to minimize core depletion.

Moisture and density

Several basic rock quantities of interest (water content, bulk density, dry density, porosity, and void ratio) are found most accurately through mass and volume determinations on discrete samples. MAD data are also used for comparison with GRA bulk density data from the WRMSL. The shipboard MAD facility for hard rock coring on the *JOIDES Resolution* consists of a vacuum water saturator, a dual balance system, and a hexapycnometer.

Vacuum water saturator

Determination of a precise and accurate wet mass of sparsely porous material requires that the pore space of the sample be completely saturated. To maintain this saturation, we used a vacuum pump system. The system consisted of a plastic chamber filled with seawater into which the samples were placed. A vacuum pump then removes air from the chamber, essentially forcing seawater into the sample pore spaces. The samples are kept under vacuum for at least 24 h. During this time, the vacuum is checked at 2–3 h intervals to ensure a stable underpressure. After removal from the saturator, the cubes are stored in sample containers filled with seawater to help prevent evaporation of pore water. Next, the cube surfaces are lightly patted with a paper towel to remove water clinging to outer surfaces and wet mass is immediately determined using the dual balance system.

Dual balance system

The dual balance system was used to measure both wet and dry masses. The two analytical balances (Mettler-Toledo XS204) compensate for ship motion; one acts as a reference and the other measures the unknown (sample). A standard weight of similar value to the sample was placed upon the reference balance to increase accuracy. The default setting of the balances is 300 measurements (taking ~1.5 min to measure). However, when in transit we found that a greater number of measurements (400–1000), and therefore a longer measurement time (depending on sea state), were required. On site, however, averages of 300 measurements were indistinguishable from averages of 500 measurements. We investigated the effect that matching the reference and sample weight had by repeatedly measuring a basaltic minicore sample with different reference masses. Overall, for this test sample an error of as much as 0.3% could be introduced if the samples were mismatched with their reference weight by as much as 50%. With reference weight matching to within ~10%, precision of 0.005 g was readily attainable. Precisions were recorded on the hard copies of data log sheets, which are stored at TAMU.

Hexapycnometer system

The hexapycnometer system measures dry sample volume using pressurized helium-filled chambers. At the start of the expedition, and whenever the helium gas tank was changed, shipboard technicians performed a calibration using stainless steel spheres of known volume. A batch of samples consisted of four cells with unknowns and one cell with two stainless steel spheres (3 and 7 cm^3). The spheres were cycled through the cells to identify any systematic error and/or instrument drift. Spheres are assumed to be known within 1% of their total volume. Individual volume measurements were preceded by three purges of the sample chambers with research grade (99.995% or better) helium heated to 280°C, followed by three data acquisition cycles.

Moisture and density calculations

Measurement of wet mass and dry mass by the dual balance system along with a dry volume measured by the hexapycnometer allows for the determination of a number of MAD properties. During this expedition, we employed MAD method “C.” Method “D,” where wet mass is determined by caliper rather than saturation, is only appropriate for samples that are too vesicular to adequately saturate.

The MAD method C program uses physical measurement data (dry mass, wet mass, and dry volume) to calculate the quantities of interest shown in Table T9. For more details on physical property MAD methods, see Blum (1997).

Compressional wave velocity

Compressional wave (*P*-wave) velocity measurements of hard rock samples were performed on the same discrete cube samples that were used for MAD and paleomagnetism determinations. *P*-wave measurements were performed on seawater-saturated samples directly after wet mass determinations were made. Measurements used the *x*-axis caliper-type contact probe transducers on the *P*-wave velocity gantry. Oriented samples were rotated manually to measure *y*- and *z*-axis velocities with the same instrument. The system uses Panametrics-NDT Microscan delay line transducers, which transmit at 0.5 MHz. To maximize contact with the transducers, deionized water was applied to sample surfaces.

The signal received through the sample was recorded by the computer attached to the system, and the peak (*P*-wave arrival) was chosen with autopicking software. The complete waveform is stored with the data if reanalysis is deemed necessary; however, shipboard visual checks of the picks appeared satisfactory. The distance between transducers was measured with a built-in linear voltage displacement transformer (LDVT).

Calibration was performed each day before measurements were made with a series of acrylic cylinders of differing thicknesses and a known *P*-wave velocity of 2750 ± 20 m/s. The determined system time delay from calibration was subtracted from the picked arrival time to give a traveltime of the *P*-wave through the sample. The thickness of the sample (calculated by LDVT in meters) was divided by the traveltime (in seconds) to calculate *P*-wave velocity in meters per second.

Data filtering

Gaps and cracks in the core can cause anomalously low readings of magnetic susceptibility and bulk density. Reflectance and color readings for gaps and cracks are not relevant to this study. Including meaningless data from gaps can hinder interpretation, especially of actual low readings of magnetic susceptibility and bulk density. Therefore, these data (magnetic susceptibility, GRA density, L*, b*, and magnetic susceptibility point) were filtered using height measurements, which were collected with the laser attached to the SHMSL. Laser heights were used to identify cracks between pieces and gaps where plastic spacers were inserted. Data corresponding to locations of gaps and cracks, as well as data near the edges of pieces, were then removed from each data set (often plotted as gray points on color plots).

Filtering program details

A series of parameters (including gradient threshold, minimum detectable gap width, minimum piece length, and instrumentation edge effect) were used to filter data. Whereas the user of the filter has some flexibility in choosing parameters, most are predetermined by the resolution and specifications of the instrumentation.

To determine the edges of pieces, the gradient of the laser height was calculated. The relatively flat surfaces of continuous section-half pieces have a small gradient. However, the sharp contrast between piece height and the height of an empty core liner results in a large gradient. Using this relationship, a threshold parameter for the gradient was set (±5 mm/cm) and used to determine the locations of piece edges. The lateral resolution of laser height measurements was 0.2 cm. With the gradient threshold set at ±5 mm/cm, this means any change in height >1 cm between subsequent measurements would indicate a piece edge or gap/crack. This threshold is set so that data for pieces with heights ranging from 1 to 3.3 cm (a full section-half radius) are kept and data for pieces with heights shorter than 1 cm are removed by the filter. Data associated with <1 cm pieces are likely to be underestimated, similar to data associated with cracks/gaps.

The minimum detectable gap width is directly related to the lateral resolution of the laser height measurements. Gaps <0.2 cm (the lateral resolution of the laser measurements) are undetectable, unless, by chance, a measurement lands within the small gap. The minimum detectable gap width could be decreased by increasing lateral resolution of the laser measurements, but this is likely unnecessary because cracks <0.2 cm should have a small effect on measured data.

The length of the "zone of influence" (the amount of core material that influences data readings) is determined by individual instrument specifications, which in turn determines both the minimum piece length and instrumentation edge effect parameters. The minimum piece length is exactly equal to the length of the zone of influence (assuming a full core liner). The edge effect parameter is the distance away from a gap or crack a measurement must be to be unaffected by the empty space. The edge effect parameter is exactly equal to half of the length of the minimum piece length. A list of the minimum piece length and edge effect parameters for each instrument is listed in Table T10.

Data points that were filtered out still appear in physical property plots and figures (e.g., VCDs) as grayed out points, whereas data that passed these sets of criteria described above are plotted with colored points according to the legend/key. For example, GRA bulk density measurements that were at least 1 cm away (edge effect parameter) from a 0.2 cm or larger crack (minimum detectable gap) and that were measured on pieces that were at least 2 cm long (minimum piece length) pass through the filter. For magnetic susceptibility and magnetic susceptibility point data, correction factors of 0.68× and 2× were applied to LIMS output data, respectively (even for grayed out points), because these corrections are due to instrumentation design and measurement technique and not related to the filtering process.

The major benefit of filtering data from GRA density and magnetic susceptibility measurements is that actual lows can be discerned from data trends. However, caution should be used, as this is the first attempt at choosing appropriate parameters and we have tried to err on the side of allowing more data through the filter than not. Data that are filtered out are underestimates of real values. Where the lowest values are often the target of the filtering, even high values may be filtered out if they are near gaps in material. In reality, these high values should be even higher given a continuous piece of core.

In the future, the potential exists for the laser heights to be used for a volume correction instead of merely a filter. Then trends may be easier to discern from the physical property data and may more closely correspond with other, independent data sets (e.g., logging bulk density). The NGR whole-round data were not filtered because of already low sample densities.

Paleomagnetism

During Expedition 324, we conducted routine demagnetization measurements of discrete samples from working-half sections. At each site, a set of samples was treated by alternating-field (AF) demagnetization and another set was treated by thermal demagnetization. We also measured bulk magnetic susceptibility on discrete samples after each temperature step during thermal demagnetization to determine whether the carrier of characteristic remanent magnetization (ChRM) of a sample remains intact or undergoes any alteration caused by the repeated heating steps.

Magnetometer

Usual shipboard paleomagnetic measurements are carried out with the automated pass-through cryogenic magnetometer with a direct-current superconducting quantum interference device (2G Enterprises model 760-R) in order to demagnetize and measure remanent magnetization. The magnetometer is equipped with an inline AF demagnetizer (2G Enterprises model 2G600) capable of producing peak fields of 80 mT with 200 Hz frequency. The magnetometer is run and data are acquired by a program called Remanent Magnetism Determination (SRM version 3.23) written by D. Hornbacher (IODP-TAMU) in LabView (version 8.5) programming language.

However, during transit to the first site, preliminary measurements allowed us to detect some problems in the AF demagnetizing by the 2G magnetometer. We found that samples would behave as if they were acquiring an anhysteretic remanent magnetization (ARM) in the course of the AF demagnetization when the demagnetizing field was larger than ~20 mT (Fig. **F18**). This ARM causes a bias of the measured paleomagnetic inclination, which is critical to our study. Unfortunately, the critical threshold above which ARM was detected varied for each sample. Moreover, the AF fields required to demagnetize basalt samples are usually much higher than 20 mT. After numerous pilot tests using half-cores and discrete samples, we communicated to 2G and concluded that the aging degausser coil may be malfunctioning. However, the 2G magnetometer was used to measure weak magnetization samples (such as some volcaniclastic samples).

As a result, the magnetization measurements were usually carried out with a Molspin Minispin magnetometer. This magnetometer is a slow-speed spinner fluxgate device in which the samples are spun at 6 Hz about a vertical axis in a fluxgate surrounded by a mu-metal shield. To obtain the three components of the magnetization vector, it is necessary to perform a sequence of measurements with the specimen in four orientations.

Core orientation

The standard IODP paleomagnetic coordinate system was used. In this system, +*x* is perpendicular to the split core surface and into the working half, +*z* is downcore, and +*y* is orthogonal to *x* and *z* in a right-hand sense (i.e., it points left along the split-core surface when looking upcore at the archive half) (see **"Structural geology"**).

Magnetic overprints

Several types of secondary magnetization were acquired during coring, which sometimes hampered interpretation. The most common secondary magnetization was a steep downward-pointing overprint attributed to the rotating drill string. This was also seen as a bias for 0° declinations in archive-half sections, which has been observed during many previous cruises (e.g., Leg 206, Shipboard Science Party, 2003a) and has been interpreted as a radially inward overprint.

Working-half (discrete sample) measurement

During the expedition, oriented discrete samples representative of the lithology were taken from the working halves of selected sections. Cubic samples with a volume of ~7 cm^3 were collected (typically one or two per section) for shipboard magnetic analysis. We drew an arrow on the split-core face pointing uphole (*z*-axis) and used the rock saw to cut the sample. The same samples were also used for physical property measurements. We carried out AF demagnetizations on approximately one-third to one-half of the samples and thermal demagnetizations on the remaining samples.

Susceptibility measurements

In addition to standard paleomagnetic measurements, bulk magnetic susceptibilities were determined for all the discrete samples using the Kappabridge KLY 4S (Geofyzika Brno). Values have been corrected for the true cubic sample volume. Bulk magnetic susceptibilities were also measured after each heating step in order to track possible magnetomineralogical changes that could happen because of the repeated heating.

Thermal demagnetizations

Discrete samples from the working-half sections were progressively demagnetized using a Schonstedt Thermal Demagnetizer (model TSD-1) in steps of 50° or 25°C for the higher temperature steps, up to a temperature usually between 500° and 600°C. The temperature steps were adjusted as a function of the unblocking temperature spectra of each batch of samples. Each batch consisted of an ensemble of 6–12 individual samples. After each demagnetization step, samples were cooled in a low–magnetic field environment and the remaining magnetic intensity and orientation were measured with the Molspin Minispin magnetometer (or the 2G magnetometer for weak samples).

For a few samples, the thermal demagnetization procedure was preceded by AF demagnetization at 10 mT to partly remove the drilling overprint, with the hope that it would remove the viscous component before the thermal procedure and increase the success rate of thermal demagnetizations. Because this was usually not the case, this procedure was not used routinely.

Alternating-field demagnetizations

As we could not use the 2G magnetometer to perform AF demagnetizations, we used the D-Tech demagnetizer. Samples were demagnetized in three orthogonal directions by the application of an alternating field with a decay rate of 0.01 mT per half-cycle. The maximum field intensity was 150 mT. Demagnetizations were carried out in field steps of 2 or 3 mT up to 15 mT, then 5 mT up to 30 mT, then 10 or 20 mT up to 80–150 mT, depending on the coercivity spectrum of each sample. The remaining magnetization was measured after each demagnetization step with the Molspin Minispin magnetometer (or the 2G magnetometer for weak samples).

Data analysis

During Expedition 324, ChRM was estimated by principal component analysis (PCA) (Kirschvink, 1980) of three or more of the stable endpoint directions. PCA analysis was conducted using the Progress08 program written by H. Shibuya. The quality of the fit is quantified with the maximum angular deviation, which measures how consistently the demagnetization data fit a line. This parameter is routinely used as a quality index for the calculated ChRM. Maximum angular deviation values >8° were typically considered to signify an ill-defined mean direction, and therefore such samples were rejected from further analysis.

Downhole logging

Downhole logs are used to determine physical, chemical, and structural properties of the formation penetrated by a borehole. The data are rapidly collected, continuous with depth, and measured in situ; they can be interpreted in terms of the stratigraphy, lithology, mineralogy, and geochemical composition of the penetrated formation. Where core recovery is incomplete or disturbed, log data may provide the only way to characterize the borehole section; where core recovery is good, log and core data complement one another and may be interpreted jointly.

Downhole logs are sensitive to formation properties on a scale that is intermediate between those obtained from laboratory measurements on core samples and geophysical surveys. They are useful in calibrating the interpretation of geophysical survey data (e.g., through the use of synthetic seismograms) and provide a necessary link for the integrated understanding of physical properties on all scales.

Wireline logging

During wireline logging, the logs were made with a variety of Schlumberger logging tools combined into several tool strings, which were run down the hole after coring operations were completed. Three wireline tool strings were used during Expedition 324 (Fig. F19; Table T11): the triple combination (gamma ray, density, porosity, and electrical resistivity), the FMS-sonic (gamma ray, microresistivity image of the borehole wall, and compressional- and shear-wave velocities), and the Ultrasonic Borehole Imager (UBI; transit times, amplitudes, and borehole radii). Each tool string also contained a telemetry cartridge for communicating through the wireline to the Schlumberger data acquisition system on the drillship.

In preparation for logging, the boreholes were flushed of debris by circulating viscous drilling fluid through the drill pipe to the bottom of the hole. Depending on hole conditions, the viscous drilling fluids used during Expedition 324 were either attapulgite mixed with seawater (approximate weight = 8.9 ppg or 1.07 g/cm^3) or drilling mud containing barite mixed with seawater (approximate weight = 10.5 ppg or 1.26 g/cm^3). The drill bit was released (using the mechanical bit release) and the bottom-hole assembly was pulled up. The tool strings were then lowered downhole by a seven-conductor wireline cable during sequential runs. A new wireline heave compensator was employed to minimize the effect of ship's heave on the tool position in the borehole (see below). During each logging run, incoming data were recorded and monitored in real time on the MCM MAXIS logging computer. The tool strings were then pulled up at constant speed, typically 250–550 m/h, to provide continuous measurements as a function of depth of several properties simultaneously.

Logged sediment properties and tool measurement principles

The logged properties and the methods that the tools use to measure them are briefly described below. The main logs taken by the tools are listed in Table T12. More detailed information on individual tools and their geological applications may be found in Ellis and Singer (2007), Goldberg (1997), Lovell et al. (1998), Rider (1996), Robinson et al. (2008), Schlumberger (1989, 1994), and Serra (1984, 1986, 1989).

Natural radioactivity

The Hostile Environment Gamma Ray Sonde (HNGS) uses two bismuth germanate scintillation detectors and five-window spectroscopy to determine concentrations of ^{40}K, ^{232}Th, and ^{238}U. The isotopes of these three elements dominate the natural radiation spectrum. The HNGS filters out gamma ray energies below 500 keV, eliminating sensitivity to bentonite or KCl in the drilling mud and improving measurement accuracy.

Density and photoelectric effect

Formation density was determined with the Hostile Environment Litho-Density Sonde (HLDS). The sonde contains a radioactive cesium (^{137}Cs) gamma ray source (622 keV) and far and near gamma ray detectors mounted on a shielded skid, which is pressed against the borehole wall by a hydraulically activated eccentralizing arm. Gamma rays emitted by the source undergo Compton scattering, which involves the transfer of energy from gamma rays to the electrons in the formation through elastic collision. The number of scattered gamma rays that reach the detectors is directly related to the density of electrons in the formation, which is in turn related to bulk density. Porosity may also be derived from this bulk density if the matrix (grain) density is known.

The HLDS also measures photoelectric absorption as the photoelectric effect (PEF). Photoelectric absorption of the gamma rays occurs when their energy is reduced below 150 keV after being repeatedly scattered by electrons in the formation. Because PEF depends on the atomic number of the elements in the formation, it also varies according to the chemical composition of the minerals present. Good contact between the tool and borehole wall is essential for good HLDS logs; poor contact results in underestimation of density values. The use of drilling mud containing barite can significantly affect the PEF measurements.

Porosity

Formation porosity was measured with the Accelerator Porosity Sonde. The sonde incorporates a minitron neutron generator that produces fast (14.4 MeV) neutrons and five neutron detectors (four epithermal and one thermal) positioned at different distances from the minitron. The tool's detectors count neutrons that arrive at the detectors after being scattered and slowed by collisions with atomic nuclei in the formation. Each of the five detectors provides a special feature to enhance the overall measurement. The near detector is centered in the tool and is used to normalize the count rates for differences in the minitron source. The remaining detectors are eccentered, and neutron backshielding is used to focus them toward the formation to minimize the effect of the borehole environment.

Neutrons leaving the tool travel through the surrounding borehole and formation and interact primarily with hydrogen atoms present in the common formation fluids. Since neutrons and hydrogen atoms have about the same mass, successive collisions rapidly reduce the energy of the neutrons to the thermal energy level of the formation (0.025 eV). Since water contains about the same quantity of hydrogen per unit volume, the detector count-rate ratios can be calibrated in terms of liquid-filled porosity in clean formations. However, because hydrogen bound in minerals such as clays or in hydrocarbons also contributes to the measurement, the raw porosity value is often an overestimate.

A mineral's ability to absorb thermal neutrons is defined as its capture cross section (Σ_f). Formations and formation fluids containing chlorine atoms are the most effective capturers of thermal neutrons. Thus, the rate of thermal neutron decay in the formation can be measured and used to differentiate between hydrocarbons in the pore space and salt water. Sigma is measured in capture units (cu). Higher values of Σ_f equate to a greater ability to capture thermal neutrons.

Electrical resistivity

The phasor dual induction–spherically focused resistivity tool (DITE-SFL) was used to measure electrical resistivity. The DITE-SFL provides three measures of electrical resistivity, each with a different depth of investigation into the formation. The two induction devices (deep and medium depths of penetration) transmit high-frequency alternating currents through transmitter coils, creating magnetic fields that induce secondary currents in the formation. These currents produce a new inductive signal, proportional to the conductivity of the formation, which is measured by the receiving coils. The measured conductivities are then converted to resistivity (in ohm-meters). For the shallow penetration resistivity, the current necessary to maintain a constant drop in voltage across a fixed interval is measured. This is a direct measurement of resistivity. Typically, igneous minerals found in crustal rocks are electrical insulators, whereas sulfide and oxide minerals as well as ionic solutions like pore water are conductors. Electrical resistivity, therefore, can be used to evaluate porosity using Archie's law (Archie, 1942, 1950) and fluid salinity.

Acoustic velocity

The Dipole Sonic Imager (DSI) measures the transit times between sonic transmitters and an array of eight receivers. It combines replicate measurements, thus providing a direct measurement of sound velocity through sediments that is relatively free from the effects of formation damage and an enlarged borehole (Schlumberger, 1989). Along with the monopole transmitters found on most sonic tools, the DSI also has two crossed-dipole transmitters that allow the measurement of orthogonal shear wave velocities in addition to the compressional wave velocity, even in the slow formations typically encountered during IODP expeditions.

Formation MicroScanner

The FMS provides high-resolution electrical resistivity–based images of borehole walls. The tool has 4 orthogonal arms and pads, each containing 16 button electrodes that are pressed against the borehole wall during the recording. The electrodes are arranged in two diagonally offset rows of 8 electrodes each. A focused current is emitted from the button electrodes into the formation, with a return electrode near the top of the tool. Resistivity of the formation at the button electrodes is derived from the intensity of current passing through the button electrodes. Processing transforms these measurements into oriented high-resolution images that reveal the geologic structures of the borehole wall. Further analysis can provide measurements of dip and direction (azimuth) of planar features in the formation.

The development of the FMS tool has added a new dimension to wireline logging (Luthi, 1990; Lovell et al., 1998; Salimullah and Stow, 1992). Features such as bedding, fracturing, slump folding, and bioturbation can be resolved; the fact that the images are oriented means that fabric analysis can be carried out and bed orientations can be measured.

The maximum extension of the caliper arms is 38.1 cm (15 inches). In holes with a diameter larger than 38.1 cm, the pad contact will be inconsistent and the FMS images may appear out of focus and too conductive. Irregular (rough) borehole walls will also adversely affect the images if contact with the wall is poor.

Ultrasonic Borehole Imager

The UBI features a high-resolution transducer that provides acoustic images of the borehole wall. The transducer emits ultrasonic pulses at a frequency of 250 or 500 kHz (low and high resolution, respectively), which are reflected at the borehole wall and then received by the same transducer. The amplitude and traveltime of the reflected signal are determined. A continuous rotation of the transducer and the upward motion of the tool produce a complete map of the borehole wall. The amplitude depends on the reflection coefficient of the borehole fluid/rock interface, the position of the UBI tool in the borehole, the shape of the borehole, and the roughness of the borehole wall. Changes in the borehole wall roughness (e.g., at fractures intersecting the borehole) are responsible for the modulation of the reflected signal; therefore, fractures or other variations in the character of the drilled rocks can be recognized in the amplitude image. The recorded traveltime image gives detailed information about the shape of the borehole, which allows calculation of one caliper value of the borehole from each recorded traveltime. Amplitude and traveltime are recorded together with a reference to magnetic north by means of a General Purpose Inclinometer Tool (GPIT), permitting the orientation of images. If features (e.g., fractures) recognized in the core are observed in the UBI images, orientation of the core is possible. The UBI orientated images can also be used to measure stress in the borehole through identification of borehole breakouts and slip along fault surfaces penetrated by the borehole (i.e., Paillet and Kim, 1987). In an isotropic, linearly elastic rock formation that is subjected to an anisotropic stress field, drilling a subvertical borehole causes breakouts in the direction of the minimum principal horizontal stress (Bell and Gough, 1983).

Borehole inclination and magnetic field measurement

Three-component acceleration and magnetic field measurements were made with the GPIT. The primary purpose of this tool, which incorporates a three-component accelerometer and a three-component magnetometer, is to determine the acceleration and orientation of the FMS-sonic and UBI tool strings during logging. Thus, the FMS and UBI images can be corrected for irregular tool motion caused by the vessel's heave, which allows for more accurate determination of the dip and direction (azimuth) of features.

Log data quality

The principal influence on log data quality is the condition of the borehole wall. If the borehole diameter is variable over short intervals resulting from washouts during drilling or ledges caused by layers of harder material, the logs from those tools that require good contact with the borehole wall (i.e., FMS, density, and porosity tools) may be degraded. Deep investigation measurements such as resistivity and sonic velocity, which do not require contact with the borehole wall, are generally less sensitive to borehole conditions. Very narrow ("bridged") sections also cause irregular log results. The quality of the borehole is improved by minimizing the circulation of drilling fluid while drilling, flushing the borehole to remove debris, and logging as soon as possible after drilling and conditioning are completed.

The quality of the depth determination depends on a series of factors. The depth of the wireline-logged measurement is determined from the length of the logging cable played out at the winch on the ship and a calculation of cable stretch. The seafloor is identified on the natural gamma log by the abrupt reduction in gamma ray count at the water/sediment boundary (mudline). Discrepancies between the drillers depth and the wireline log depth occur because of core expansion, incomplete core recovery, incomplete heave compensation, and drill pipe stretch in the case of drillers depth. In the case of log depth, discrepancies occur because of incomplete heave compensation, incomplete correction for cable stretch, and cable slip. Tidal changes in sea level also have an effect. To minimize the wireline tool motion caused by ship heave, a hydraulic wireline heave compensator adjusts for rig motion during wireline logging operations (Goldberg, 1997).

Logging data flow and log depth scales

Data for each wireline logging run were monitored in real time and recorded using the Schlumberger MAXIS 500 system. The initial logging data are referenced to the rig floor (wireline depth below rig floor [WRF]). After logging was completed, the data were shifted to a seafloor reference (wireline depth below seafloor [WSF]) based on the step in gamma radiation at the sediment/water interface. These data were made available to the science party.

The data were transferred onshore to Lamont-Doherty Earth Observatory, where standardized data processing took place. The main part of the processing is depth matching to remove depth offsets between data from different logging runs, which results in a new depth scale, wireline matched depth below seafloor (WMSF). Also, corrections are made to certain tools and logs, documentation for the logs (with an assessment of log quality) is prepared, and the data are converted to ASCII for the conventional logs and GIF for the FMS images. Schlumberger GeoQuest's GeoFrame software package is used for most of the processing. The data were transferred back to the ship within a few days of logging and made available (in ASCII and DLIS formats) through the shipboard IODP logging database

Measurements such as NGR and density are taken both downhole and on cores. They can be correlated using Correlator software, which allows shifting of the core depths onto the wireline depth.

Core-log-seismic integration

GeoFrame's IESX seismic interpretation software package was used during Expedition 324 to display site survey seismic sections acquired precruise. Velocity and density logs, together with the equivalent measurements made on core in the physical property laboratory, were used to create synthetic seismograms. The depth-traveltime relation was adjusted until the features in the synthetic seismogram matched the features in the seismic section. In this way, lithostratigraphic units in the core are correlated with reflectors and sequences in the seismic section.

References

Ando, A., Nakano, T., Kaiho, K., Kobayashi, T., Kokado, E., and Khim, B.-K., 2009. Onset of seawater ^{87}Sr/^{86}Sr excursion prior to Cenomanian–Turonian Oceanic Anoxic Event 2? New Late Cretaceous strontium isotope curve from the central Pacific Ocean. *J. Foraminiferal Res.,* 39(4):322–334. **doi:10.2113/gsjfr.39.4.322**

Archie, G.E., 1942. The electrical resistivity log as an aid in determining some reservoir characteristics. *J. Pet. Technol.,* 5:1–8.

Archie, G.E., 1950. Introduction to petrophysics of reservoir rocks. *AAPG Bull.,* 34(5):943–961.

Aubele, J.C., Crumpler, L.S., and Elston, W.E., 1988. Vesicle zonation and vertical structure of basalt flows. *J. Volcanol. Geotherm. Res.,* 35(4):349–374. **doi:10.1016/0377-0273(88)90028-5**

Bach, W., Erzinger, J., Alt, J.C., and Teagle, D.A.H., 1996. Chemistry of the lower sheeted dike complex, Hole 504B (Leg 148): influence of magmatic differentiation and hydrothermal alteration. *In* Alt, J.C., Kinoshita, H., Stokking, L.B., and Michael, P.J. (Eds.), *Proc. ODP, Sci. Results,* 148: College Station, TX (Ocean Drilling Program), 39–55. **doi:10.2973/odp.proc.sr.148.114.1996**

Batiza, R., and White, J.D.L., 2000. Submarine lavas and hyaloclastite. *In* Sigurdsson, H., Houghton, B.F., McNutt, S.R., Rymer, H., and Stix, J. (Eds.), *Encyclopedia of Volcanoes:* San Diego (Acad. Press), 361–381.

Bell, J.S., and Gough, D.I., 1983. The use of borehole breakouts in the study of crustal stress. *In* Zoback, M.D., and Haimson, B.C. (Eds.), *Hydraulic Fracturing Stress Measurements:* Washington (Natl. Acad. Press), 201–209.

Bellier, J.-P., and Moullade, M., 2002. Lower Cretaceous planktonic foraminiferal biostratigraphy of the western North Atlantic (ODP Leg 171B), and taxonomic clarification of key index species. *Rev. Micropaleontol.,* 45(1):9–26. **doi:10.1016/S0035-1598(02)80003-4**

Blackman, D.K., Ildefonse, B., John, B.E., Ohara, Y., Miller, D.J., MacLeod, C.J., and the Expedition 304/305 Scientists, 2006. *Proc IODP,* 304/305: College Station, TX (Integrated Ocean Drilling Program Management International, Inc.). **doi:10.2204/iodp.proc.304305.2006**

Blum, P., 1997. Physical properties handbook: a guide to the shipboard measurement of physical properties of deep-sea cores. *ODP Tech. Note,* 26. **doi:10.2973/odp.tn.26.1997**

Bolli, H.M., Beckmann, J.-P., and Saunders, J.B., 1994. *Benthic Foraminiferal Biostratigraphy of the South Caribbean Region:* Cambridge (Cambridge Univ. Press).

Boudagher-Fadel, M.K., Banner, F.T., and Whittaker, J.E., 1997. *The Early Evolutionary History of Planktonic Foraminifers:* London (Chapman and Hall).

Bown, P.R. (Ed.), 1998. *Calcareous Nannofossil Biostratigraphy:* Dordrecht, The Netherlands (Kluwer Academic Publ.).

Bralower, T.J., Fullagar, P.D., Paull, C.K., Dwyer, G.S., and Leckie, R.M., 1997. Mid-Cretaceous strontium-isotope stratigraphy of deep-sea sections. *Geol. Soc. Am. Bull.,* 109(11):1421–1442. **doi:10.1130/0016-7606(1997)109<1421:MCSISO>2.3.CO;2**

Bralower, T.J., Monechi, S., and Thierstein, H.R., 1989. Calcareous nannofossil zonation of the Jurassic–Cretaceous boundary interval and correlation with the geomagnetic polarity timescale. *Mar. Micropaleontol.,* 14(1–3):153–235. **doi:10.1016/0377-8398(89)90035-2**

Bukry, D., 1973. Low-latitude coccolith biostratigraphic zonation. *In* Edgar, N.T., Saunders, J.B., et al., *Init. Repts. DSDP,* 15: Washington, DC (U.S. Govt. Printing Office), 685–703. **doi:10.2973/dsdp.proc.15.116.1973**

Bukry, D., 1975. Coccolith and silicoflagellate stratigraphy, northwestern Pacific Ocean, Deep Sea Drilling Project Leg 32. *In* Larson, R.L., Moberly, R., et al., *Init. Repts. DSDP,* 32: Washington, DC (U.S. Govt. Printing Office), 677–701. **doi:10.2973/dsdp.proc.32.124.1975**

Burnett, J.A., 1998. Upper Cretaceous. *In* Bown, P.R. (Ed.), *Calcareous Nannofossil Biostratigraphy:* Dordrecht, The Netherlands (Kluwer Academic Publ.), 132–199.

Carlisle, D., 1963. Pillow breccias and their aquagene tuffs, Quadra Island, British Columbia. *J. Geol.,* 71(1):48–71. **doi:10.1086/626875**

Caron, M., 1985. Cretaceous planktic foraminifera. *In* Bolli, H.M., Saunders, J.B., and Perch-Nielsen, K. (Eds.), *Plankton Stratigraphy:* Cambridge (Cambridge Univ. Press), 17–86.

Channell, J.E.T., Erba, E., Nakanishi, M., and Tamaki, K., 1995. Late Jurassic–Early Cretaceous time scales and oceanic magnetic anomaly block models. *In* Berggren, W.A., Kent, D.V., Aubry, M.-P., and Hardenbol, J. (Eds.), *Geochronology, Time Scales, and Global Stratigraphic Correlation.* Spec. Publ.—SEPM (Soc. Sediment. Geol.), 54:51–63. **http://sp.sepmonline.org/content/sepspecpub/sepspgec/1/SEC4.body.pdf**

Clague, D.A., Paduan, J.B., and Davis, A.S., 2009. Widespread strombolian eruptions of mid-ocean ridge basalt. *J. Volcanol. Geotherm. Res.,* 180(2–4):171–188. **doi:10.1016/j.jvolgeores.2008.08.007**

Dixon, J.E., 1995. An experimental study of water and carbon dioxide solubilities in mid-ocean ridge basaltic liquids, Part II. Application to degassing. *J. Petrol.,* 36(6):1633–1646. **http://petrology.oxfordjournals.org/cgi/reprint/36/6/1633**

Droser, M.L., and Bottjer, D.J., 1986. A semiquantitative field classification of ichnofabric. *J. Sediment. Res.,* 56(4):558–559. **http://jsedres.sepmonline.org/cgi/content/abstract/56/4/558**

Ellis, D.V., and Singer, J.M., 2007. *Well Logging for Earth Scientists, Second Edition:* Dordrecht, The Netherlands (Springer).

Erba, E., Premoli Silva, I., Wilson, P.A., Pringle, M.S., Sliter, W.V., Watkins, D.K., Arnaud Vanneau, A., Bralower, T.J., Budd, A.F., Camoin, G.F., Masse, J.-P., Mutterlose, J., and Sager, W.W., 1995. Synthesis of stratigraphies from shallow-water sequences at Sites 871 through 879 in the western Pacific Ocean. *In* Haggerty, J.A., Premoli Silva, I., Rack, F., and McNutt, M.K. (Eds.), *Proc. ODP, Sci. Results,* 144: College Station, TX (Ocean Drilling Program), 873–885. **doi:10.2973/odp.proc.sr.144.076.1995**

Expedition 309/312 Scientists, 2006. Methods. *In* Teagle, D.A.H., Alt, J.C., Umino, S., Miyashita, S., Banerjee, N.R., Wilson, D.S., and the Expedition 309/312 Scientists. *Proc. IODP,* 309/312: Washington, DC (Integrated Ocean Drilling Program Management International, Inc.). **doi:10.2204/iodp.proc.309312.102.2006**

Expedition 320T Scientists, 2009. USIO Sea Trials and Assessment of Readiness Transit (START): Ontong Java Plateau. *IODP Prel. Rept.,* 320T. **doi:10.2204/iodp.pr.320T.2009**

Fisher, R.V., 1961. Proposed classification of volcaniclastic sediments and rocks. *Geol. Soc. Am. Bull.,* 72(9):1409–1414. **doi:10.1130/0016-7606(1961)72[1409:PCOVSA]2.0.CO;2**

Fisher, R.V., and Schmincke, H.-U., 1984. *Pyroclastic Rocks:* New York (Springer-Verlag).

Frey, F.A., Coffin, M.F., Wallace, P.J., Weis, D., Zhao, X., Wise, S.W., Jr., Wähnert, V., Teagle, D.A.H., Saccocia, P.J., Reusch, D.N., Pringle, M.S., Nicolaysen, K.E., Neal, C.R., Müller, R.D., Moore, C.L., Mahoney, J.J., Keszthelyi, L., Inokuchi, H., Duncan, R.A., Delius, H., Damuth, J.E., Damasceno, D., Coxall, H.K., Borre, M.K., Boehm, F., Barling, J., Arndt, N.T., and Antretter, M., 2000. Origin and evolution of a submarine large igneous province: the Kerguelen Plateau and Broken Ridge, southern Indian Ocean. *Earth Planet. Sci. Lett.,* 176(1):73–89. **doi:10.1016/S0012-821X(99)00315-5**

Goldberg, D., 1990. Test performance of the Ocean Drilling Program wireline heave motion compensator. *Sci. Drill.,* 1:206–209.

Goldberg, D., 1997. The role of downhole measurements in marine geology and geophysics. *Rev. Geophys.,* 35(3):315–342. **doi:10.1029/97RG00221**

Gradstein, F.M., 1978. Biostratigraphy of Lower Cretaceous Blake Nose and Blake Bahama Basin foraminifers, DSDP Leg 44, western North Atlantic Ocean. *In* Benson, W.E., Sheridan, R.E., et al., *Init. Repts. DSDP,* 44: Washington, DC (U.S. Govt. Printing Office), 663–702. **doi:10.2973/dsdp.proc.44.132.1978**

Gradstein, F.M., Agterberg, F.P., Ogg, J.G., Hardenbol, J., van Veen, P., Thierry, J., and Huang, Z., 1995. A Triassic, Jurassic and Cretaceous time scale. *In* Berggren, W.A., Kent, D.V., Aubry, M.-P., and Hardenbol, J. (Eds.), *Geo-*

chronology, Time Scales and Global Stratigraphic Correlation. Spec. Publ.—SEPM (Soc. Sedimet. Geol.), 54:95–126. **http://sp.sepmonline.org/content/sepspecpub/sepspgec/1/SEC7.body.pdf**

Greene, A.R., Scoates, J.S., Weis, D., Katvala, E.C., Israel, S., and Nixon, G.T., 2010. The architecture of oceanic plateaus revealed by the volcanic stratigraphy of the accreted Wrangellia oceanic plateau. *Geosphere,* 6(1):47–73. **doi:10.1130/GES00212.1**

Gregg, T.K.P., and Fink, J.H., 1995. Quantification of submarine lava-flow morphology through analog experiments. *Geology,* 23(1):73–76. **doi:10.1130/0091-7613(1995)023<0073:QOSLFM>2.3.CO;2**

Guilbaud, M.-N., Self, S., Thordarson, T., and Blake, S., 2005. Morphology, surface structures, and emplacement of lavas produced by Laki, A.D. 1783–1784. *In* Manga, M., and Ventura, G. (Eds.), *Kinematics and Dynamics of Lava Flows.* Spec. Pap.—Geol. Soc. Am., 396:81–102.

Holbourn, A., Kuhnt, W., and Soeding, E., 2001. Atlantic paleobathymetry, paleoproductivity and paleocirculation in the late Albian: the benthic foraminiferal record. *Palaeogeogr., Palaeoclimatol., Palaeoecol.,* 170(3–4):171–196. **doi:10.1016/S0031-0182(01)00223-1**

Holbourn, A.E.L., and Kaminski, M.A., 1997. *Lower Cretaceous Deep-Water Benthic Foraminifera of the Indian Ocean.* Spec. Publ.—Grzybowski Found., 4.

Hon, K., Kauahikaua, J., Denlinger, R., and Mackay, K., 1994. Emplacement and inflation of pahoehoe sheet flows: observations and measurements of active lava flows on Kilauea Volcano, Hawaii. *Geol. Soc. Am. Bull.,* 106(3):351–370. **doi:10.1130/0016-7606(1994)106<0351:EAIOPS>2.3.CO;2**

Jerram, D.A., and Widdowson, M., 2005. The anatomy of continental flood basalt provinces: geological constraints on the processes and products of flood volcanism. *Lithos,* 79(3–4):385–405. **doi:10.1016/j.lithos.2004.09.009**

Jones, R.W., and Wonders, A.A.H., 1992. Benthic foraminifers and paleobathymetry of Barrow Group (Berriasian–Valanginian) deltaic sequences, Sites 762 and 763, northwest shelf, Australia. *In* von Rad, U., Haq, B.U., et al., *Proc. ODP, Sci. Results,* 122: College Station, TX (Ocean Drilling Program), 557–568. **doi:10.2973/odp.proc.sr.122.174.1992**

Keene, J.B., 1975. Cherts and porcellanites from the North Pacific DSDP, Leg 32. *In* Larson, R.L., Moberly, R., et al. *Init. Repts. DSDP,* 32: Washington, DC (U.S. Govt. Printing Office), 429–507. **doi:10.2973/dsdp.proc.32.114.1975**

Keszthelyi, L., 2002. Classification of the mafic lava flows from ODP Leg 183. *In* Frey, F.A., Coffin, M.F., Wallace, P.J., and Quilty, P.G. (Eds.), *Proc. ODP, Sci. Results,* 183: College Station, TX (Ocean Drilling Program), 1–28. **doi:10.2973/odp.proc.sr.183.012.2002**

Kirschvink, J.L., 1980. The least-squares line and plane and the analysis of palaeomagnetic data. *Geophys. J. R. Astron. Soc.,* 62(3):699–718. **doi:10.1111/j.1365-246X.1980.tb02601.x**

Kokelaar, B.P., 1982. Fluidization of wet sediments during the emplacement and cooling of various igneous bodies. *J. Geol. Soc.,* 139(1):21–33. **doi:10.1144/gsjgs.139.1.0021**

Koutsoukos, E.A.M., and Hart, M.B., 1990. Cretaceous foraminiferal morphogroup distribution patterns, palaeocommunities and trophic structures: a case study from the Sergipe Basin, Brazil. *Trans. R. Soc. Edinburgh: Earth Sci.,* 81:221–246.

Leckie, R.M., Bralower, T.J., and Cashman, R., 2002. Oceanic anoxic events and plankton evolution: biotic response to tectonic forcing during the mid-Cretaceous. *Paleoceanography,* 17(3):1041. **doi:10.1029/2001PA000623**

Loeblich, A.R., Jr., and Tappan, H., 1988. *Foraminiferal Genera and Their Classification:* New York (Van Nostrand Reinhold).

Lonsdale, P., and Spiess, F.N., 1980. Deep-tow observations at the East Pacfic Rise, 8°45′N, and some interpretations. *In* Rosendahl, B.R., Hekinian, R., et al., *Init. Repts. DSDP,* 54: Washington, DC (U.S. Govt. Printing Office), 43–62. **doi:10.2973/dsdp.proc.54.104.1980**

Lovell, M.A., Harvey, P.K., Brewer, T.S., Williams, C., Jackson, P.D., and Williamson, G., 1998. Application of FMS images in the Ocean Drilling Program: an overview. *In* Cramp, A., MacLeod, C.J., Lee, S.V., and Jones, E.J.W. (Eds.), *Geological Evolution of Ocean Basins: Results from the Ocean Drilling Program.* Geol. Soc. Spec. Publ., 131(1):287–303. **doi:10.1144/GSL.SP.1998.131.01.18**

Luterbacher, H., 1973. Early Cretaceous foraminifera from the northwestern Pacific: Leg 32 of the Deep Sea Drilling Project. *In* Larson, R.L., Moberly, R., et al., *Init. Reports DSDP,* 32: Washington, DC (U.S. Govt. Printing Office), 703–718. **10.2973/dsdp.proc.32.125.1975**

Luthi, S.M., 1990. Sedimentary structures of clastic rocks identified from electrical borehole images. *In* Hurst, A., Lovell, M.A., and Morton, A.C. (Eds.), *Geological Applications of Wireline Logs.* Geol. Soc. Spec. Publ., 48(1):3–10. **doi:10.1144/GSL.SP.1990.048.01.02**

Macdonald, G.A., 1953. Pahoehoe, a'a, and block lava. *Am. J. Sci.,* 251:169–191.

Macdonald, G.A., 1967. Forms and structures of extrusive basaltic rocks. *Basalts—The Poldervaart Treatise on Rocks of Basaltic Composition:* New York (Wiley-Interscience Publ.), 1:1–61.

MacKenzie, W.S., Donaldson, C.H., and Guilford, C., 1982. *Atlas of Igneous Rocks and Their Textures:* New York (Wiley).

Mahoney, J.J., Fitton, J.G., Wallace, P.J., et al., 2001. *Proc. ODP, Init. Repts.,* 192: College Station, TX (Ocean Drilling Program). **doi:10.2973/odp.proc.ir.192.2001**

Mazzullo, J.M., Meyer, A., and Kidd, R.B., 1988. New sediment classification scheme for the Ocean Drilling Program. *In* Mazzullo, J.M., and Graham, A.G. (Eds.), *Handbook for shipboard sedimentologists.* ODP Tech. Note, 8:45–67. **doi:10.2973/odp.tn.8.1988**

Michael, F.Y., 1972. Planktonic foraminifera from the Comanchean Series (Cretaceous) of Texas. *J. Foraminiferal Res.,* 2(4):200–220. **doi:10.2113/gsjfr.2.4.200**

Mitchell, N.C., Beier, C., Rosin, P.L., Quartau, R., and Tempera, F., 2008. Lava penetrating water: submarine lava flows around the coasts of Pico Island, Azores. *Geochem.,* *Geophys., Geosyst.,* 9(3):Q03024. **doi:10.1029/2007GC001725**

Moullade, M., Bellier, J.-P., and Tronchetti, G., 2002. Hierarchy of criteria, evolutionary processes and taxonomic simplification in the classification of Lower Cretaceous planktonic foraminifera. *Cretaceous Res.,* 23:(1)111–148. **doi:10.1006/cres.2002.0304**

Munsell Color Company, Inc., 1994. *Munsell Soil Color Chart* (Revised ed.): Newburgh, MD (Munsell Color).

Murray, R.W., Miller, D.J., and Kryc, K.A., 2000. Analysis of major and trace elements in rocks, sediments, and interstitial waters by inductively coupled plasma–atomic emission spectrometry (ICP-AES). *ODP Tech. Note,* 29. **doi:10.2973/odp.tn.29.2000**

Nederbragt, A.J., 1991. Late Cretaceous biostratigraphy and development of Heterohelicidae (planktic foraminifera). *Micropaleontology,* 37(4):329–372. **doi:10.2307/1485910**

Nyong, E.E., and Olsson, R.K., 1984. A paleoslope model of Campanian to lower Maestrichtian foraminifera in the North American Basin and adjacent continental margin. *Mar. Micropaleontol.,* 8(6):437–477. **doi:10.1016/0377-8398(84)90009-4**

Okada, H., and Bukry, D., 1980. Supplementary modification and introduction of code numbers to the low-latitude coccolith biostratigraphic zonation (Bukry, 1973; 1975). *Mar. Micropaleontol.,* 5:321–325. **doi:10.1016/0377-8398(80)90016-X**

Paillet, F.L., and Kim, K., 1987. Character and distribution of borehole breakouts and their relationship to in situ stresses in deep Columbia River basalts. *J. Geophys. Res., [Solid Earth],* 92(B7):6223–6234. **doi:10.1029/JB092iB07p06223**

Passchier, C.W., and Trouw, R.A.J., 1996. *Microtectonics:* Berlin (Springer-Verlag).

Perch-Nielsen, K., 1985. Mesozoic calcareous nannofossils. *In* Bolli, H.M., Saunders, J.B., and Perch-Nielsen, K. (Eds.), *Plankton Stratigraphy:* Cambridge (Cambridge Univ. Press), 329–426.

Petrizzo, M.R., and Huber, B.T., 2006. On the phylogeny of the late Albian genus *Planomalina. J. Foraminiferal Res.,* 36(3):233–240. **doi:10.2113/gsjfr.36.3.233**

Premoli Silva, I., and Sliter, W.V., 1999. Cretaceous paleoceanography: evidence from planktonic foraminiferal evolution. *In* Barrera, E., and Johnson, C.C. (Eds.), *The Evolution of Cretaceous Ocean-Climatic System.* Spec. Pap.—Geol. Soc. Am., 332:301–328.

Ramsay, J.G., and Huber, M.I., 1987. *The Techniques of Modern Structural Geology* (Vol. 2): *Folds and Fractures:* New York (Acad. Press).

Rider, M.H., 1996. *The Geological Interpretation of Well Logs* (2nd ed.): Caithness (Whittles Publ.).

Robaszynski, F., and Caron, M., 1995. Foraminifères planctoniques du Crétacé: commentaire de la zonation Europe-Méditerranée. *Bull. Soc. Geol. Fr.,* 166:681–692.

Robaszynski, F., Caron, M., Gonzales-Donoso, J.-M., Wonders, A.A.H., and the European Working Group on Planktonic Foraminifera, 1984. Atlas of Late Cretaceous globotruncanids. *Rev. Micropaleontol.,* 26:145–305.

Robinson, S., Mrozewski, S., Hussein, T., Masterson, W., Meissner, E., Williams, T., Keogh, W., Myers, G., Bartington, G., and Goldberg, D., 2008. A new borehole magnetic susceptibility tool for high-resolution formation evaluation. In *SPWLA 49th Annual Logging Symposium: Abstracts.* Petrophys. Houston, 49(2):196–197.

Roth, P.H., 1978. Cretaceous nannoplankton biostratigraphy and oceanography of the northwestern Atlantic Ocean. *In* Benson, W.E., Sheridan, R.E., et al., *Init. Repts. DSDP,* 44: Washington, DC (U.S. Govt. Printing Office), 731–759. **doi:10.2973/dsdp.proc.44.134.1978**

Roth, P.H., 1983. Jurassic and Lower Cretaceous calcareous nannofossils in the western North Atlantic (Site 534): biostratigraphy, preservation, and some observations on biogeography and paleoceanography. *In* Sheridan, R.E., Gradstein, F.M., et al., *Init. Repts. DSDP,* 76: Washington, DC (U.S. Govt. Printing Office), 587–621. **doi:10.2973/dsdp.proc.76.125.1983**

Salimullah, A.R.M., and Stow, D.A.V., 1992. Application of FMS images in poorly recovered coring intervals: examples from ODP Leg 129. *In* Hurst, A., Griffiths, C.M., and Worthington, P.F. (Eds.), *Geological Application of Wireline Logs II.* Geol. Soc. Spec. Publ., 65(1):71–86. **doi:10.1144/GSL.SP.1992.065.01.06**

Schlumberger, 1989. *Log Interpretation Principles/Applications:* Houston (Schlumberger Educ. Services), SMP–7017.

Schlumberger, 1994. *IPL Integrated Porosity Lithology:* Houston (Schlumberger Wireline and Testing), SMP-9270.

Serra, O., 1984. *Fundamentals of Well-Log Interpretation* (Vol. 1): *The Acquisition of Logging Data:* Amsterdam (Elsevier).

Serra, O., 1986. *Fundamentals of Well-Log Interpretation* (Vol. 2): *The Interpretation of Logging Data.* Amsterdam (Elsevier).

Serra, O., 1989. *Formation MicroScanner Image Interpretation:* Houston (Schlumberger Educ. Serv.), SMP-7028.

Shipboard Scientific Party, 1989. Introduction and explanatory notes. *In* Robinson, P.T., Von Herzen, R., et al., *Proc. ODP, Init. Repts.,* 118: College Station, TX (Ocean Drilling Program), 3–23. **doi:10.2973/odp.proc.ir.118.101.1989**

Shipboard Scientific Party, 1991. Explanatory notes. *In* Taira, A., Hill, I., Firth, J.V., et al., *Proc. ODP, Init. Repts.,* 131: College Station, TX (Ocean Drilling Program), 25–60. **doi:10.2973/odp.proc.ir.131.104.1991**

Shipboard Scientific Party, 1992a. Explanatory notes. *In* Behrmann, J.H., Lewis, S.D., Musgrave, R.J., et al., *Proc. ODP, Init. Repts.,* 141: College Station, TX (Ocean Drilling Program), 37–71. **doi:10.2973/odp.proc.ir.141.105.1992**

Shipboard Scientific Party, 1992b. Explanatory notes. *In* Dick, H.J.B., Erzinger, J., Stokking, L.B., et al., *Proc. ODP, Init. Repts.,* 140: College Station, TX (Ocean Drilling Program), 5–33. **doi:10.2973/odp.proc.ir.140.101.1992**

Shipboard Scientific Party, 1992c. Explanatory notes. *In* Parson, L., Hawkins, J., Allan, J., et al., *Proc. ODP, Init. Repts.,* 135: College Station, TX (Ocean Drilling Program), 49–79. **doi:10.2973/odp.proc.ir.135.102.1992**

Shipboard Scientific Party, 1993a. Explanatory notes. *In* Alt, J.C., Kinoshita, H., Stokking, L.B., et al., *Proc. ODP, Init. Repts.,* 148: College Station, TX (Ocean Drilling Program), 5–24. **doi:10.2973/odp.proc.ir.148.101.1993**

Shipboard Scientific Party, 1993b. Explanatory notes. *In* Gillis, K., Mével, C, Allan, J., et al., *Proc. ODP, Init. Repts.,* 147: College Station, TX (Ocean Drilling Program), 15–42. **doi:10.2973/odp.proc.ir.147.102.1993**

Shipboard Scientific Party, 1995. Explanatory notes. *In* Cannat, M., Karson, J.A., Miller, D.J., et al., *Proc. ODP, Init. Repts.,* 153: College Station, TX (Ocean Drilling Program), 15–42. **doi:10.2973/odp.proc.ir.153.10X.1995**

Shipboard Scientific Party, 1999. Explanatory notes. *In* Dick, H.J.B., Natland, J.H., Miller, D.J., et al., *Proc. ODP, Init. Repts.,* 176: College Station, TX (Ocean Drilling Program), 1–42. **doi:10.2973/odp.proc.ir.176.102.1999**

Shipboard Scientific Party, 2000a. Explanatory notes. *In* Coffin, M.F., Frey, F.A., Wallace, P.J., et al., *Proc. ODP, Init. Repts.,* 183: College Station, TX (Ocean Drilling Program), 1–94. **doi:10.2973/odp.proc.ir.183.102.2000**

Shipboard Scientific Party, 2000b. Explanatory notes. *In* Sacks, I.S., Suyehiro, K., Acton, G.D., et al., *Proc. ODP, Init. Repts.,* 186: College Station, TX (Ocean Drilling Program), 1–51. **doi:10.2973/odp.proc.ir.186.102.2000**

Shipboard Scientific Party, 2002a. Explanatory notes. *In* Bralower, T.J., Premoli Silva, I., Malone, M.J., et al., *Proc. ODP, Init. Repts.,* 198: College Station, TX (Ocean Drilling Program), 1–63. **doi:10.2973/odp.proc.ir.198.102.2002**

Shipboard Scientific Party, 2002b. Explanatory notes. *In* Tarduno, J.A., Duncan, R.A., Scholl, D.W., et al., *Proc. ODP, Init. Repts.,* 197: College Station, TX (Ocean Drilling Program), 1–89. **doi:10.2973/odp.proc.ir.197.102.2002**

Shipboard Scientific Party, 2003a. An in situ section of upper oceanic crust formed by superfast seafloor spreading. *ODP Prelim. Rept.,* 206: College Station, TX (Ocean Drilling Program). **doi:10.2973/odp.pr.206.2003**

Shipboard Scientific Party, 2003b. Explanatory notes. *In* Wilson, D.S., Teagle, D.A.H., Acton, G.D., *Proc. ODP, Init. Repts.,* 206: College Station, TX (Ocean Drilling Program), 1–94. **doi:10.2973/odp.proc.ir.206.102.2003**

Sikora, P.J. and Olsson, R.K., 1991. A paleoslope model of late Albian to early Turonian foraminifera of the west Atlantic margin and North Atlantic Basin. *Mar. Micropaleontol.,* 8(1–2):25–72. **doi:10.1016/0377-8398(91)90005-Q**

Sissingh, W., 1977. Biostratigraphy of Cretaceous calcareous nannoplankton. *Geol. Mijnbouw,* 56:37–65.

Skilling, I.P., White, J.D.L., and McPhie, J., 2002. Peperite: a review of magma–sediment mingling. *J. Volcanol. Geotherm. Res.,* 114(1–2):1–17. **doi:10.1016/S0377-0273(01)00278-5**

Sliter, W.V., 1977. Cretaceous benthic foraminifers from the western South Atlantic Leg 39, Deep Sea Drilling Project. *In* Supko, P.R., Perch-Nielsen, K., et al., *Init. Repts. DSDP,* 39: Washington, DC (U.S. Govt. Printing Office), 657–697. **doi:10.2973/dsdp.proc.39.130.1977**

Sliter, W.V., 1980. Mesozoic foraminifers and deep-sea benthic environments from Deep Sea Drilling Project Sites 415 and 416, eastern North Atlantic. *In* Lancelot, Y., Winterer, E.L., et al., *Init. Repts. DSDP,* 50: Washington, DC (U.S. Govt. Printing Office), 353–427. **doi:10.2973/dsdp.proc.50.109.1980**

Sliter, W.V., 1989. Biostratigraphic zonation for Cretaceous planktonic foraminifers examined in thin section. *J. Foraminiferal Res.,* 19(1):1–19. **doi:10.2113/gsjfr.19.1.1**

Sliter, W.V., and Baker, R.A., 1972. Cretaceous bathymetric distribution of benthic foraminifers. *J. Foraminiferal Res.,* 2(4):167–183. **doi:10.2113/gsjfr.2.4.167**

Sparks, J.W., and Zuleger, E., 1995. Data report: chemical analyses of the Leg 140 reference sample. *In* Erzinger, J., Becker, K., Dick, H.J.B., Stokking, L.B. (Eds.), *Proc. ODP, Sci. Results,* 137/140: College Station, TX (Ocean Drilling Program), 353–355. **doi:10.2973/odp.proc.sr.137140.041.1995**

Staudigel, H., and Schmincke, H.-U., 1984. The Pliocene seamount series of La Palma/Canary Islands. *J. Geophys. Res., [Solid Earth],* 89(B13):11195–11215. **doi:10.1029/JB089iB13p11195**

Teagle, D.A.H., Alt, J.C., Umino, S., Miyashita, S., Banerjee, N.R., Wilson, D.S., and Expedition 309/312 Scientists, 2006. *Proc. IODP,* 309/312: Washington, DC (Integrated Ocean Drilling Program Management International, Inc.). **doi:10.2204/iodp.proc.309312.2006**

Thordarson, T., and Self, S., 1998. The Roza Member, Columbia River Basalt Group: a gigantic pahoehoe lava flow field formed by endogenous processes. *J. Geophys. Res., [Solid Earth],* 103(B11):27411–27445. **doi:10.1029/98JB01355**

Twiss, R.J., and Moores, E.M., 1992. *Structural Geology:* New York (Freeman).

Vacquier, V., 1985. The measurement of thermal conductivity of solids with a transient linear heat source on the plane surface of a poorly conducting body. *Earth Planet. Sci. Lett.,* 74(2–3):275–279. **doi:10.1016/0012-821X(85)90027-5**

van Andel, T.H., and Ballard, R.D., 1979. The Galapagos Rift at 86°W, 2. Volcanism, structure, and evolution of the rift valley. *J. Geophys. Res., [Solid Earth],* 84(B10):5379–5606. **doi:10.1029/JB084iB10p05390**

Verga, D., and Premoli Silva, I., 2003a. Early Cretaceous planktonic foraminifera from the Tethys: the large, many-chambered representatives of the genus *Globigerinelloides*. *Cretaceous Res.,* 24(6):661–690. **doi:10.1016/j.cretres.2003.07.007**

Verga, D., and Premoli Silva, I., 2003b. Early Cretaceous planktonic foraminifera from the Tethys: the small, few-chambered representatives of the genus *Globigerinelloides*. *Cretaceous Res.,* 24(3):305–334. **doi:10.1016/S0195-6671(03)00045-4**

Verga, D., and Premoli Silva, I., 2005. Early Cretaceous planktonic foraminifera from the Tethys: the upper Aptian, planispiral morphotypes with elongate chambers. *Cretaceous Res.,* 26(2):239–259. **doi:10.1016/j.cretres.2005.01.004**

Walker, G.P.L., 1971. Compound and simple lava flows and flood basalts. *Bull. Volcanol.,* 35(3):579–590. **doi:10.1007/BF02596829**

Walker, G.P.L., 1991. Structure, and origin by injection of lava under surface crust, of tumuli, "lava rises," "lava-rise pits," and "lava-inflation clefts" in Hawaii. *Bull. Volcanol.,* 53(7):546–558. **doi:10.1007/BF00298155**

Walker, G.P.L., 1992. Morphometric study of pillow-size spectrum among pillow lavas. *Bull. Volcanol.,* 54(6):459–474. **doi:10.1007/BF00301392**

Wallace, P.J., 1998. Pre-eruptive H_2O and CO_2 contents of mafic magmas from the submarine to emergent shield stages of Gran Canaria. *In* Weaver, P.P.E., Schmincke, H.-U., Firth, J.V., and Duffield, W. (Eds.), *Proc. ODP, Sci. Results,* 157: College Station, TX (Ocean Drilling Program), 411–420. **doi:10.2973/odp.proc.sr.157.146.1998**

Wentworth, C.K., 1922. A scale of grade and class terms for clastic sediments. *J. Geol.,* 30(5):377–392. **doi:10.1086/622910**

White, J.D.L., Bryan, S.E., Ross, P.S., Self, S., and Thordarson, T., 2009. Physical volcanology of continental large igneous provinces: update and review. *In* Thordarson, T., Self, S., Larsen, G., Rowland, S.K., and Hoskuldsson, A. (Eds.), *Studies in Volcanology: The Legacy of George Walker.* Spec. Publ. IAVCEI, 2:291–321.

Widmark, J.G.V., 1997. Deep-sea benthic foraminifera from Cretaceous–Tertiary boundary strata in the South Atlantic Ocean: taxonomy and paleoecology. *Fossils Strata,* 43:1–94.

Wilmoth, R.A., and Walker, G.P.L., 1993. P-type and S-type pahoehoe: a study of vesicle distribution patterns in Hawaiian lava flows. *J. Volcanol. Geotherm. Res.,* 55(1–2):129–142. **doi:10.1016/0377-0273(93)90094-8**

Publication: 3 November 2010
MS 324-102

Figure F1. Example of sedimentary VCD graphic report.

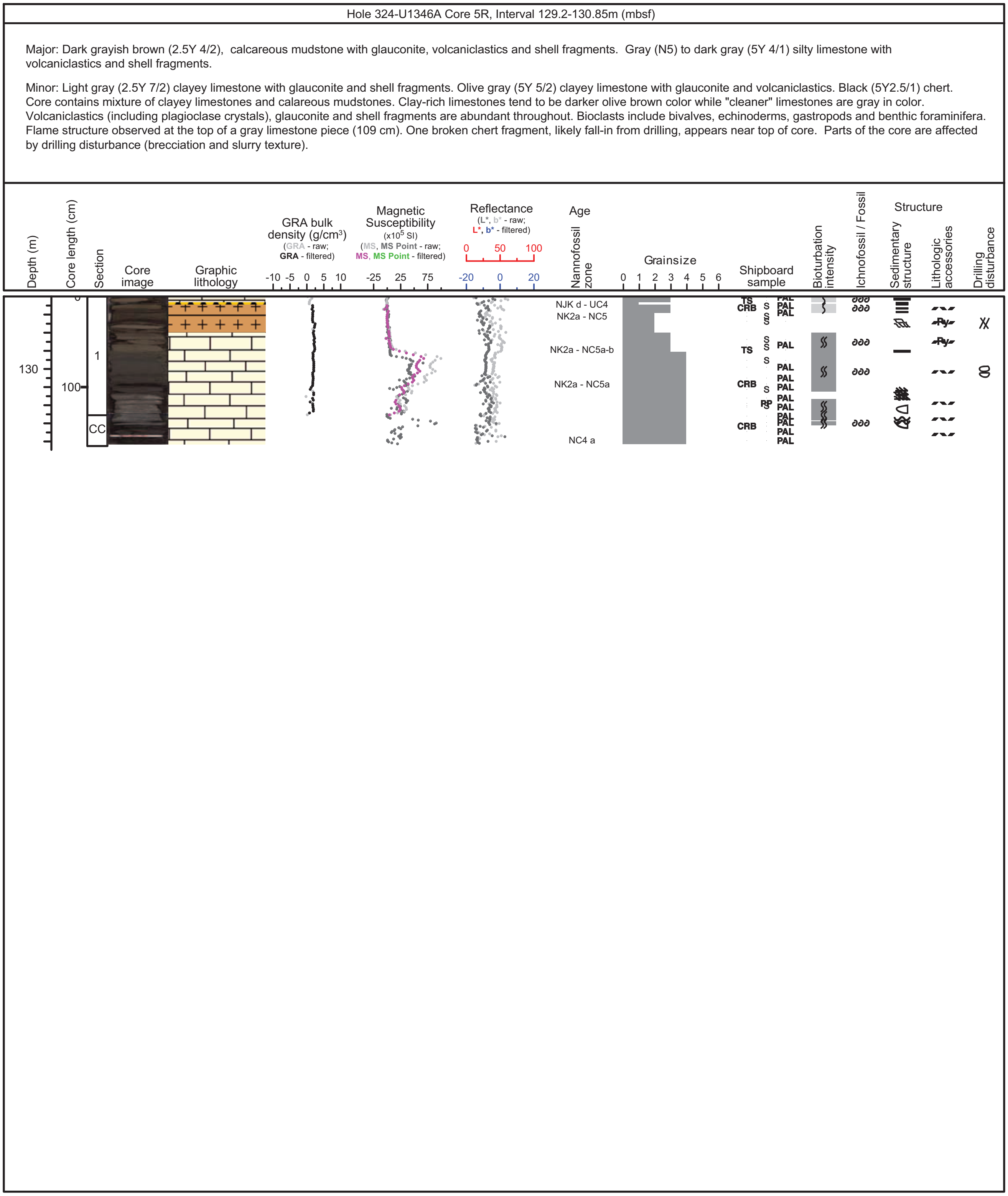

Hole 324-U1346A Core 5R, Interval 129.2-130.85m (mbsf)

Major: Dark grayish brown (2.5Y 4/2), calcareous mudstone with glauconite, volcaniclastics and shell fragments. Gray (N5) to dark gray (5Y 4/1) silty limestone with volcaniclastics and shell fragments.

Minor: Light gray (2.5Y 7/2) clayey limestone with glauconite and shell fragments. Olive gray (5Y 5/2) clayey limestone with glauconite and volcaniclastics. Black (5Y2.5/1) chert. Core contains mixture of clayey limestones and calareous mudstones. Clay-rich limestones tend to be darker olive brown color while "cleaner" limestones are gray in color. Volcaniclastics (including plagioclase crystals), glauconite and shell fragments are abundant throughout. Bioclasts include bivalves, echinoderms, gastropods and benthic foraminifera. Flame structure observed at the top of a gray limestone piece (109 cm). One broken chert fragment, likely fall-in from drilling, appears near top of core. Parts of the core are affected by drilling disturbance (brecciation and slurry texture).

Figure F2. Symbols and nomenclature used in sedimentary VCD graphic reports.

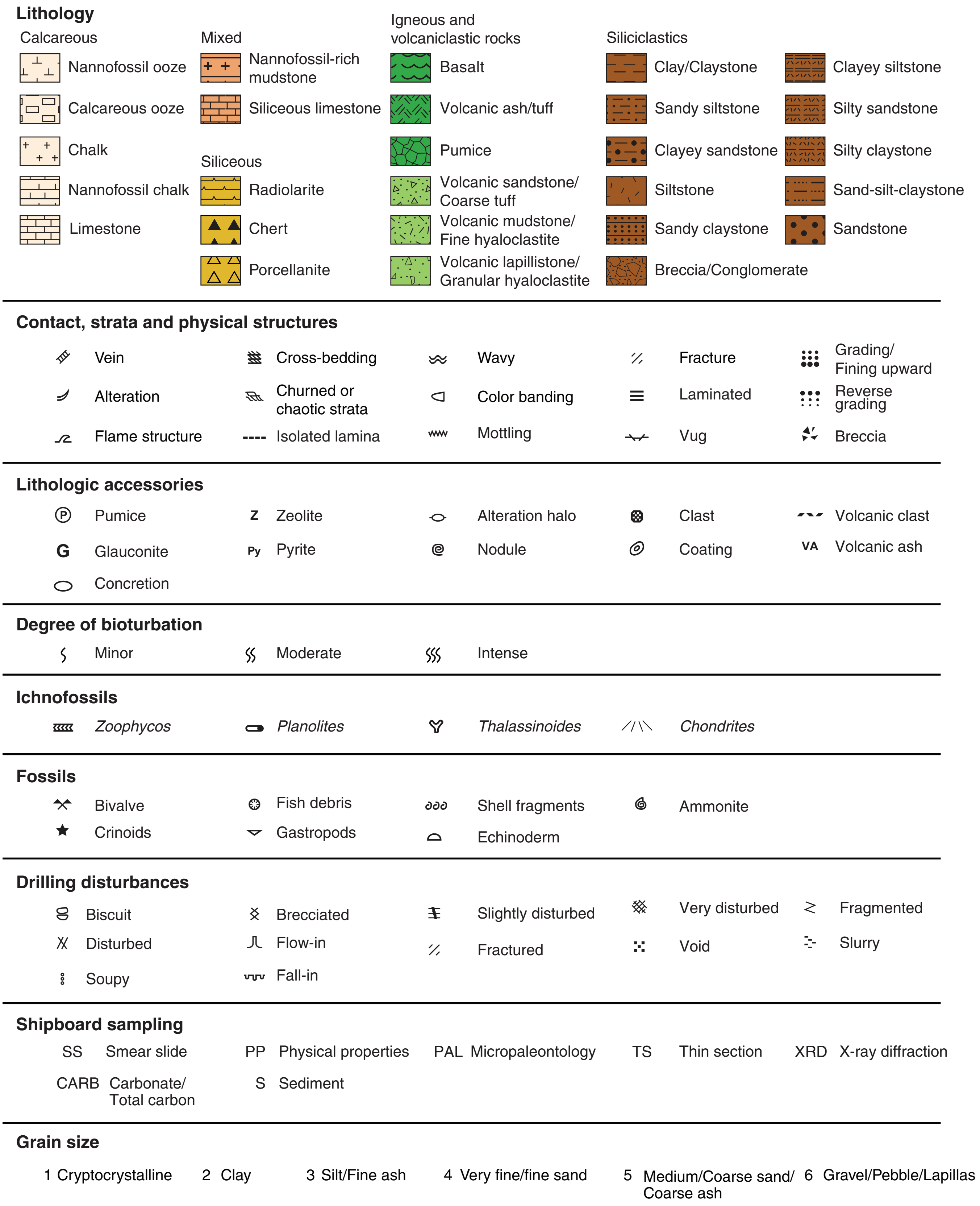

Figure F3. Table of grain size classification (Wentworth, 1922).

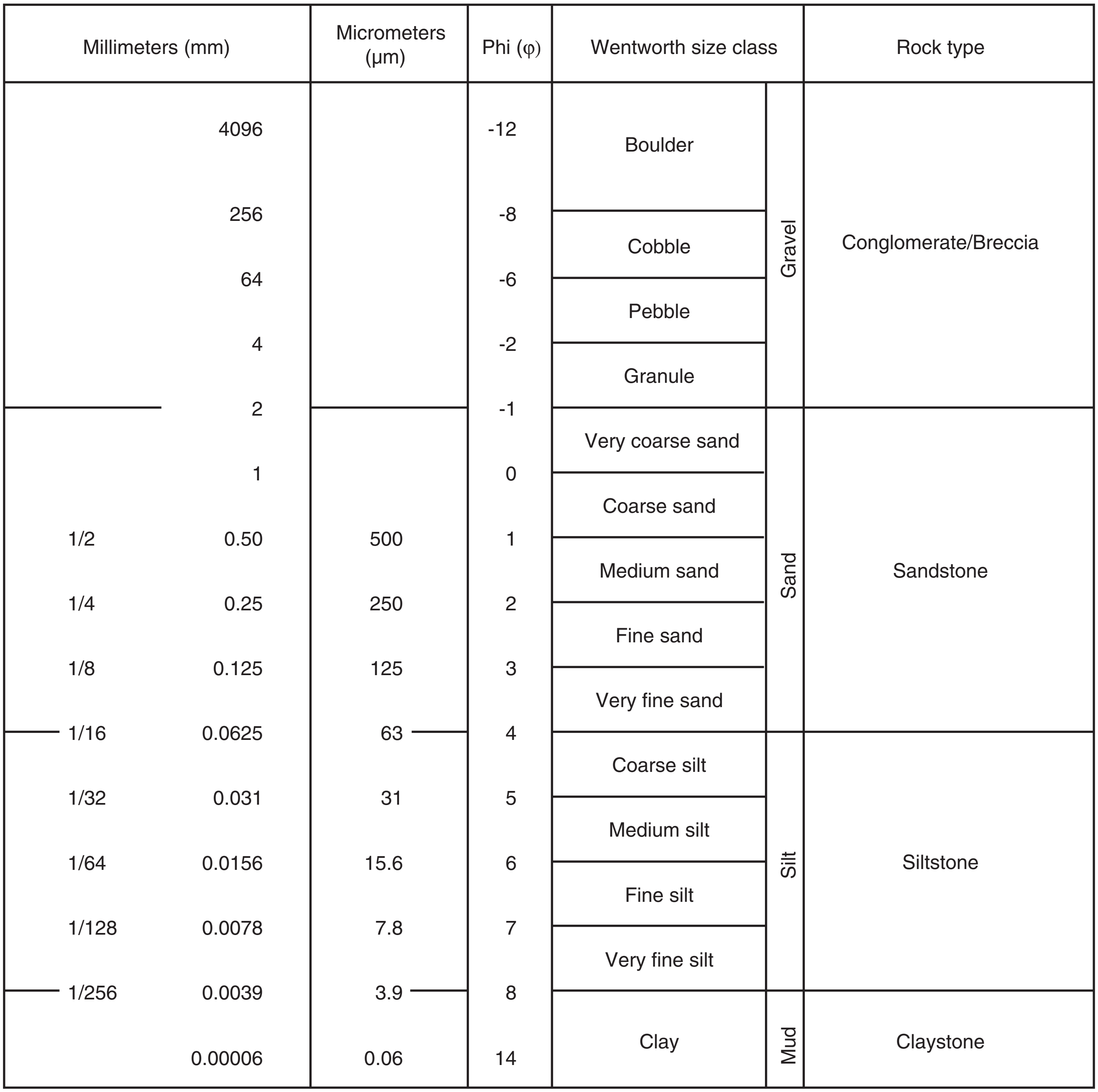

Millimeters (mm)		Micrometers (µm)	Phi (φ)	Wentworth size class		Rock type
	4096		-12	Boulder	Gravel	Conglomerate/Breccia
	256		-8	Cobble		
	64		-6	Pebble		
	4		-2	Granule		
	2		-1	Very coarse sand	Sand	Sandstone
	1		0	Coarse sand		
1/2	0.50	500	1	Medium sand		
1/4	0.25	250	2	Fine sand		
1/8	0.125	125	3	Very fine sand		
1/16	0.0625	63	4	Coarse silt	Silt	Siltstone
1/32	0.031	31	5	Medium silt		
1/64	0.0156	15.6	6	Fine silt		
1/128	0.0078	7.8	7	Very fine silt		
1/256	0.0039	3.9	8	Clay	Mud	Claystone
	0.00006	0.06	14			

Figure F4. Cretaceous timescale used for Expedition 324 with calcareous nannofossil and planktonic foraminifer zones and datums. B = base, T = top. **A.** 65–110 Ma. (Continued on next page.)

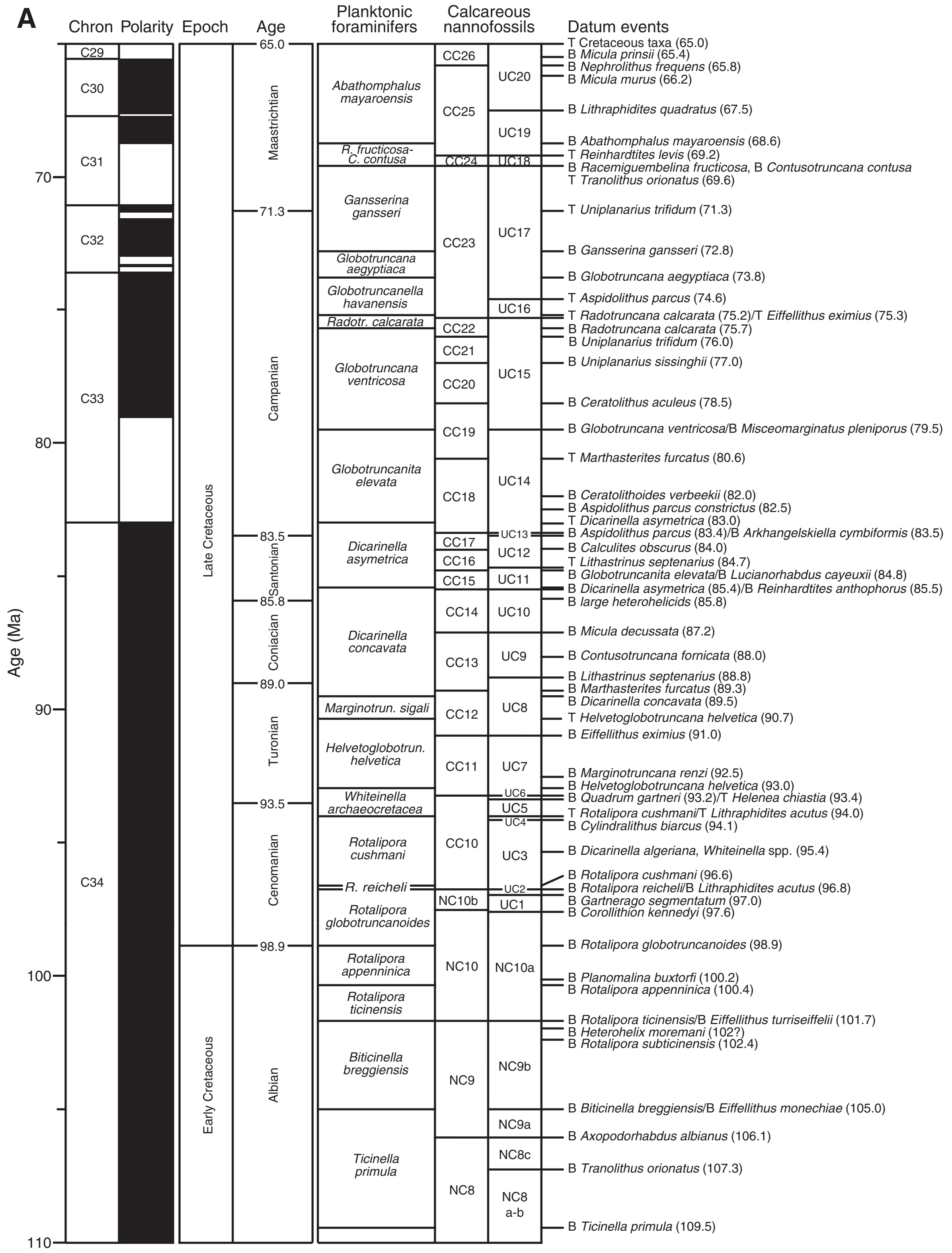

Figure F4 (continued). B. 102–147 Ma.

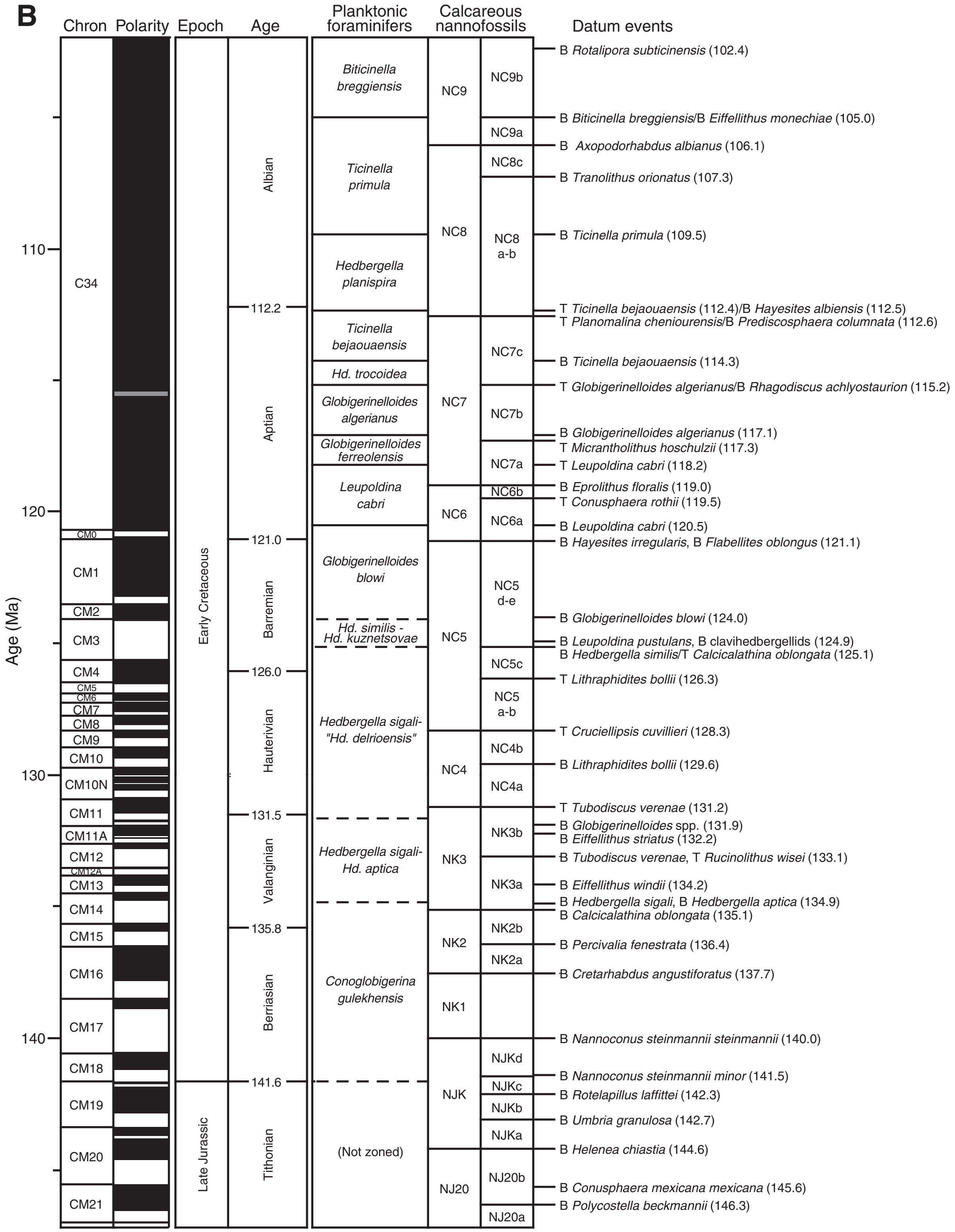

Figure F5. Nongenetic classification of volcanic rocks. Modified after the classification used by Shipboard Scientific Party (2002b), ODP Leg 197 (Emperor Seamounts).

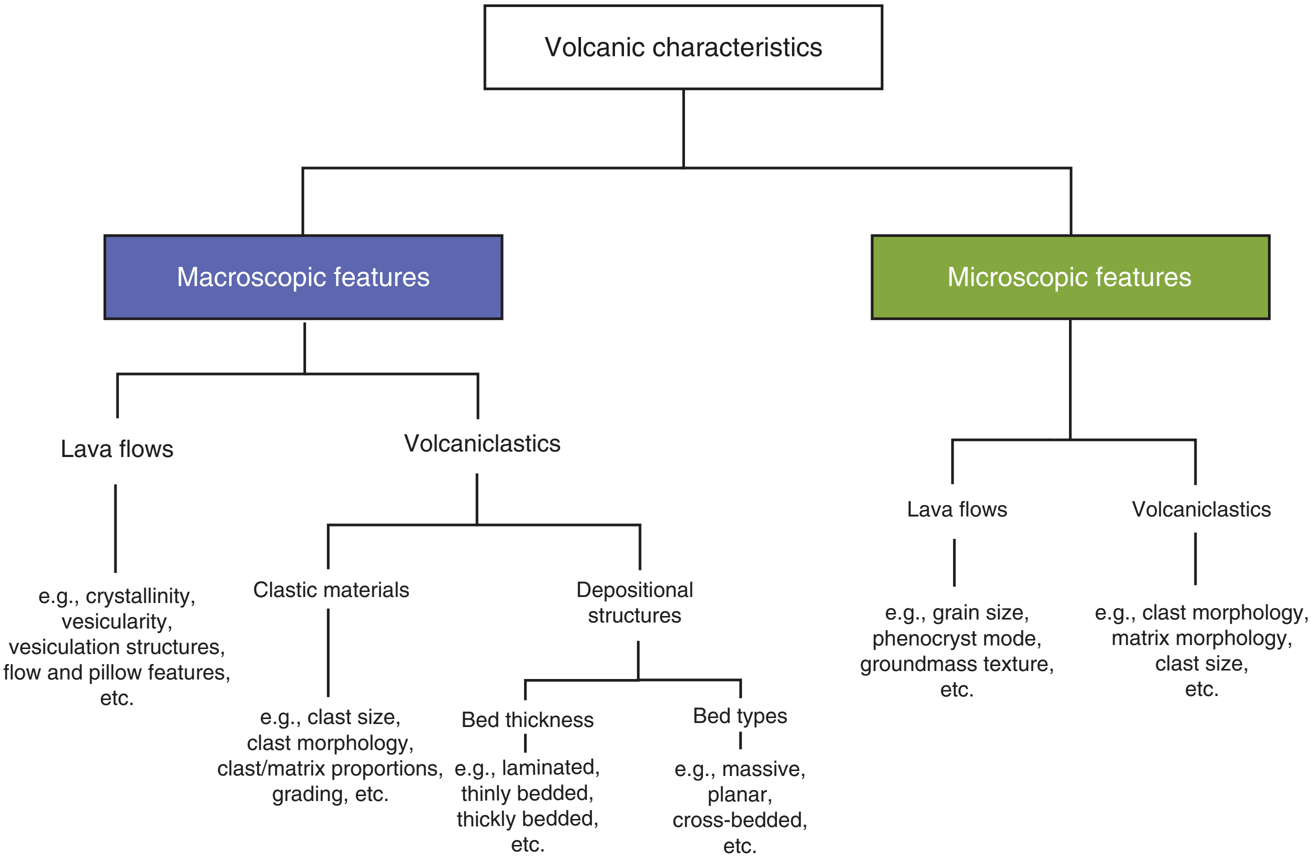

Figure F6. Genetic classification of volcanic rocks derived from effusive and explosive processes and associated volcaniclastic (pyroclastic, syneruptive, and epiclastic) sediments, Expedition 324. Classification modified after Shipboard Scientific Party (2002b), ODP Leg 197 (Emperor Seamounts). Italicized text denotes process involved.

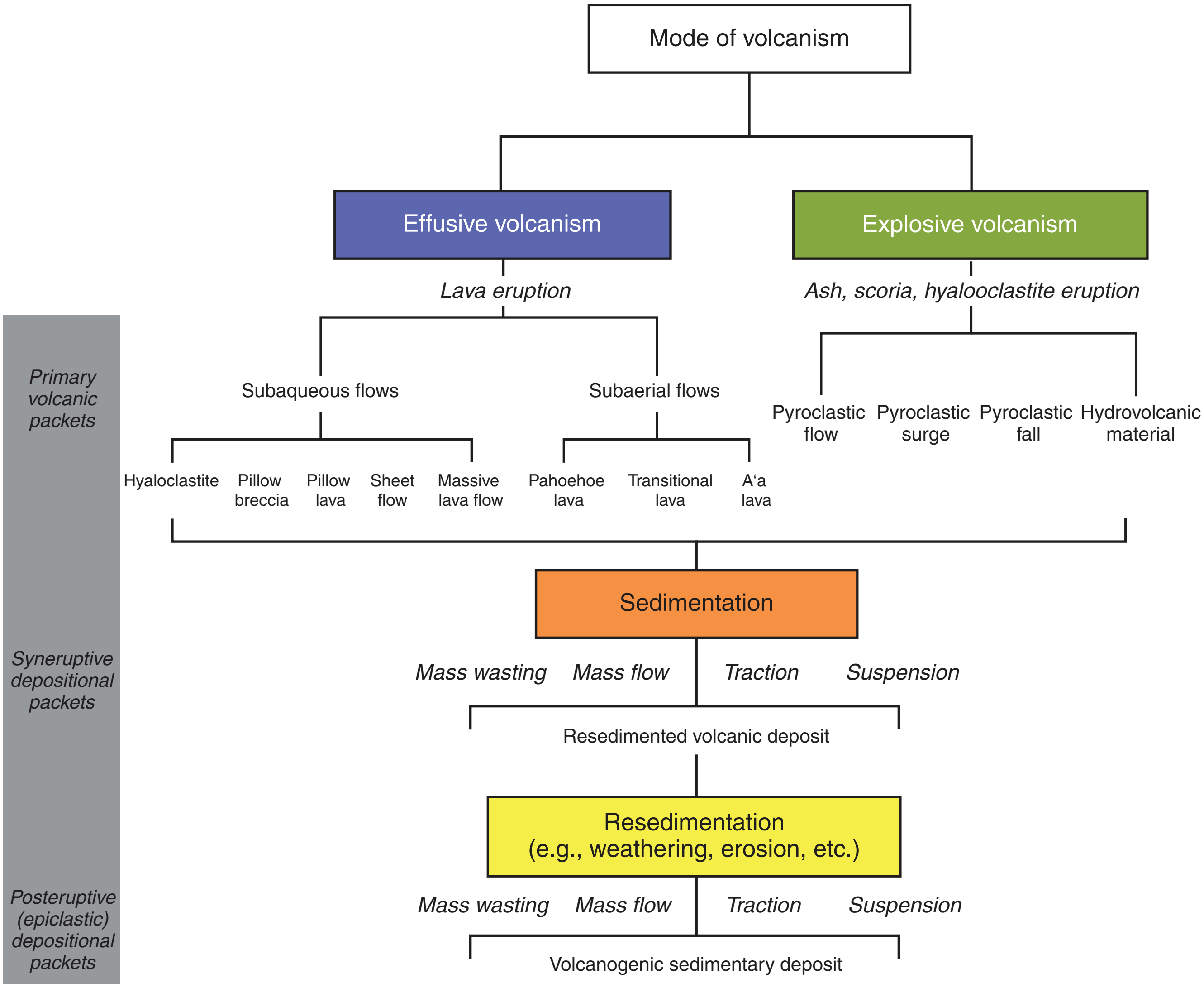

Figure F7. Likely four-stage evolution of the Shatsky Rise through analogy with the complete volcanic LIP series in the accreted Wrangellia Terrane (Greene et al., 2010). Volcanic facies associations reveal (**A**) initial deep water eruptive phase of pillowed and massive submarine flows, (**B**) shallow-water flow emplacement with increasing proportion of volcaniclastics, (**C**) emergent (subaerial) stage of plateau growth, and (**D**) waning eruption stage.

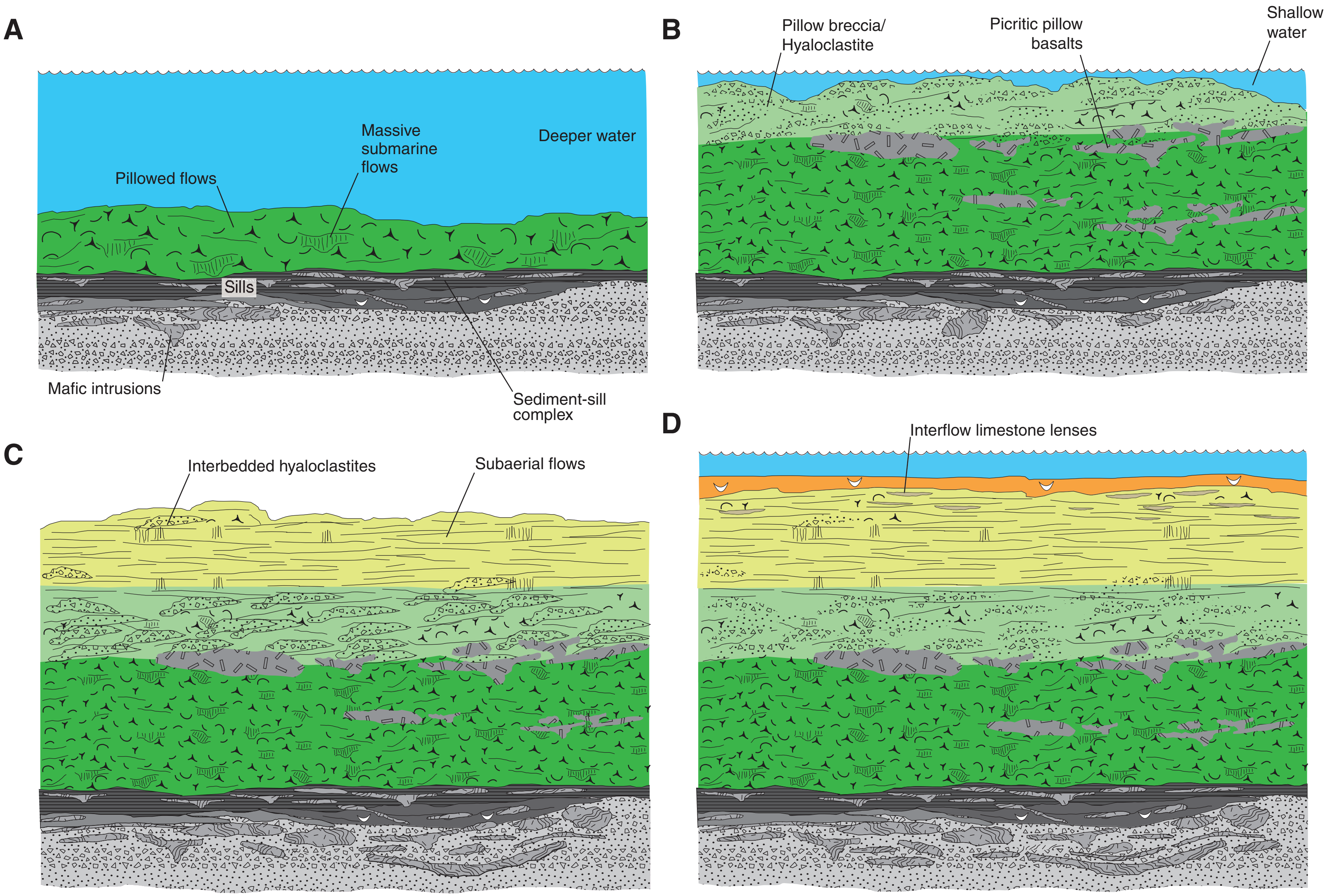

Figures F8. Example of igneous VCD graphic report.

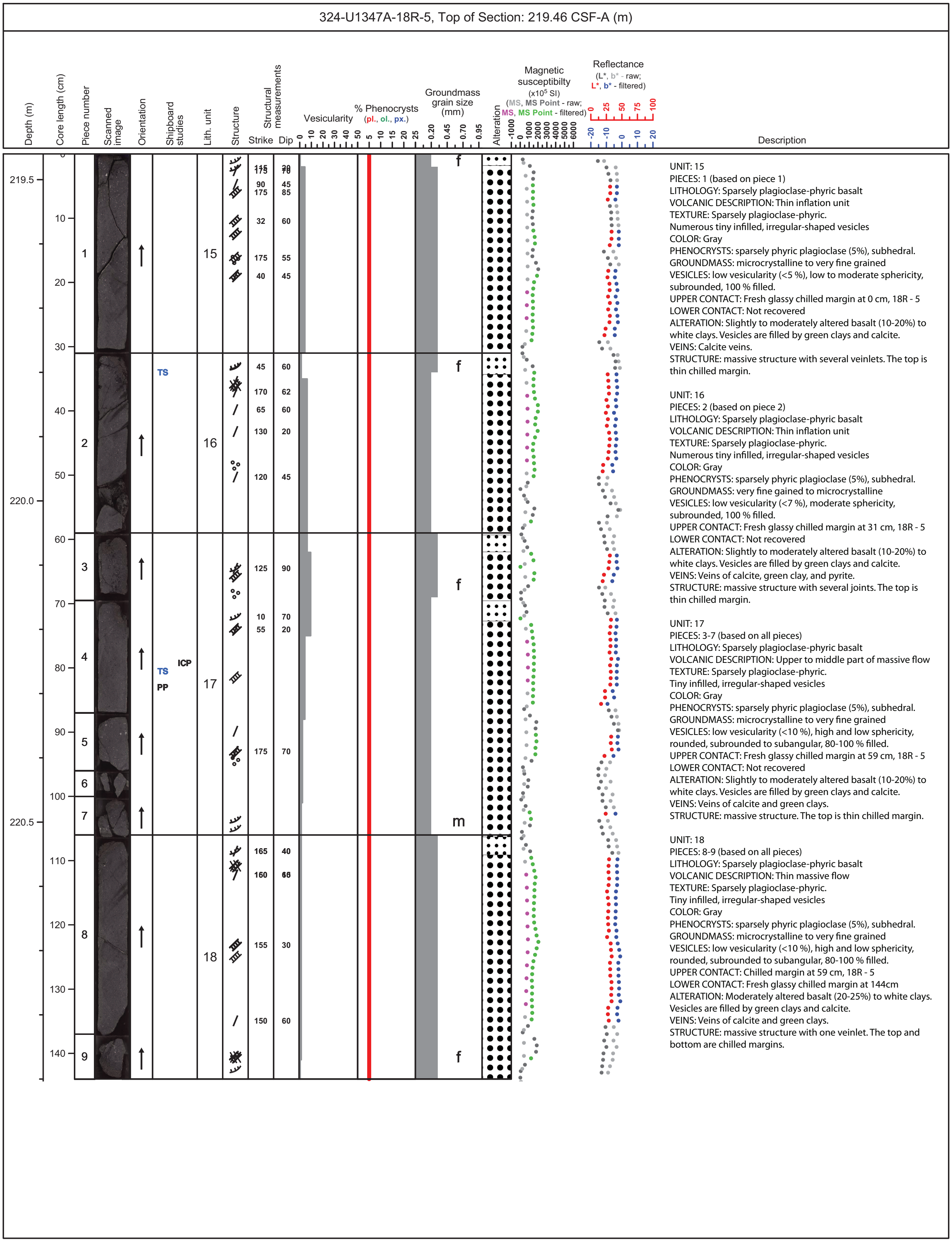

UNIT: 15
PIECES: 1 (based on piece 1)
LITHOLOGY: Sparsely plagioclase-phyric basalt
VOLCANIC DESCRIPTION: Thin inflation unit
TEXTURE: Sparsely plagioclase-phyric.
Numerous tiny infilled, irregular-shaped vesicles
COLOR: Gray
PHENOCRYSTS: sparsely phyric plagioclase (5%), subhedral.
GROUNDMASS: microcrystalline to very fine grained
VESICLES: low vesicularity (<5 %), low to moderate sphericity, subrounded, 100 % filled.
UPPER CONTACT: Fresh glassy chilled margin at 0 cm, 18R - 5
LOWER CONTACT: Not recovered
ALTERATION: Slightly to moderately altered basalt (10-20%) to white clays. Vesicles are filled by green clays and calcite.
VEINS: Calcite veins.
STRUCTURE: massive structure with several veinlets. The top is thin chilled margin.

UNIT: 16
PIECES: 2 (based on piece 2)
LITHOLOGY: Sparsely plagioclase-phyric basalt
VOLCANIC DESCRIPTION: Thin inflation unit
TEXTURE: Sparsely plagioclase-phyric.
Numerous tiny infilled, irregular-shaped vesicles
COLOR: Gray
PHENOCRYSTS: sparsely phyric plagioclase (5%), subhedral.
GROUNDMASS: very fine gained to microcrystalline
VESICLES: low vesicularity (<7 %), moderate sphericity, subrounded, 100 % filled.
UPPER CONTACT: Fresh glassy chilled margin at 31 cm, 18R - 5
LOWER CONTACT: Not recovered
ALTERATION: Slightly to moderately altered basalt (10-20%) to white clays. Vesicles are filled by green clays and calcite.
VEINS: Veins of calcite, green clay, and pyrite.
STRUCTURE: massive structure with several joints. The top is thin chilled margin.

UNIT: 17
PIECES: 3-7 (based on all pieces)
LITHOLOGY: Sparsely plagioclase-phyric basalt
VOLCANIC DESCRIPTION: Upper to middle part of massive flow
TEXTURE: Sparsely plagioclase-phyric.
Tiny infilled, irregular-shaped vesicles
COLOR: Gray
PHENOCRYSTS: sparsely phyric plagioclase (5%), subhedral.
GROUNDMASS: microcrystalline to very fine grained
VESICLES: low vesicularity (<10 %), high and low sphericity, rounded, subrounded to subangular, 80-100 % filled.
UPPER CONTACT: Fresh glassy chilled margin at 59 cm, 18R - 5
LOWER CONTACT: Not recovered
ALTERATION: Slightly to moderately altered basalt (10-20%) to white clays. Vesicles are filled by green clays and calcite.
VEINS: Veins of calcite and green clays.
STRUCTURE: massive structure. The top is thin chilled margin.

UNIT: 18
PIECES: 8-9 (based on all pieces)
LITHOLOGY: Sparsely plagioclase-phyric basalt
VOLCANIC DESCRIPTION: Thin massive flow
TEXTURE: Sparsely plagioclase-phyric.
Tiny infilled, irregular-shaped vesicles
COLOR: Gray
PHENOCRYSTS: sparsely phyric plagioclase (5%), subhedral.
GROUNDMASS: microcrystalline to very fine grained
VESICLES: low vesicularity (<10 %), high and low sphericity, rounded, subrounded to subangular, 80-100 % filled.
UPPER CONTACT: Chilled margin at 59 cm, 18R - 5
LOWER CONTACT: Fresh glassy chilled margin at 144cm
ALTERATION: Moderately altered basalt (20-25%) to white clays. Vesicles are filled by green clays and calcite.
VEINS: Veins of calcite and green clays.
STRUCTURE: massive structure with one veinlet. The top and bottom are chilled margins.

Figure F9. Symbols and nomenclature used in igneous VCD graphic reports. ICP-AES = inductively coupled plasma–atomic emission spectroscopy.

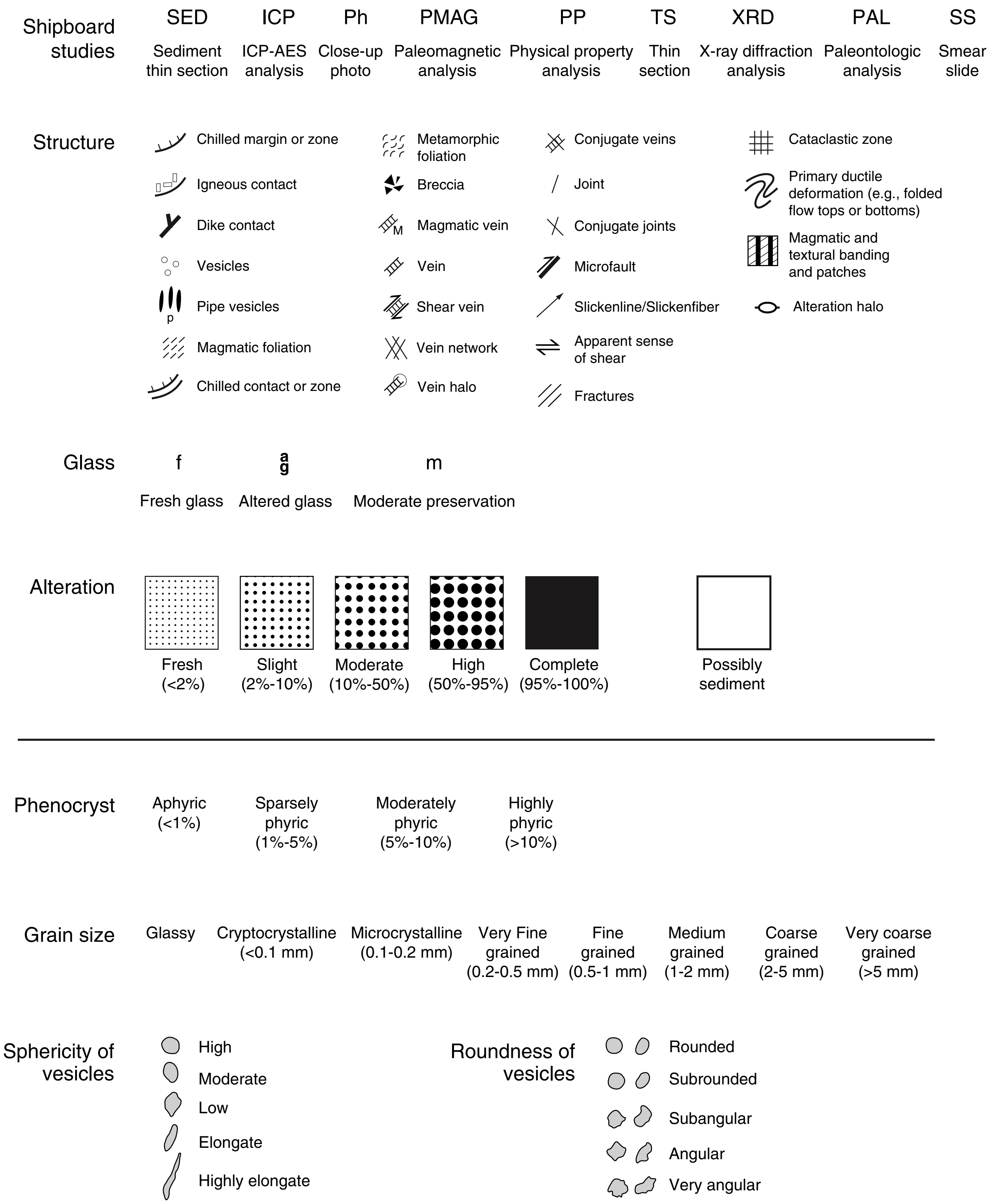

Figure F10. DESClogik data entry software templates for (**A**) volcanologic and petrographic observations and (**B**) description of volcanic features. Data are uploaded from DESClogik into the LIMS database and used to develop the VCD graphic report.

A

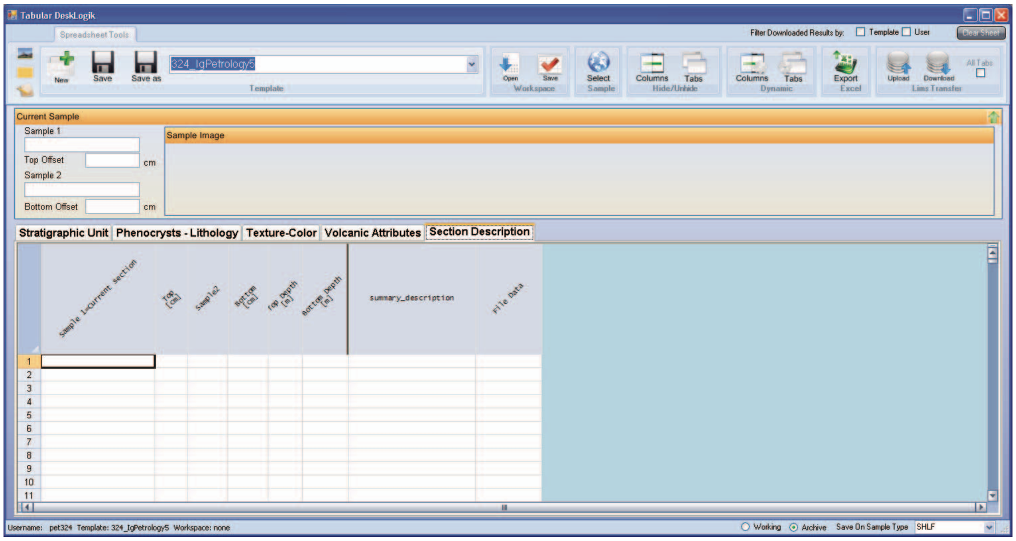

Username: pet324 Template: 324_IgPetrology5 Workspace: none

B

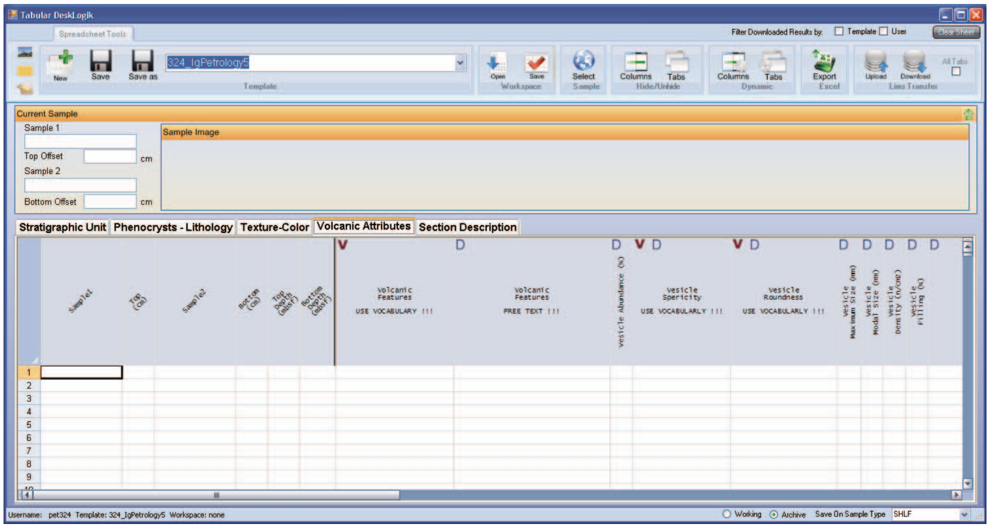

Username: pet324 Template: 324_IgPetrology5 Workspace: none

Figure F11. DESClogik data entry software template for thin section petrographic observation. Data are uploaded from DESClogik into the LIMS database and used to develop a thin section report.

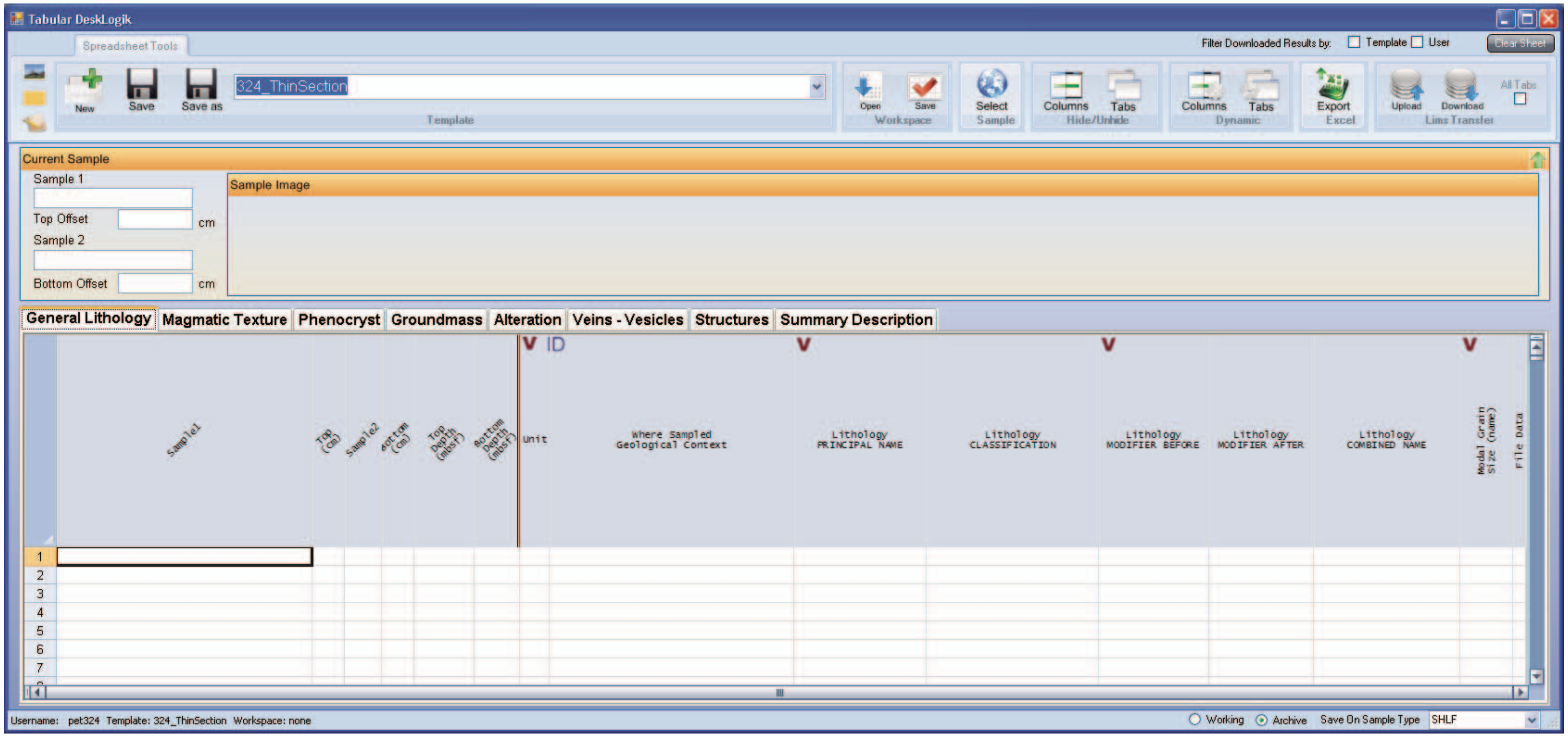

Template: 324_ThinSection

Username: pet324 Template: 324_ThinSection Workspace: none

Save On Sample Type: SHLF

Figure F12. Example of alteration log template.

Sample1	Top (cm)	Sample2	Bottom (cm)	Top depth (m)	Bottom depth (m)	Lithology/Principal name	Lithology classification	Modifier (Before principal name)	Modifier (After principal name)	Lithology name	Alteration abundance (name)	Alteration color	Alteration type	% Olivine altered	Olivine alteration mineral	% Plagioclase altered	Plagioclase alteration mineral	% Pyroxene altered	Pyroxene alteration mineral	% Groundmass altered	% of vesicle infilling	Infilling minerals of vesicles	% Glass altered	Halo around	Halo color	Halo minerals	Halo width (mm)	

Figure F13. Example of vein log template.

Sample1	Top (cm)	Sample2	Bottom (cm)	Top depth (m)	Bottom depth (m)	Vein structure	Vein orientation (qualitative)	Vein color	Vein shape	Vein geometry	Average vein width (cm)	Vein connectivity	Vein texture	Vein mineralogy - most abundant	Vein mineralogy - 2nd most abundant	Vein mineralogy - 3rd most abundant	Vein mineralogy - 4th most abundant	Vein mineralogy - 5th most abundant	Halo color	Halo minerals	Halo width (mm)

Figure F14. Vein classification used in the DESClogik vein log.

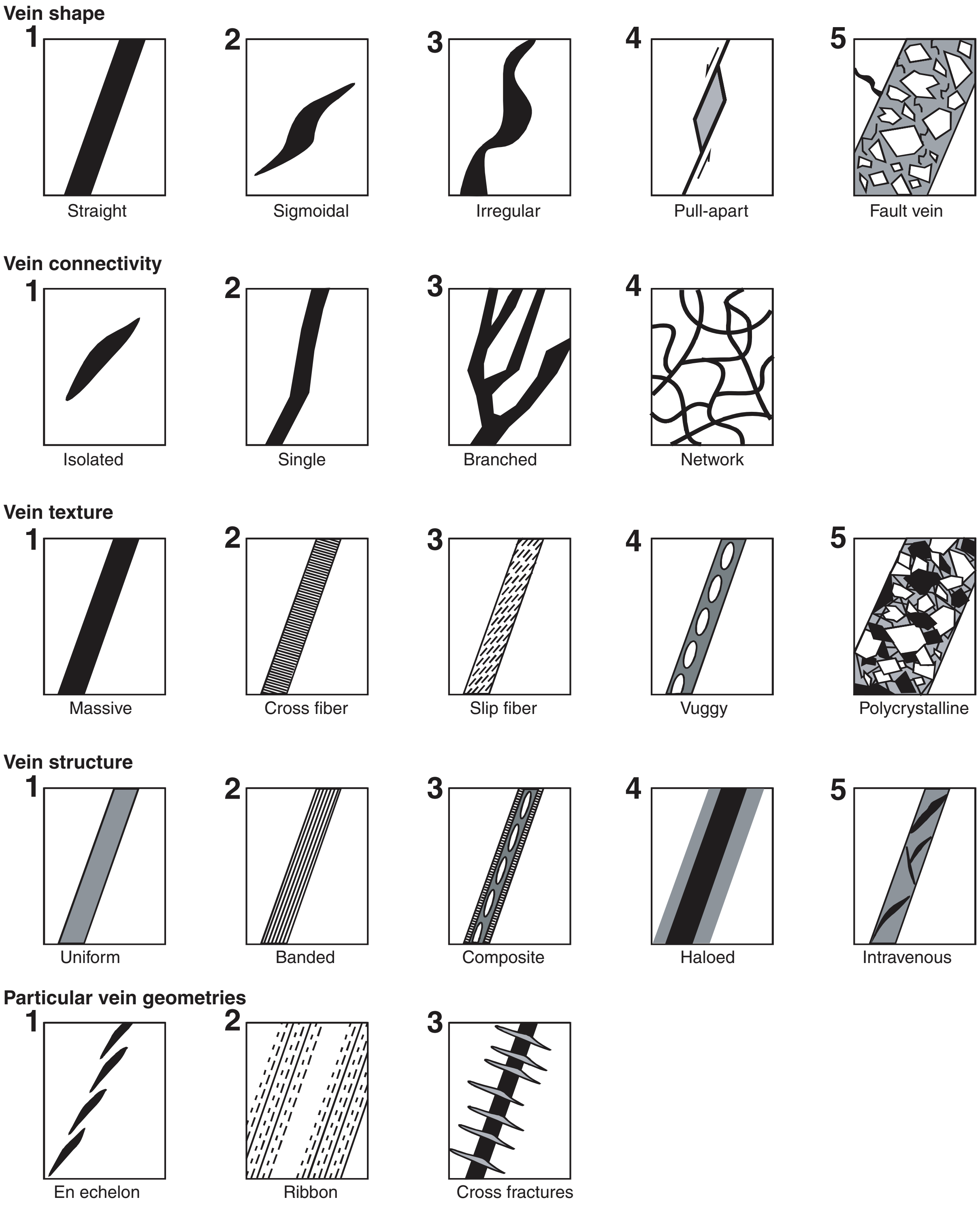

Figure F15. Example of the structural description form.

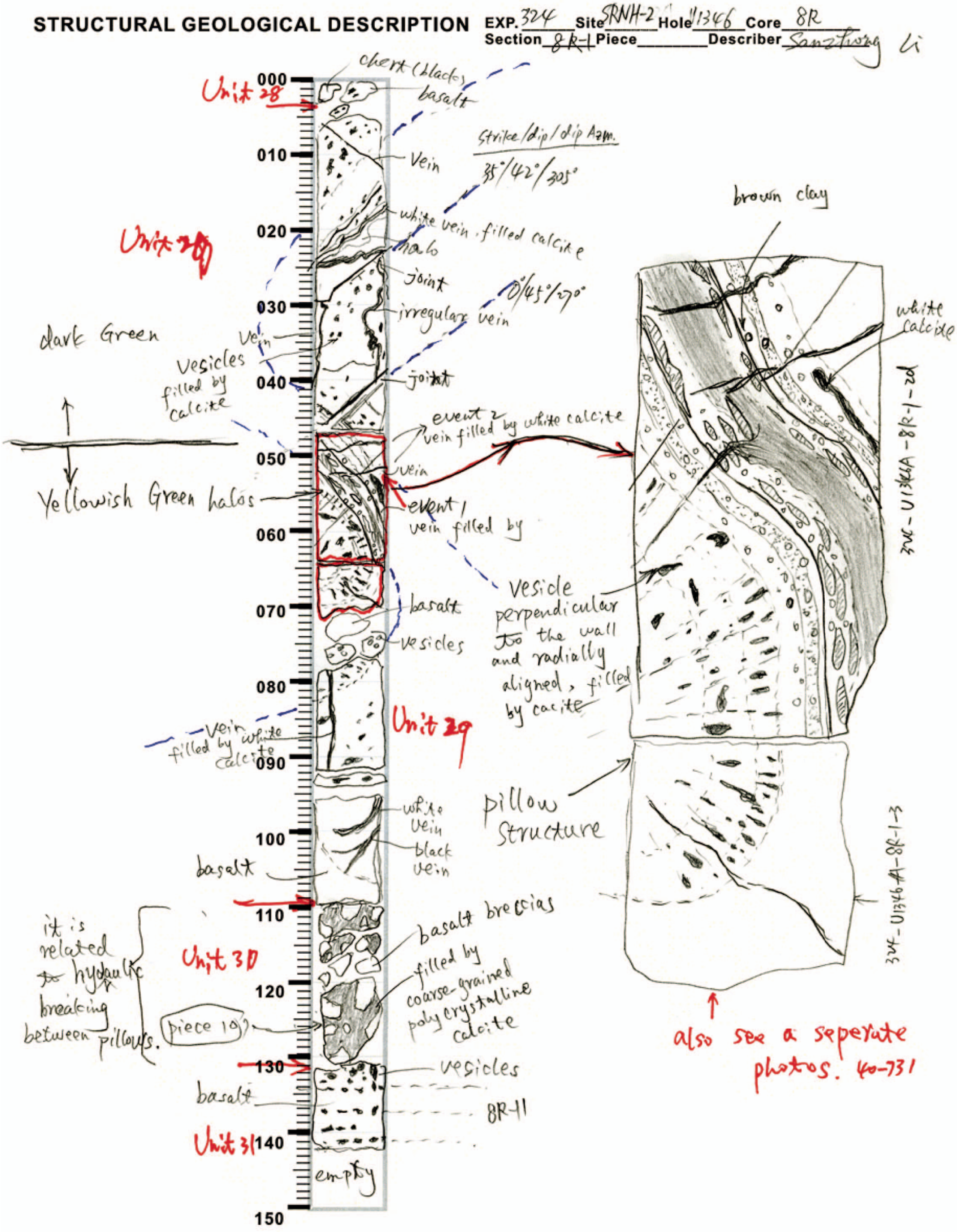

STRUCTURAL GEOLOGICAL DESCRIPTION

EXP. 324 Site SRNH-2 Hole U1346 Core 8R

Section 8R-1 Piece ____ Describer Sanzhong Li

Figure F16. Vein morphology and fiber growth examples commonly found during Expedition 324. Partially redrawn from Ramsay and Huber (1987) and ODP Leg 206 (Shipboard Scientific Party, 2003b).

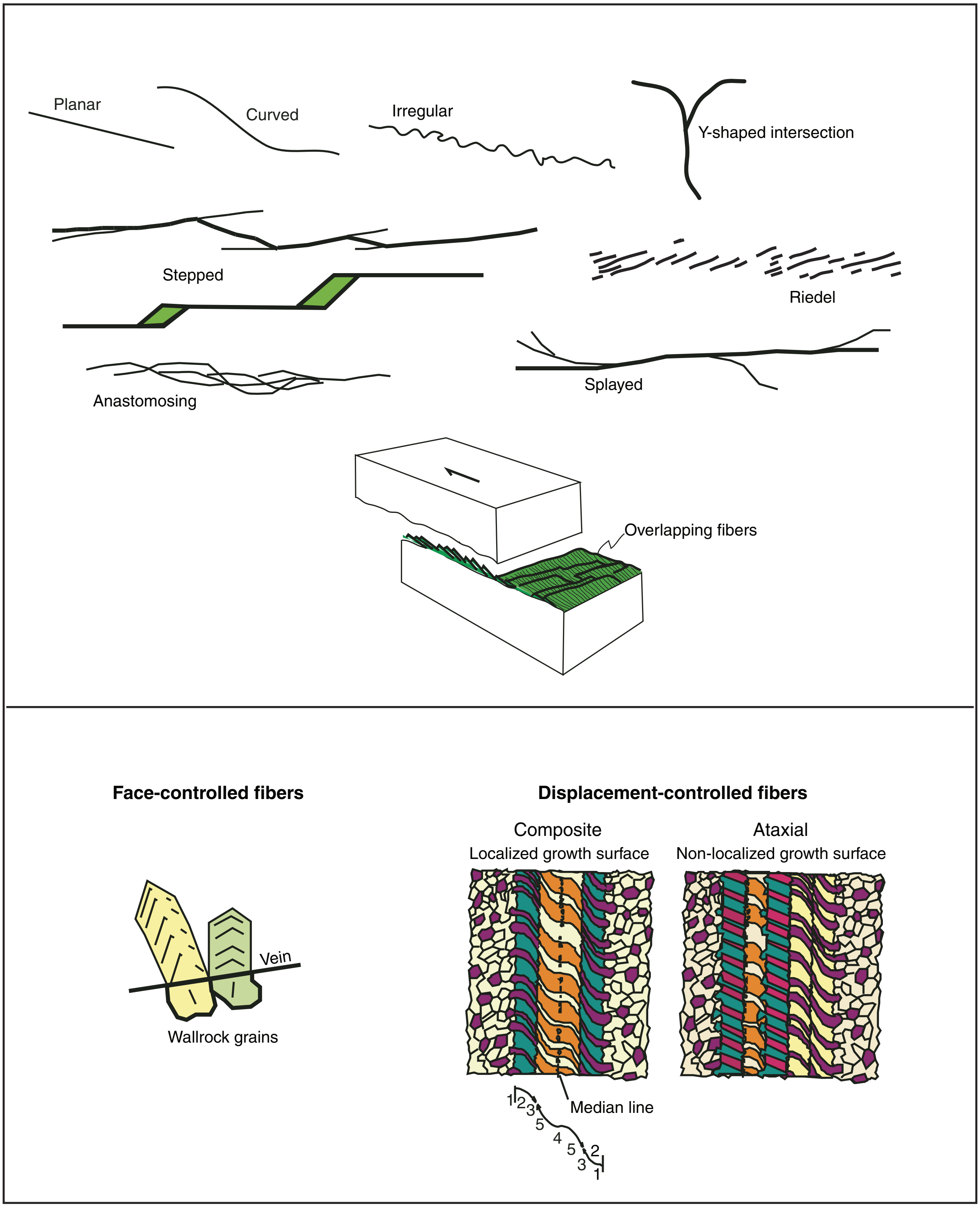

Figure F17. Conventions used for measuring azimuths and dips of structural features in core and the techniques adopted for measuring structural planes in three dimensions in the core reference frame. **A.** Working-half reference frame. **B.** Archive-half reference frame. **C.** Clinometer measurements. **D.** Measurement of true orientation of structural features. Examples of orientation measurements with the protractor-based device are shown (Leg 206, Shipboard Scientific Party, 2003b).

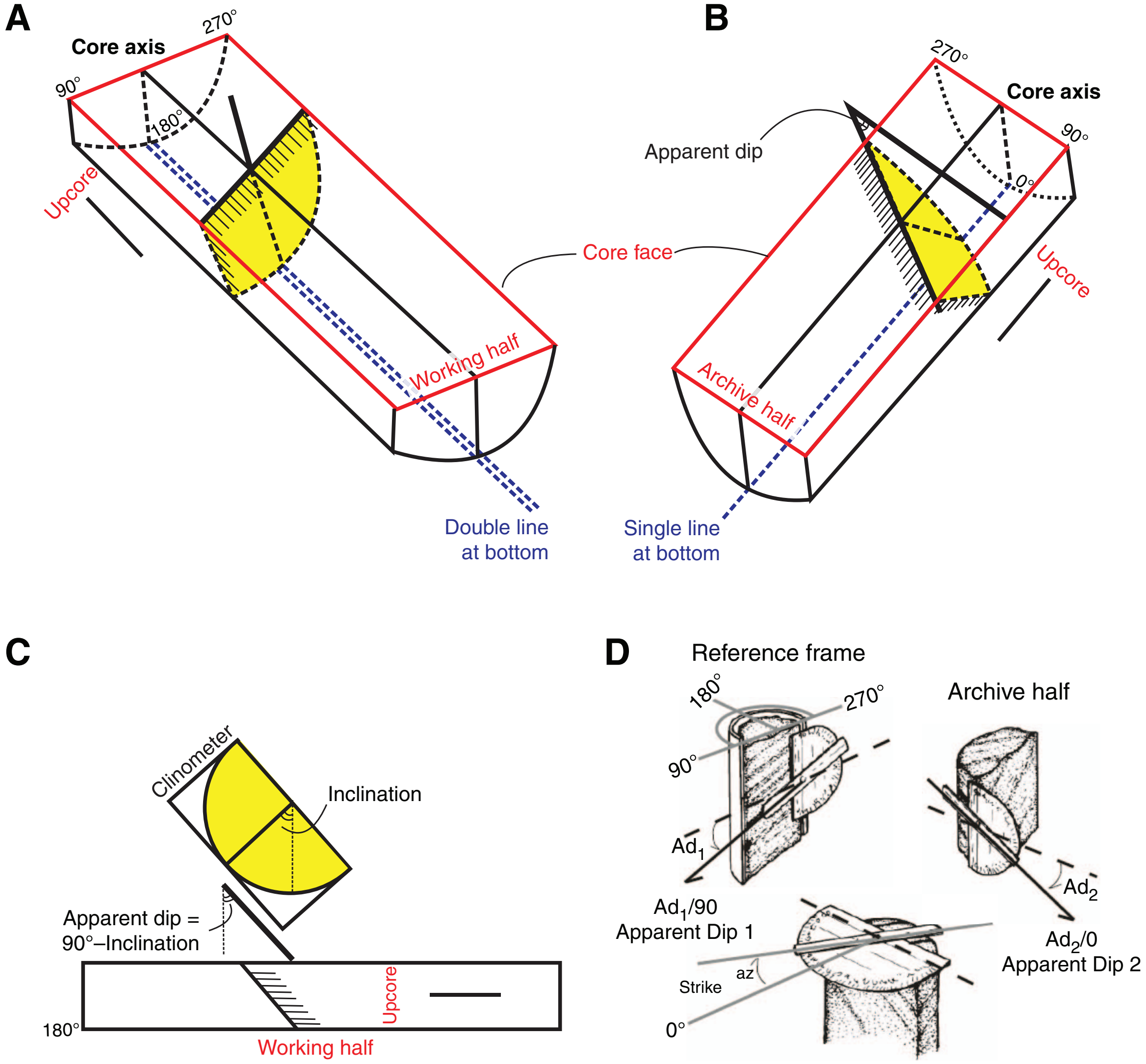

Figure F18. 2G magnetometer test results, Hole U1347A. Variation of the inclination with the demagnetizing field: green = sample demagnetized and measured by 2G magnetometer; red = sample demagnetized by 2G magnetometer, measured by Molspin Minispin magnetometer; blue = sample demagnetized by Dtech demagnetizer, measured by 2G magnetometer; pink = sample demagnetized by Dtech demagnetizer, measured by Molspin Minispin magnetometer.

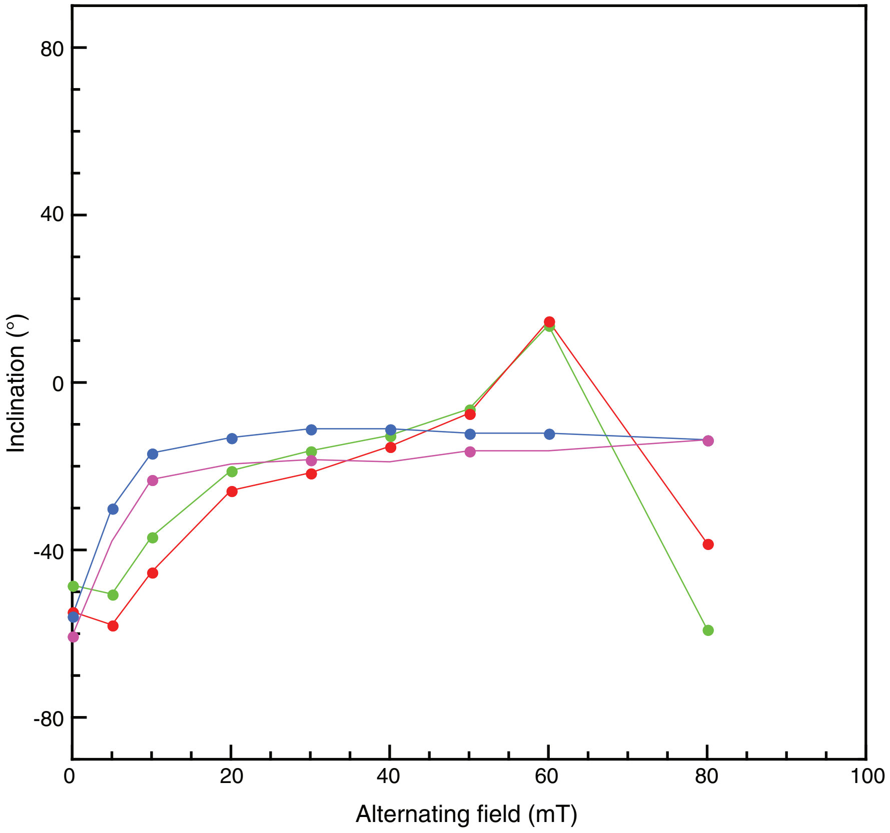

Figure F19. Wireline tool strings used during Expedition 324. HNGS = Hostile Environment Natural Gamma Ray Sonde, HLDS = Hostile Environment Litho-Density Sonde, APS = Accelerator Porosity Sonde, GPIT = General Purpose Inclinometry Tool, DITE = Dual Induction Tool model E, DSI = Dipole Sonic Imager, FMS = Formation MicroScanner, UBI = Ultrasonic Borehole Imager.

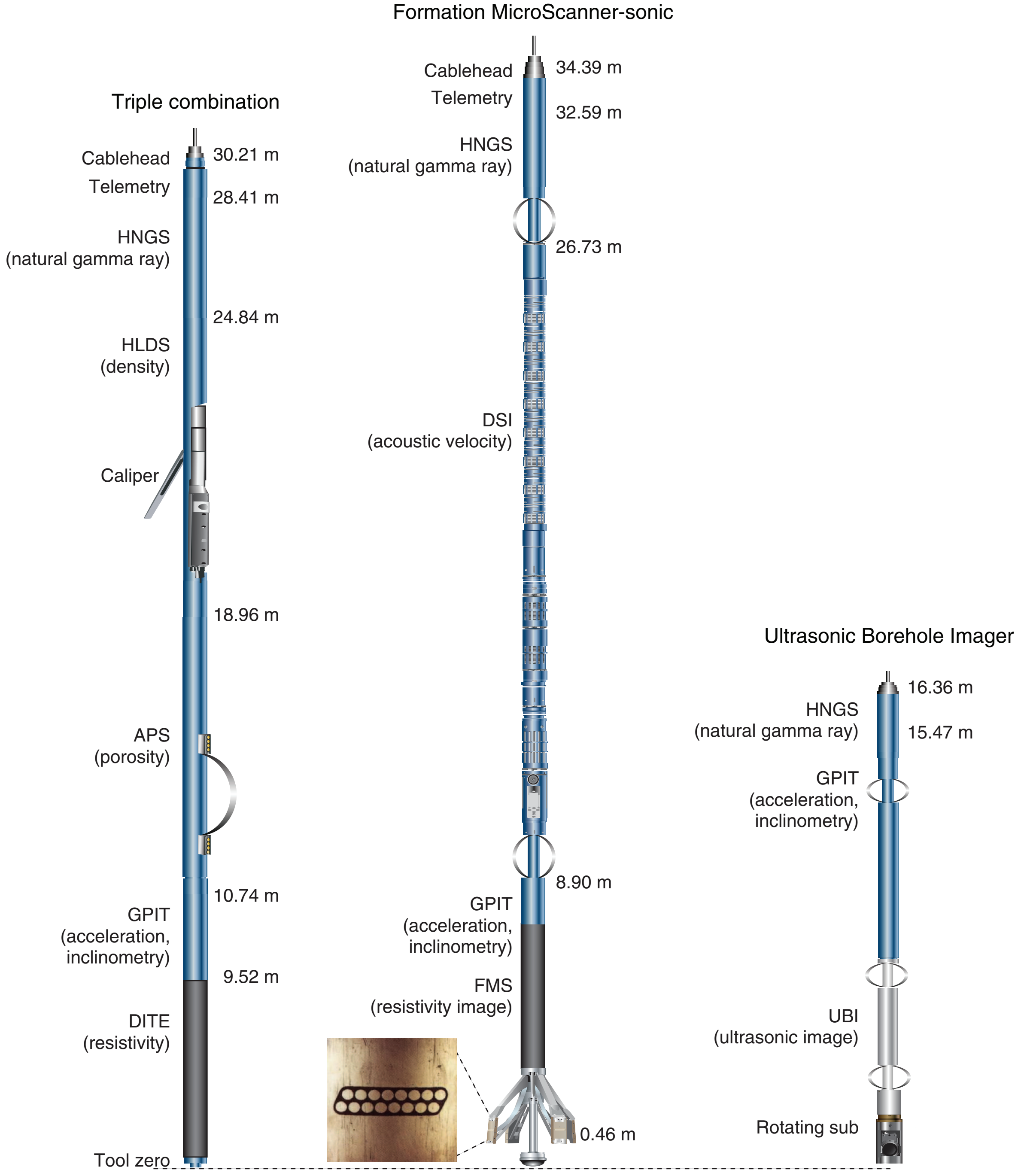

Table T1. Classification for consolidated volcaniclastic rock. (See table notes.)

Grain size (mm)	Nongenetic nomenclature	Genetic nomenclature
<1/16	Volcaniclastic mudstone	Fine hyaloclastite
1/16–2	Volcaniclastic sandstone	Hyaloclastite sandstone
2–4	Volcaniclastic conglomerate/ Volcaniclastic breccia	Granular hyaloclastite
4–64		Hyaloclastite breccia
>64		

Notes: Modified from Fisher (1961). Genetic nomenclature was used only for hyaloclastics at Site U1348.

Table T2. Calcareous nannofossil datums. (See table notes.)

Species event	Zone/Subzone (base)	Age (Ma)	References
FO *Micula prinsii*		65.4	1
FO *Nephrolithus frequens*	CC26	65.8	1, 2
FO *Micula murus*		66.2	1
FO *Lithraphidites quadratus*	UC20	67.5	1, 3
LO *Reinhardtites levis*	CC25/UC19	69.2	1, 2, 3
LO *Tranolithus orionatus*	CC24/UC18	69.6	1, 2, 3
LO *Uniplanarius trifidum*		71.3	1
LO *Aspidolithus parcus*	UC17	74.6	1, 3
LO *Eiffellithus eximius*	CC23/UC16	75.3	1, 2, 3
FO *Uniplanarius trifidum*	CC22	76	1, 2
FO *Uniplanarius sissinghii*	CC21	77	1, 2
FO *Ceratolithoides aculeus*	CC20	78.5	1, 2
FO *Misceomarginatus pleniporus*	UC15	79.5	1, 3
LO *Marthasterites furcatus*	CC19	80.6	1, 2
FO *Ceratolithoides verbeekii*		82	1
FO *Aspidolithus parcus constrictus*		82.5	1
FO *Aspidolithus parcus*	CC18/UC14	83.4	1, 2, 3
FO *Arkhangelskiella cymbiformis*	UC13	83.5	1, 3
FO *Calculites obscurus*	CC17	84	1, 2
LO *Lithastrinus septenarius*	UC12	84.7	1, 3
FO *Lucianorhabdus cayeuxii*	CC16	84.8	1, 2
FO *Reinhardtites anthophorus*	CC15/UC11	85.5	1, 2, 3
FO *Micula decussata*	CC14/UC10	87.2	1, 2, 3
FO *Lithastrinus septenarius*	UC9	88.8	1, 3
FO *Marthasterites furcatus*	CC13	89.3	1, 2
FO *Eiffellithus eximius*	CC12/UC8	91	1, 2, 3
FO *Quadrum gartneri*	CC11/UC7	93.2	1, 2, 3
LO *Helenea chiastia*	UC6	93.4	1, 3
LO *Lithraphidites acutus*	UC5	94	1, 3
FO *Cylindralithus biarcus*	UC4	94.1	1, 3
FO *Lithraphidites acutus*	CC10/UC3	96.8	1, 2, 3
FO *Gartnerago segmentatum*	UC2	97	1, 2, 3
FO *Corollithion kennedyi*	NC10b/UC1	97.6	3, 4, 5
FO *Eiffellithus turriseiffelii*	NC10a	101.7	4, 5
FO *Eiffellithus monechiae*	NC9b	105	4, 5
FO *Axopodorhabus albianus*	NC9a	106.1	4, 5
FO *Tranolithus orionatus*	NC8c	107.3	4, 5
FO *Hayesites albiensis*	NC8b	112.5	4, 5
FO *Prediscosphaera columnata*	NC8a	112.6	4, 5
FO *Rhagodiscus achlyostaurion*	NC7c	115.2	4, 5
LO *Micrantholithus hoschulzii*	NC7b	117.3	4, 5
FO *Eprolithus floralis*	NC7a	119	4, 5
LO *Conusphaera rothii*	NC6b	119.5	4, 5
FO *Hayesites irregularis*	NC6a	121.1	4, 5
FO *Flabellites oblongus*		121.1	1, 4
LO *Calcicalathina oblongata*	NC5d–NC5e	125.1	1, 4
LO *Lithraphidites bollii*	NC5c	126.3	1, 4
FO *Cruciellipsis cuvillieri*	NC5a–NC5b	128.3	1, 4
FO *Lithraphidites bollii*	NC4b	129.6	1, 4
LO *Tubodiscus verenae*	NC4a	131.2	1, 4
FO *Eiffellithus striatus*		132.2	1, 6
FO *Tubodiscus verenae*	NK3b	133.1	1, 6
LO *Rucinolithus wisei*		133.1	1, 6
FO *Eiffellithus windii*		134.2	1, 6
FO *Calcicalathina oblongata*	NK3a	135.1	1, 6
FO *Percivalia fenestrata*	NK2b	136.4	1, 6
FO *Cretarhabdus angustiforatus*	NK2a	137.7	1, 6
FO *Nannoconus steinmannii steinmannii*	NK1	140	1, 6
FO *Nannoconus steinmannii minor*	NJKd	141.5	1, 6
FO *Rotelapillus laffittei*	NJKc	142.3	1, 6
FO *Umbria granulosa*	NJKb	142.7	1, 6
FO *Helenea chiastia*	NJKa	144.6	1, 6
FO *Conusphaera mexicana mexicana*		145.6	1, 6
FO *Polycostella beckmannii*	NJ20b	146.3	1, 6

Notes: FO = first occurrence, LO = last occurence. 1 = Erba et al., 1995; 2 = Sissingh,1977; 3 = Burnett, 1999; 4 = Roth, 1973; 5 = Bralower et al., 1997; 6 = Bralower et al., 1989.

Table T3. Cretaceous planktonic foraminifer datums. (**See table notes.**)

Species event	Zone (base)	Age (Ma)	References
LO *Abathomphalus mayaroensis*		65.0	
FO *Abathomphalus mayaroensis*	*A. mayaroenesis*	68.6	1, 2
FO *Racemiguembelina fructicosa*	*R. fructicosa–C. contusa*	69.6	2
FO *Contusotruncana contusa*	*R. fructicosa–C. contusa*	69.6	2
FO *Gansserina gansseri*	*G. gansseri*	72.8	1, 3, 4
FO *Globotruncana aegyptiaca*	*G. aegyptiaca*	73.8	1, 3, 4
LO *Radotruncana calcarata*	*G. havanensis*	75.2	1, 3, 4
FO *Radotruncana calcarata*	*R. calcarata*	75.7	1, 3, 4
FO *Globotruncana ventricosa*	*G. ventricosa*	79.5	1, 3, 4
LO *Dicarinella asymetrica*	*G. elevata*	83.0	1, 3, 4
FO *Dicarinella asymetrica*	*D. asymetrica*	85.4	1, 3, 4
FO *Contusotruncana fornicata*		88.0	2
FO *Dicarinella concavata*	*D. concavata*	89.5	1, 3, 4
LO *Helvetoglobotruncana helvetica*	*M. sigali*	90.7	1, 3, 5
FO *Helvetoglobotruncana helvetica*	*H. helvetica*	93.0	1, 3, 5
LO *Rotalipora cushmani*	*W. archaeocretacea*	94.0	1, 3, 5
FO *Rotalipora cushmani*	*R. cushmani*	96.6	1, 3, 5
FO *Rotalipora reicheli*	*R. reicheli*	96.8	1, 3, 5
FO *Rotalipora globotruncanoides*	*R. globotruncanoides*	98.9	1, 3, 5
FO *Planomalina buxtorfi*		100.1	5
FO *Rotalipora appenninica*	*R. appenninica*	100.4	1, 3, 5
FO *Rotalipora ticinensis*	*R. ticinensis*	101.7	1, 3, 5
FO *Rotalipora subticinensis*		102.4	1, 3, 5
FO *Biticinella breggiensis*	*B. breggiensis*	105.0	1, 3, 5
FO *Ticinella primula*	*T. primula*	109.5	1, 3, 5
LO *Ticinella bejaouaensis*	*"H. planispira"*	112.4	1, 3, 5
LO *Planomalina cheniourensis*		112.6	1, 3, 5
FO *Ticinella bejaouaensis*	*T. bejaouaensis*	114.3	1, 3, 5
LO *Globigerinelloides algerianus*	*H. trocoidea*	115.2	1, 3, 5
FO *Globigerinelloides algerianus*	*G. algerianus*	117.1	1, 3, 5
LO *Leupoldina cabri*	*G. ferreolensis*	118.2	1, 3, 5
FO *Leupoldina cabri*	*L. cabri*	120.5	1, 3, 5
FO *Globigerinelloides blowi*	*G. blowi*	124.0	2
FO *Hedbergella similis*	*H. similis–H. kuznetsovae*	125.1	2
FO *Globigerinelloides* spp.	*H. sigali–H. delrioensis*	131.9	2
FO *Hedbergella sigali–Hedbergella aptica*	*H. sigali–H. aptica*	134.9	2

Notes: LO = last occurrence, FO = first occurrence. 1 = Sliter, 1989; 2 = Premoli Silva and Sliter, 1999; 3 = Caron, 1985; 4 = Erba et al., 1995; 5 = Leckie et al., 2002.

Table T4. Structural geology checklist for core descriptions.

Identifier/Term	Description/Explanation
Veins	
Average width	
Morphology	Planar
	Curved/Sigmoid
	Irregular
Color of filling minerals	White
	Black
	Grayish black
	Yellow
	Green
	Others
Fabric of filling minerals	Massive
	Cross-fiber
	Slip fiber
	Polycrystalline
	Vermicular
	Vuggy
	Magmatic flow
Array	En echelon/Reidel
	Parallel
	Conjugate
	Anastomosing
	Network
	Splayed/Y-shaped
	Stepped
Abundance	Vein numbers in interval
Orientation	
Crosscutting relationship	
Faults	
Offset/displacement	
Morphology	Planar
	Curved
	Irregular
Types	Dextral
	Sinistral
	Normal
	Reverse
	Microfault
Array	En echelon/Reidel
	Parallel
	Conjugate
	Anastomosing
	Network
	Splayed/Y-shaped
	Stepped
Orientation	
Crosscutting relationship	
Gouge type	Breccia
	Cataclasite
Joints	
Density	Joint numbers in interval
Morphology	Planar
	Curved
	Irregular
Types	Dextral
	Sinistral
	Tensional
	Reverse
Array	En echelon/Reidel
	Parallel
	Conjugate
	Anastomosing
	Network
	Splayed/Y-shaped
	Stepped
Orientation	
Crosscutting relationship	
Breccia/Cataclastite	
Clast shape	Angular
	Subangular
	Subrounded
	Rounded
Clast size	Min-max average size
Clast percent	Volume%
Clast type	
Matrix composition	
Matrix percent	Volume%
Origin	Fault-related
	Hydraulic
Shear zones	
Offset/displacement	
Morphology	Planar
	Curved
	Irregular
Shear sense	Dextral
	Sinistral
Mylonite type	
Clast type	δ -type
	θ-type
	ϕ-type
Clast mineral	
Clast percent	Volume%
Lineation type	
Lineation mineral	
Matrix composition	
Matrix percent	Volume%
Width of shear zone	
Orientation of mylonitic foliation	
Crosscutting relationship	

Table T5. Wavelengths used for rock measurements by ICP-AES, Expedition 324. (**See table notes.**)

Element	Wavelength (nm)	
Major:		
Si	250.690	251.611
Ti	337.280	
Al	308.215	396.152
Fe	239.563	
Mn	257.610	
Mg	280.271	285.213
Ca	317.933	
Na	588.995	589.592
K	769.897	
P	214.914	
Trace:		
Ba	493.409	
Sr	407.771	421.552
Zr	339.198	343.823
Y	360.073	
V	292.401	
Sc	361.383	
Cu	324.754	
Zn	213.856	
Co	228.615	
Cr	283.563	
Ni	231.604	

Notes: For elements listed with two wavelengths, concentrations derived from both measurements were averaged if calibration lines for each wavelength were of similar quality. Otherwise, the wavelength yielding the best calibration line was used.

Table T6. Typical sequence of analyses in ICP-AES run. (See table notes.)

Analysis number	Identifier/Type
1	DRIFT 1 (BHVO-2)
2	BLANK - 1
3	BHVO-2 STD
4	BIR-1 STD
5	BCR-2 STD
6	DRIFT 2 (BHVO-2)
7	JGB-1 STD
8	JA-3 STD
9	SCO-1 STD
10	JR-2 STD
11	DRIFT 3 (BHVO-2)
12	STM-1 STD
13	NBS-1C STD
14	BAS-140 Check
15	BAS-206 Check
16	DRIFT 4 (BHVO-2)
17	Sample
18	Sample
19	Sample
20	Sample
21	DRIFT 5 (BHVO-2)
22	Sample
23	Sample
24	Sample
25	Sample
26	DRIFT 6 (BHVO-2)
27	Sample
28	Sample
29	Sample
30	Sample
31	DRIFT 7 (BHVO-2)
32	BLANK - 2
33	BAS-140 Check
34	BAS-206 Check
35	Sample
36	DRIFT 8 (BHVO-2)
37	Sample
38	Sample
39	Sample
40	Sample
41	DRIFT 9 (BHVO-2)
42	BAS-140 Check
43	BAS-206 Check
44	BLANK - 3
45	DRIFT 10 (BHVO-2)

Notes: STD = calibration standard. Check = check standard. DRIFT = standard used for drift correction.

Table T7. Check-standard data for ICP-AES analysis, Expedition 324. (**See table notes.**)

	BAS-140			BAS-206		
Element	Mean (N = 16)	2σ	Published[*]	Mean (N = 16)	2σ	Published[†]
Major (wt%):						
SiO_2	50.46	1.73	50.50	48.85	1.99	49.53
TiO_2	1.04	0.04	0.98	2.05	0.05	2.04
Al_2O_3	14.62	0.52	14.60	14.08	0.49	14.22
$Fe_2O_3^T$	10.94	0.87	11.10	14.32	0.42	14.30
MnO	0.18	0.01	0.19	0.25	0.01	0.22
MgO	8.04	0.25	8.15	6.73	0.24	6.77
CaO	12.91	0.73	12.40	9.78	0.54	9.70
Na_2O	1.86	0.09	1.84	2.87	0.11	2.78
K_2O	BD	0.22	0.01	0.10	0.18	0.18
P_2O_5	0.07	0.07	0.08	0.18	0.03	0.16
Trace (ppm):						
Ba	12	18.4	2[‡]	51	11.3	49.9
Sr	39	6.5	44	109	28.5	112
Zr	47	11.2	49[‡]	118	8.1	127
Y	28	2.3	24	50	16.7	43.8
V	332	18.7	333[‡]	452	17.5	461
Sc	45	1.7	43	49	2.4	47
Cu	79	15.7	81	52	14.3	60[‡]
Zn	80	7.1	80	126	11.2	103[‡]
Co	46	2.4	55	54	2.3	48[‡]
Cr	191	9.7	186	135	10.1	83.7
Ni	86	9.0	85	51	22.9	53.5

Notes: * = values published by Sparks and Zuleger (1995). † = values published by Leg 206 Shipboard Scientific Party (2003). ‡ = values reported by Expedition 309/312 Shipboard Scientific Party (2006). BAS-140 and BAS-206 are laboratory standards. Mean values of 16 analyses are indicated. Uncertainties are listed as ±2σ. $Fe_2O_3^T$ = total iron calculated as ferric oxide. BD = below detection.

Table T8. MACOR ceramic standards for thermal conductivity.

Site	Standard	2σ	Number of measurements
U1346	1.615	0.017	8
U1347	1.617	0.012	8
U1348	No measurements		
U1349	1.609	0.019	6

Table T9. Moisture and density variables, units, and calculations.

Quantity and variable	Unit	Value or calculation
Density salt, ρ_{salt}	g/cm^3	2.22
Density pore water, ρ_{PW}	g/cm^3	1.024
Mass ratio (salinity correction)	None	0.965
Wet mass, M_W	g	Measured
Dry mass, M_D	g	Measured
Dry volume, V_D	cm^3	Measured
Mass pore water, M_{PW}	g	$(M_W - M_D)$/mass ratio
Volume pore water, V_{PW}	cm^3	M_{PW}/ρ_{PW}
Mass salts, M_{salt}	g	$M_{PW} - M_W + M_D$
Volume salts, V_{salt}	cm^3	M_{salt}/ρ_{salt}
Wet volume, V_W	cm^3	$V_D - V_{salt} + V_{PW}$
Mass of solids, M_{solids}	g	$M_W - M_{PW}$
Volume solids, V_{solids}	cm^3	$V_W - V_{PW}$
Porosity, ϕ	None	V_{PW}/V_W
Wet density, ρ_W	g/cm^3	M_W/V_W
Dry density, ρ_D	g/cm^3	M_{solids}/V_W
Grain density, ρ_{grain}	g/cm^3	M_{solids}/V_{solids}
Void ratio	None	V_{PW}/V_{solids}

Table T10. Filter parameters. (See table note.)

Data	Minimum detectable gap (cm)	Minimum piece length (cm)	Edge effect (cm)
GRA density	0.2	2	1
Magnetic susceptibility	0.2	8	4
Magnetic susceptibility point	0.2	3	1.5
L*	0.2	3	1.5
b*	0.2	3	1.5

Note: GRA = gamma ray attenuation, L* = reflectance parameter, b* = red/green color parameter.

Table T11. Wireline tool string downhole measurements, Expedition 324. (See table notes.)

Tool string	Tool	Measurement	Sampling interval (cm)	Approximate vertical resolution (cm)
Triple combination	HNGS	Spectral gamma ray	15	51
	GPIT	Tool orientation	0.25 and 15	NA
	APS	Porosity	5 and 15	43
	HLDS	Bulk density	2.5 and 15	38/46
	DITE	Resistivity	15	200/150/76
Formation MicroScanner-sonic	HNGS	Spectral gamma ray	15	51
	GPIT	Tool orientation	0.25 and 15	NA
	FMS	Microresistivity imaging	0.25	0.5
	DSI	Acoustic velocity	15	107
Ultrasonic Borehole Imager	UBI	Acoustic imaging	0.15	0.51
	GPIT	Tool orientation	0.25 and 15	NA
	HNGS	Spectral gamma ray	15	51

Notes: All tool and tool string names are trademarks of Schlumberger. Sampling interval based on optimal logging speed. Acoustic imaging approximate vertical resolution is at 500 kHz. NA = not applicable. For definitions of tool acronyms, see Table T12.

Table T12. Acronyms and units used for downhole wireline tools and measurements. (See table notes.)

Tool	Output	Explanation	Unit
APS		Accelerator Porosity Sonde	
	APLC	Near array porosity (limestone calibrated)	%
	SIGF	Formation capture cross-section (Σ_f)	Capture units
	STOF	Tool standoff (computed distance from borehole wall)	Inch
DITE		Dual Induction Tool model E	
	IDPH	Deep induction resistivity	Ωm
	IMPH	Medium induction resistivity	Ωm
	SFLU	Spherically focused resistivity	Ωm
DSI		Dipole Sonic Imager	
	DTCO	Compressional wave delay time (Δt)	µs/ft
	DTSM	Shear wave delay time (Δt)	µs/ft
	DTST	Stoneley wave delay time (Δt)	µs/ft
FMS		Formation MicroScanner	
	C1, C2	Orthogonal hole diameters	Inch
	P1AZ	Pad 1 azimuth	°
		Spatially oriented resistivity images of borehole wall	
GPIT		General Purpose Inclinometry Tool	
	DEVI	Hole deviation	°
	HAZI	Hole azimuth	°
	F_x, F_y, F_z	Earth's magnetic field (three orthogonal components)	Oe
	A_x, A_y, A_z	Acceleration (three orthogonal components)	m/s^2
HLDS		Hostile Environment Litho-Density Sonde	
	RHOM	Bulk density	g/cm^3
	PEFL	Photoelectric effect	b/e^-
	LCAL	Caliper (measure of borehole diameter)	Inch
	DRH	Bulk density correction	g/cm^3
HNGS		Hostile Environment Natural Gamma Ray Sonde	
	HSGR	Standard (total) gamma ray	gAPI
	HCGR	Computed gamma ray (HSGR minus uranium contribution)	gAPI
	HFK	Potassium	wt%
	HTHO	Thorium	ppm
	HURA	Uranium	ppm
UBI		Ultrasonic Borehole Imager	
	TTAV	Transit time average	µs
	AWAV	Amplitude average	db
	BRAC	Radii average	Inch
		Spatially oriented acoustic images of borehole wall	

Notes: For the complete list of acronyms used in IODP and for additional information about tool physics, consult IODP-USIO Science Services, LDEO, at **iodp.ldeo.columbia.edu/TOOLS_LABS/tools.html.**